A Molecular Simulation Study of Amorphous Solid Water under Extraterrestrial Conditions

By

John James McCann

In the fulfilment of the requirement

for the degree of Doctor of Philosophy

Department of Chemical and Process Engineering

University of Strathclyde

Supervised by

Dr Martin B Sweatman

Copyright

Declaration

I declare that this thesis embodies my own research work and that it was composed by myself. Where appropriate, I have made acknowledgements to the work of others.

John James McCann

Acknowledgements

First of all, I would like to express my sincere gratitude towards my supervisor Dr Martin Sweatman, for his guidance, encouragement and continuous support in the whole period of my PhD study. Dr Sweatman was always there to listen and give me advice. He showed me different ways and perspectives to deal with a research problem, which benefited me a lot.

I would like to thank my mother and father for everything they have done for me over the years and for their continued support during my studies.

Abstract

This thesis studies Amorphous Solid Water (ASW) using Molecular Dynamics for the purpose of investigating what governs asteroid, planet and comet formation, which in turn provides the foundations for life to exist in the universe.

This thesis begins by presenting the astronomical background to this study, focusing on our current understanding of how the universe evolved from the Big Bang to its current state, and the role which interstellar dust grains have played in stellar evolution. It is currently believed that the icy mantles which reside on interstellar dust grains in cold dense regions of the interstellar medium (ISM) act as a catalyst allowing the formation of prebiotic molecules. The catalytic properties of icy mantles responsible for synthesis of these molecules depend on the concentration of unsatisfied, or 'dangling', ASW hydrogen bonds within these icy mantles, Observational studies do not detect dangling O-H bonds but experimental studies do. This study suggests that while ASW dangling O-H bonds do exist in these icy mantles, most water molecules exist in a hydrogen bonded network with about 3.78 hydrogen bonds per water molecule. This should be compared with crystalline ice for which all four hydrogen bonds per molecule. Moreover, this work also indicates that there are more dangling bonds in the interfacial region than the bulk region.

Work in this thesis also investigates the role that ‘shadowing’ and ‘electrostatic steering’ play in ASW growth on extraterrestrial dust surfaces. Currently, it is believed that the coral-like structure of ASW is caused solely by shadowing, a geometric phenomenon. However, this work finds that although shadowing has an influence, ASW growth and its subsequent structure are primarily determined by electrostatic steering, i.e. a process where depositing water molecules are steered towards dangling O-H bonds on the ASW surface.

This thesis concludes by contrasting these new findings with the current literature on the properties and structure of ASW, and describing the implications for our

understanding of stellar evolution.

Table of Contents

Table of Tables

List of Figures

1. Introduction

The universe, which contains all the physical laws we know, appears to us as an infinite array of space and time. This incomprehensible vastness has inspired and intrigued man for millennia ranging from ancient philosophers to modern day scientists. Although, as time progresses our knowledge of this universe is refined through scientific rigour, the original questions proposed by philosophers are just as significant and widely perplexing now as they were back then. Why does life exist? How was life created in the universe? Whilst the former question will always remain a purely philosophical one; the latter is at the forefront of modern science.

It is widely accepted within the scientific community that the universe initially existed as a concentration of mass and energy which underwent rapid expansion, in a process known as the Big Bang. 300,000 years after the big bang our universe existed as a giant cloud of hydrogen and helium gas which astronomers currently believe was locally subject to gravitational collapse, resulting in the formation of huge “Megasuns”. These megasuns were composed entirely of hydrogen and would have been hundreds of times the mass our sun. Generally, stars which are several solar mass tend to be short lived as they use up vast amounts of matter through nuclear fusion reactions. Essentially, these megasuns converted hydrogen into heavier elements by nuclear fusion reactions releasing vast amount of energy in the process. So much so, that stars (both mega suns and present stars) can be thought of as giant nuclear processing factories in space.

ELEMENT	ABUNDANCE WITH RESPECT TO HYDROGEN
He	1.0x10-1
C	2.1x10-4
O	4.6x10-4
N	6.6x10-5
S	2.7x10-5
Mg	2.5x10-5
Si	1.2x10-5

Table 1: The comparative abundance of heavier atoms in the ISM [1,2]

Although approximately 99% of the current universe mass is composed of hydrogen and helium (of which 90% and 10% is hydrogen and helium respectively), stellar nuclear fusion has produced heavier elements such as carbon, oxygen, nitrogen, and silicon to name but a few, which now account for about 1% of the mass of the universe. The vast proportion of heavier elements are contained within dust grains, which are generally either siliceous or graphitic, believed to be heterogeneous in nature, and known to play a pivotal role in the evolution of the universe through important processes such as scattering, reddening, radiation, extinction and star/planet formation[3-6].

This thesis focuses on the latter role of dust grains – star and planet formation. We already know that stars form in dense cores of molecular clouds in the interstellar medium (ISM)[7,8], which is populated by icy dust grains[8].

Icy dust grains also play a pivotal role in planet, asteroid, and comet formation in the universe. In addition to this, the icy mantle on these icy dust grains are thought to act as a catalyst producing more complex molecules such as methane, ammonia, carbon dioxide, and methanol, along with over 200 different molecular species, which increases the chemical richness of the universe[3,8].

The increased chemical abundance of more complex molecules is instrumental in “kick starting” the gravitational collapse of dense cores resulting in star formation in the universe[9]. Furthermore, icy mantles have the potential to create prebiotic and organic

molecules such as formic acid, formamide, acetaldehyde and amino acids[10-13], and influence the formation of life itself in the universe!

However, our knowledge of icy dust grain morphology, porosity and chemical composition is poorly understood. In particular, as mentioned above, we know that dust grains have mainly graphite or silica cores, and are heterogeneous in composition[3,4,14,15]. Recent observational studies such as ISO SWS and Spitzer have found that the dominant ice in icy dust grains is water ice[16,17]. A series of laboratory based studies, especially work by Van Dishoeck and Blake[5], strongly indicates that dust grain icy mantles are porous. This is further reinforced by recent work by Accolla et al.[18] in which ASW is grown under interstellar conditions in the laboratory. Their samples exhibit two infrared absorption peaks at 3720 and 3696 cm^{-1}, indicative of dangling O-H bonds. Furthermore, Ehrenfreund and Fraser et al.[3] also grew ASW under experimental conditions and found ASW to be highly porous. However, in spite of these experimental studies these infrared absorption peaks are not detected in astronomical observations[19,20].

These icy mantles are produced by two types of vapour deposition. Firstly, when atoms freeze out onto dust grain surfaces, in molecular clouds, molecular hydrogen is produced, which then reacts with atomic oxygen through surface chemistry producing water. In this thesis formation of water on dust grain surfaces by this route is referred to as Chemical Vapour Deposition (CVD). Secondly, during the protostellar phase of star formation bipolar jets (see section 1.2.7) produce water from the abundance of molecular hydrogen and atomic oxygen in the gas phase. In addition to this, water desorbs from icy dust grain mantles close to a protostellar object due to high stellar temperatures. This water then physisorbs (re-accretes) onto cooler dust grains located further away from the protostellar object in the cooler equatorial midplane region of the protostellar disk. This is called Physical Vapour Deposition (PVD) in this thesis. These icy dust grains formed by PVD in the equatorial midplane are thought to collide and aggregate over millions of years[3] producing not only planets, asteroids and comets but also the conditions for life to exist in the universe.

Therefore, these icy mantles are highly important, displaying physical phenomena instrumental in shaping the universe as it exists today. If these icy mantles are predominantly water and porous what are their physical properties and morphology? Which ice structure is likely to be present on dust grains at extremely low pressures and temperatures? These are the questions that this work sets out to investigate. In order to make progress we must first look at different water ice morphologies in the water phase diagram.

1.1 Amorphous Solid Water

Oxygen is one of the most electronegative atoms in the periodic table. This means that the electrons of other atoms in the same molecule are drawn towards it, resulting in an excess of charge near the oxygen atom. In water molecules this produces a charge variation which gives water its characteristic hydrogen bonding and proton disorder, and subsequent behaviour resulting in an extensive range of crystalline solid phases as shown in Figure 1 below. In addition to this, water's molecular geometry results in a strong electrostatic dipole, rendering water sensitive to external electric fields and the proximity of other charges and dipolar molecules. Moreover, water's molecular centre of mass is situated close to the oxygen atom, resulting in a low moment of inertia. The combination of these factors means that water molecules experience high angular accelerations even at low temperatures. All water ices are dominated by a hydrogen bonding network, as each water molecule can accept and donate two hydrogen bonds each. This four-fold proton disordered hydrogen bonding network is organised in a tetrahedral bonding network. Although most of the water ices are in the high pressure region of the phase diagram it is the low pressure and temperature range (extraterrestrial conditions) which this study is interested in for the purposes understanding which ice structure is present on space borne icy dust grains.

There are 9 recognised ice structures in the low pressure and temperature range of the phase diagram namely[3,7]:

- Hexagonal Ice
- Cubic Ice

- High density amorphous ice (HDA)
- Very high density amorphous ice (VHDA)
- Low density amorphous ice (LDA)
- Hyperquenched solid water (HSW)
- Nanoporous Amorphous solid water (Nanoporous ASW)
- Microporous Amorphous solid water (Microporous ASW)
- Amorphous solid water to cubic ice transition phase

Hexagonal ice is the only thermodynamically stable phase for all low pressures and temperatures whilst the rest are only mechanically stable or metastable over narrow temperature and pressure ranges[3]. Hexagonal ice can be found in ice bergs and house hold freezers as ice cubes; LDA and HDA can be found in glaciers with HDA forming in the high pressure regions[3]; HSW can be found in the upper atmospheres of our planet, hail stones and in the interstellar regions of space[3]. Amorphous solid water is only found in the interstellar medium (ISM) naturally. Figure 1.1 below shows the mechanical pathways for formation of these ices over a range of temperatures and pressures.

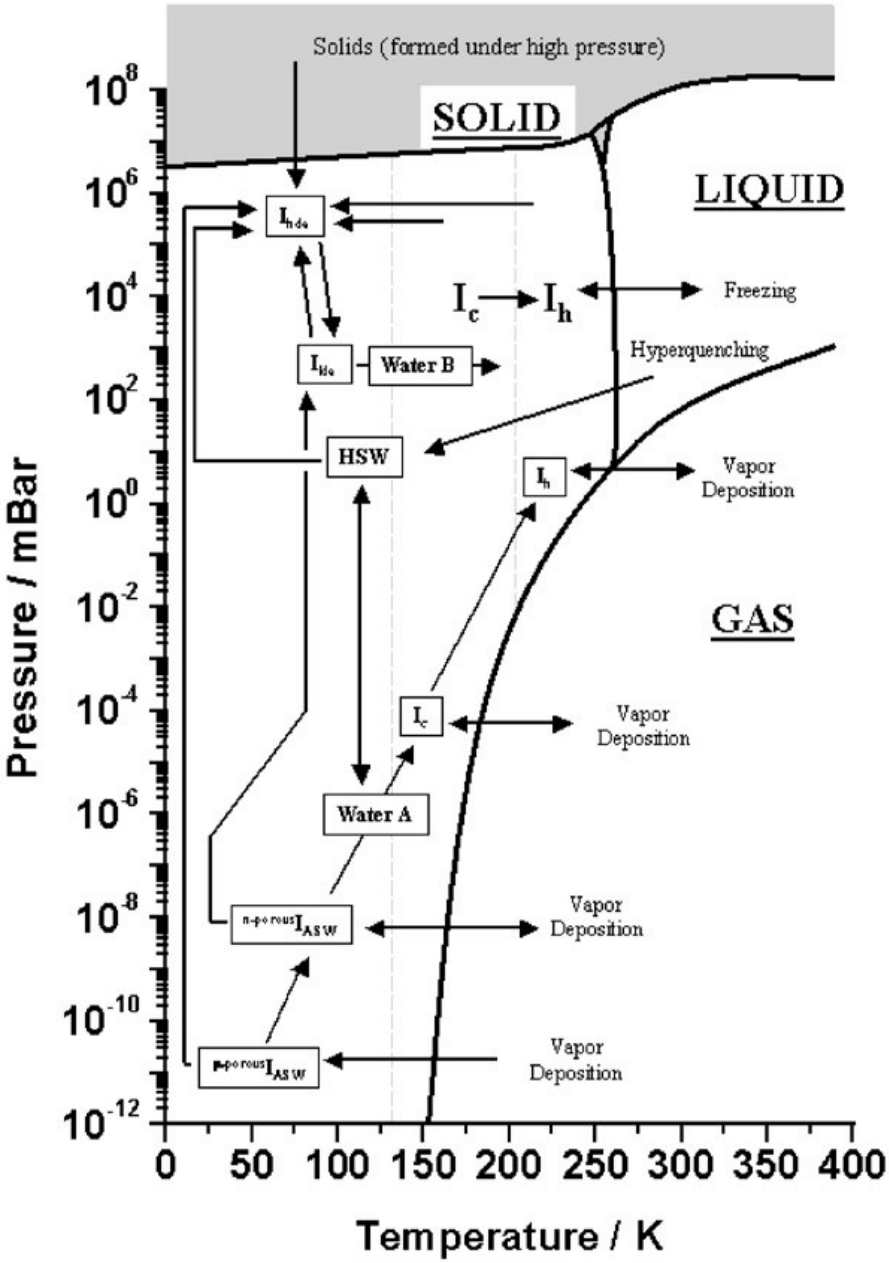

Figure 1: This figure illustrates the low pressure and temperature range of the water phase diagram, compiled from Earth based experimental studies. The arrows show metastable/thermodynamic pathways with single and double arrows representing irreversible and reversible reaction respectively. Ih and Ic are hexagonal and cubic ice respectively; LDA, HDA and water B are low, high and very high density amorphous ices. Ic micro and nanoporous ASW are formed through vapour deposition, where microporous ASW forms at the lowest PT and undergoes a structural change during pore collapse to form nanoporous ASW when subjected to higher PT.[3]

Hexagonal ice is formed when water is frozen at atmospheric pressure. HDA can be formed by compressing hexagonal ice, cubic ice, LDA, VHDA (which is water B in figure 1.1) or microporous ASW, and has a typical density of around 1.1 g cm^{-3} [3]. LDA forms when HDA is heated at atmospheric pressure at around 77K and has a typical density of 0.94 g cm^{-3}. At extremely low pressures and temperatures (less than 70-80K) mircoporous ASW forms through PVD vapour deposition onto cold substrates, producing a highly porous (4000 m^2 g^{-1}) amorphous ice. Microporous ASW when heated to around 65K undergoes pore collapse producing nanoporous ASW[3]. When nanoporous ASW is heated to between 120-140K there is a viscous liquid transition phase[21] (shown as water A in figure 1.1) that is experienced before increased crystallisation leads to cubic ice formation, which in turn is irreversibly converted into hexagonal ice at around 200K.

Given ISM temperatures and pressures, microporous ASW appears to be the most likely icy mantle morphology formed on dust grain substrates[7,8,22] in the ISM. Although microporous ASW is believed to be highly porous and amorphous the precise structural properties of ASW are relatively unknown.

Recent work by Salter and Fraser et al.[9] investigated the sticking probability of colliding icy silica dust grains at 0.1-0.28 m/s, and found that there was a 10% sticking probability for all dust grain collisions. The icy mantles used in this experiment were not highly porous ASW but much more compact hexagonal ice maintained at a temperature of 130K. This study concludes that lower ambient temperatures will increase the sticking probability as thermal energy from collisions (kinetic impact energy) will be dissipated quicker upon impact. Furthermore, replacing a compact hexagonal icy mantle with a highly porous ASW icy mantle should act as a 'cushion' for colliding icy dust grains, allowing firstly, a more gradual release of impact energy which will minimise sublimation and secondly, converting this collision energy into molecular re-structuring of the ASW structure by breaking existing hydrogen bonds or annealing the ASW structure. Consequently, highly porous ASW icy mantles should increase icy dust grain aggregation in the ISM, relative to compact ice mantles, which is

essential for planet formation before gravity becomes a more dominant aggregation driver.

Therefore, this thesis investigates ASW structural properties under extraterrestrial conditions which is key to understanding how planet, comets, asteroids, stars and life form in the universe.

1.2 Water in the ISM

Dust grains, which predominantly have graphite or silica cores[6], measuring only a few hundred nanometres across, make up the vast majority of solids in the ISM (1% of ISM mass is dust[22]). It is currently believed that these dust grains form in the atmospheres of cool stars and then dissipate into the ISM where they may be subject to further chemical restructuring from background UV radiation[16]. The ISM is composed of several different types of region or phase. The ISM plasma phase, which consists almost entirely of ionized hydrogen, dominates the ISM and is known as the tenuous region of the ISM. The neutral atomic phase on the other hand (composed almost entirely of atomic hydrogen), is found in diffuse clouds. The rich gas and surface chemistry as well as the role dust grains play in diffuse clouds are detailed in the next three sections. Table 2 below illustrates ISM pressures and temperatures.

	ISM tenuous clouds in ionized region	ISM diffuse clouds in neutral region	ISM molecular clouds
Density	100 atoms/cm^3	100 atoms/cm^3	10000 atoms/cm^3
Gas Temperature	100's - 1000's K	100-600K	30K
Dust Temperature	100-1000K	100K	10K

Table 2: Table illustrating the density and temperature of different ISM regions[22]

1.2.1 Diffuse Clouds

Diffuse clouds are rare ISM regions saturated with UV starlight. These clouds are 90% hydrogen and 9% helium by volume[22], and occur i) in regions close to nearby stars where the powerful photodissociative nature of UV and X-rays is dominant, or ii) in regions closer to dense clouds where neutral atoms exist and star formation occurs. As the dust grain and gas phase density in diffuse clouds is several orders of magnitude

lower than in molecular clouds[23,24], cosmic and UV rays emitted from surrounding stars can easily penetrate this phase, ionising atomic hydrogen. It is estimated that 0.01% of all hydrogen in diffuse clouds is ionised by nearby stars, allowing limited gas phase chemistry producing the following molecules: CO, CH, CN, CH^+, CN^+[3,16,25]. These molecules exist in diffuse clouds as there is little to no activation energy barrier for their formation, and associative recombination of an ionised hydrogen atom with an electronegative atom such as oxygen or nitrogen occurs readily due to a strong binding energy. Gas and dust temperatures can range from 100's-1000's K and 100-1000K respectively, close to nearby stars (in the ionized diffuse region). However, in diffuse neutral regions (further away from nearby stars) gas and dust temperatures are approximately 100-600K and 100K respectively. Dust grains in the diffuse ISM, typically 100's of nanometres across, absorb destructive UV and X-rays and re-emit in infrared regions thereby shielding other regions of the ISM. However, this shielding is extremely limited when compared to the level of shielding that occurs in molecular clouds where gas and dust densities are much higher.

1.2.2 Molecular Clouds

Molecular clouds are sometimes referred to as Dark clouds as the degree of scattering in the visible spectrum is such that no background radiation appears to penetrate this region of the ISM, as shown in figure 1 below. The presence of CO and molecular hydrogen in molecular clouds, which have many more energy modes (i.e. a much greater density of states) to excite than simple atoms, greatly increases interstellar extinction due to dissipation of energy via molecular vibrational and rotation modes. As a result inner regions of molecular clouds are shielded from UV rays. However, cosmic rays are still prevalent. The presence of CO in the ISM is seen as the boundary between diffuse and molecular clouds.

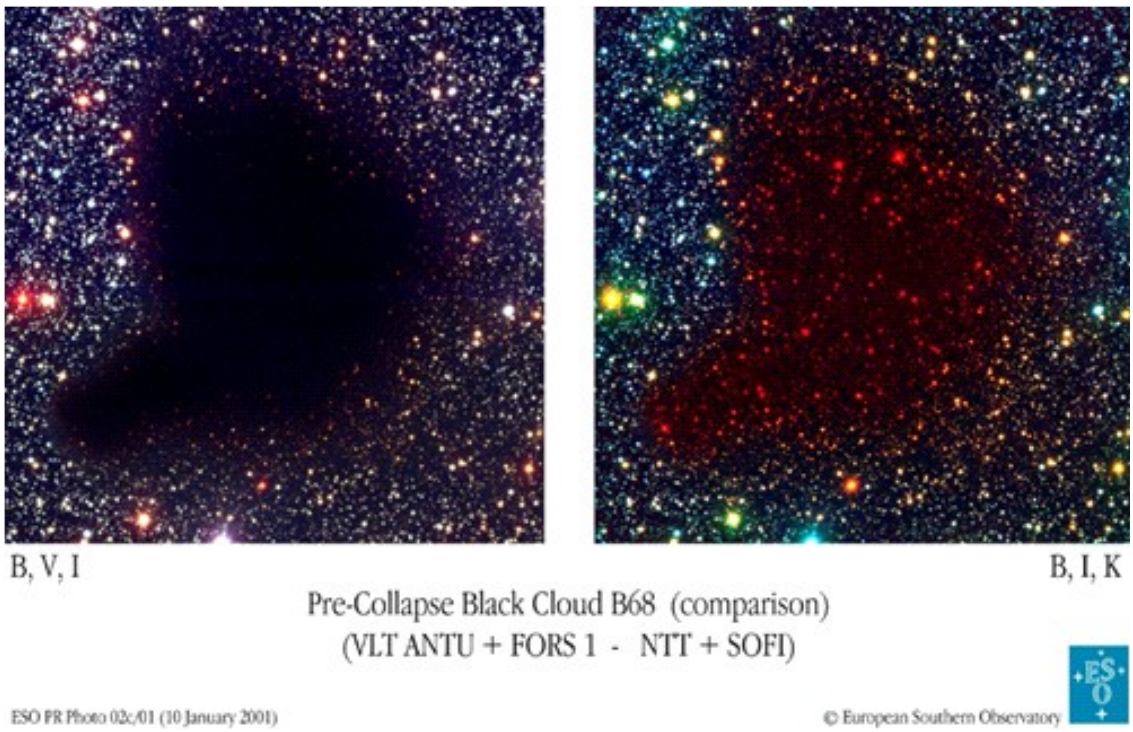

Figure 2: This figure shows a molecular cloud in the visible (left) and infrared (right) spectrum. Visible light is scattered and absorbed by dust and gas (in a molecular form with higher density of states) in a process known as interstellar extinction. Consequently, molecular clouds appear as dark or reddened clouds in the visible or IR spectral range respectively in the ISM. [26]

Consequently, dust grain and gas phase temperatures are lower in molecular clouds than diffuse clouds, at around 10K and 30K respectively (as shown in Table 2). As molecular clouds are shielded from destructive UV and X-rays, a rich variety of ISM molecules are formed and detected, which strongly suggests that there is a significant amount of chemistry occurring in this ISM region[3,16,25,27,28]. This chemistry can occur, to a limited extent, in the molecular cloud gas phase. However, most of these molecules are believed to form through surface chemistry on the surfaces of icy dust grains which is discussed in detail below.

1.2.3 Gas phase Chemistry

Most exothermic chemical reactions in the gas phase of molecular clouds have high activation energy barriers, typically between 0.1-1 eV, as existing chemical bonds

within molecules must be broken to allow more complex molecules to form[2]. Therefore, as molecular cloud temperatures are around 10K, (or $k_BT = 0.001$ eV, where k_B is Boltzman's constant and T is the temperature) neutral-neutral endothermic gas phase chemistry is highly improbable. Work carried out by Simms et al.[29], found that rate constants in the ISM are significantly higher than predicted by the Arrhenius equation, but nevertheless arrives at the same conclusion. In addition to this, exothermic reactions are also prohibited as the thermal energy released during the reaction breaks any chemical bonds which were previously formed. Consequently a third body is needed to allow exothermic reactions in the ISM, but the probability of such 3-body interactions is extremely low in the ISM due to the extremely low gas density. However, reactants adsorbed onto the surface of dust grains can undergo exothermic reactions as the dust grain acts as a third body . Therefore, most of a molecular cloud's chemical abundance is governed by surface chemistry rather than gas phase chemistry.

Gas Phase Chemistry	**Surface Chemistry on Icy dust grain mantles**			
CO	AlCl	C_2S	HCNO	H_3CNH_2
CH_3^+	AlF	C_2P	HNCO	CH_2CHCN
CH_3OH	AlO	CO_2	HNCS	H_2CHCOH
OH	C_2	H_2C	NH_3	C_6H
CO_2	CH	H_2O	HSCN	HC_4CN
	CN	H_2S	SiC_3	CH_3CHO
	CO	HCN	C_5	H_3CC_2CN
	CP	HCO	CH_4	$H_2COHCHO$
	CS	HCP	*c*-C_3H_2	$HCOOCH_3$
	FeO	HNC	*l*-H_2C_3	CH_3COOH
	H_2	HNO	H_2CCN	H_2C_6
	HCl	KCN	H_2C_2O	CH_2CHCHO
	HF	MgCN	H_2CNH	CH_2CCHCN
	HO	MgNC	C_4H	C_7H
	KCl	NH_2	HC_3N	NH_2CH_2CN
	NH	N_2O	HCC-NC	CH_3C_4H
	N_2	NaCN	HCOOH	CH_3OCH_3
	NO	NaOH	NH_2CN	CH_3CH_2CN
	NS	OCS	HC(O)CN	CH_3CONH_2
	NaCl	O_3	SiC_4	CH_3CH_2OH
	NaI	*c*-SiC_2	SiH_4	C_8H
	O_2	SiCN	*c*-H_2C_3O	HC_7N
	PN	SiNC	C_2H_4	CH_3CHCH_2
	PO	SO_2	CH_3CN	
	SH	CH_3	CH_3NC	
	SO	*l*-C_3H	CH_3OH	

	SiC	*c*-C_3H	CH_3SH	
	SiN	C_3N	*l*-H_2C_4	
	SiO	C_3O	$HCONH_2$	
	SiS	C_3S	C_5H	
	AlNC	C_2H_2	HC_2CHO	
	AlOH	H_2CN	HC_4N	
	C_3	H_2CO	CH_2CNH	
	C_2H	H_2CS	*c*-C_2H_4O	
	C_2O	HCCN	CH_3C_2H	

Table 3: Table listing ISM molecules produced by Gas and Surface chemistry on dust grain surfaces. It is clear from this table that the vast proportion of ISM molecules are produced on dust grain icy mantles.

Table 3 above clearly illustrates how significant dust grain surface chemistry is, and its profound role in astrochemistry. Water ice mantles on icy dust grains are responsible for much of the chemical diversity in the ISM, which in turn is pivotal in star, planet and comet formation, and therefore also pivotal for the origin of life in the universe.

1.2.4 *Surface Chemistry*

There are generally considered to be two types of surface chemistry; the Langmuir-Hinshelwood and Ely Rideal mechanisms. The latter corresponds to the case where reactants physisorb onto a surface and react via surface diffusion, while the former corresponds to the case where a reactant is chemisorbed and pinned onto a surface and incoming reactants bond with this chemisorbed reactant. In both cases the final products are generally desorbed back into the gas phase due to high exothermic reaction energies. Atomic hydrogen chemisorbs onto dust grain surfaces in diffuse regions, leading to the formation of molecular hydrogen and water via an Ely Rideal surface chemistry. Over time this physisorption-reaction-desorption-re-accretion process results in the formation of an ASW icy mantle, which consequently results in the formation of new and more complex molecules on dust grain surfaces[17]. However, given the

powerful photodissociative environment in diffuse clouds most dust grains here are bare, and only dust grains which are shielded from stellar radiation (for example in molecular clouds) possess icy mantles. As gas and dust grain temperatures are lower in molecular clouds, physisorption is much more prevalent than chemisorption because incoming reactants have lower velocities and cannot overcome the activation energy barrier to chemisorb onto the surface. Consequently, molecules physisorb onto dust grain surfaces forming icy mantles[3,6,16] which are predominantly water ice[3,16,17] with CO ice being the next most abundant ice species[16]. Figure 1.3 below illustrates the difference between dust grains found in diffuse and molecular clouds.

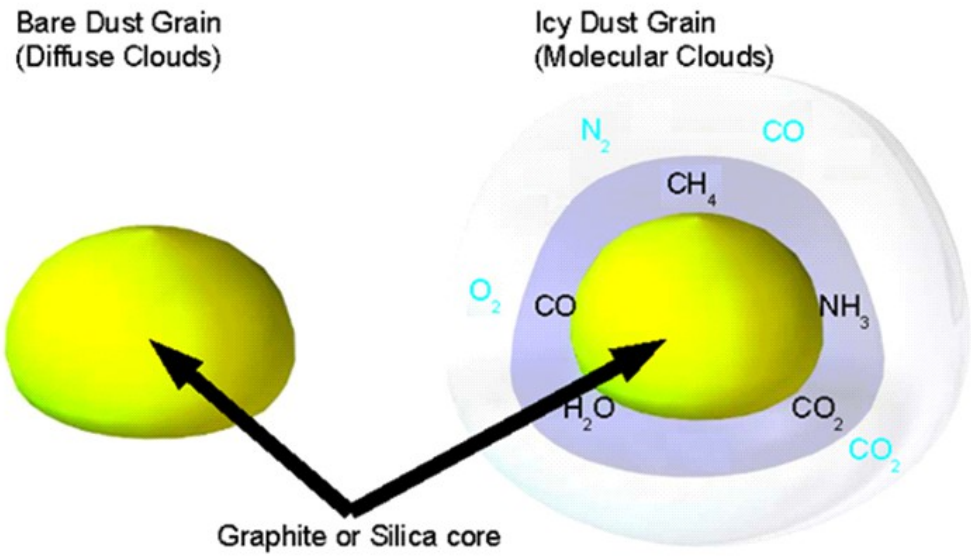

Figure 3: This figure shows bare and icy dust grains found in the ISM. Bare dust grains are prevalent in diffuse regions of the ISM due to the prevalence of photodissociative radiation emitted from nearby stars. As gas phase temperatures are lower in molecular clouds due to the increased density of states, dust grains are better shielded from stellar radiation. Consequently, dust grain surfaces have lower temperatures, resulting in molecules"freezing out"on dust grain surfaces to form icy mantles. These icy mantles are predominantly water with CO2 being the next most abundant ice species[31,32].

These icy mantles promote surface chemistry, which is far more productive than gas phase chemistry, through several mechanisms[8]. The process begins with physisorption

of gas species (atoms, molecules, or radicals) on icy mantle binding sites, also known as accretion, with near 100% sticking efficiency[8].

Due to the low dust temperatures in molecular and diffuse clouds in the ISM these adsorbed species generally form a solid phase, further adding to the icy mantle. This adsorption process causes energy, generally in the form of intra red radiation, to be released. Laboratory based experiments[29,30] have shown that the sticking efficiency for this process is almost 1, i.e. re-sublimation is highly improbable. Therefore, icy mantles and dust grains absorb this physisorption (impact) energy which increases surface mobility. Water is believed to form when oxygen combines with molecular H_2 or individual hydrogen atoms on dust grain surfaces. The thermal energy released during this exothermic reaction is then absorbed by the dust grain and re-emitted as radiation[34]. This process of water formation is known as chemical vapour deposition. These icy mantles act as a catalyst by increasing molecular collision rates by an order of magnitude on icy mantles when compared with collision rates in the gas phase. Furthermore, through Langmuir-Hinshelwood surface chemistry, activation energy barriers are significantly reduced resulting in the formation of more complex molecules whose formation is much less likely via gas phase chemistry.

All water structures absorb in the near to short wavelength infrared region. However, water has different absorption signatures depending on its state (gas, liquid or solid), with IR absorbance at 3800 – 3600, 3600 – 3000 and 3400 – 3000 for water vapour, liquid and cubic ice respectively. Amorphous ices such as LDA and HDA absorb in the region between liquid water and cubic ice as shown in Figure 4 below.

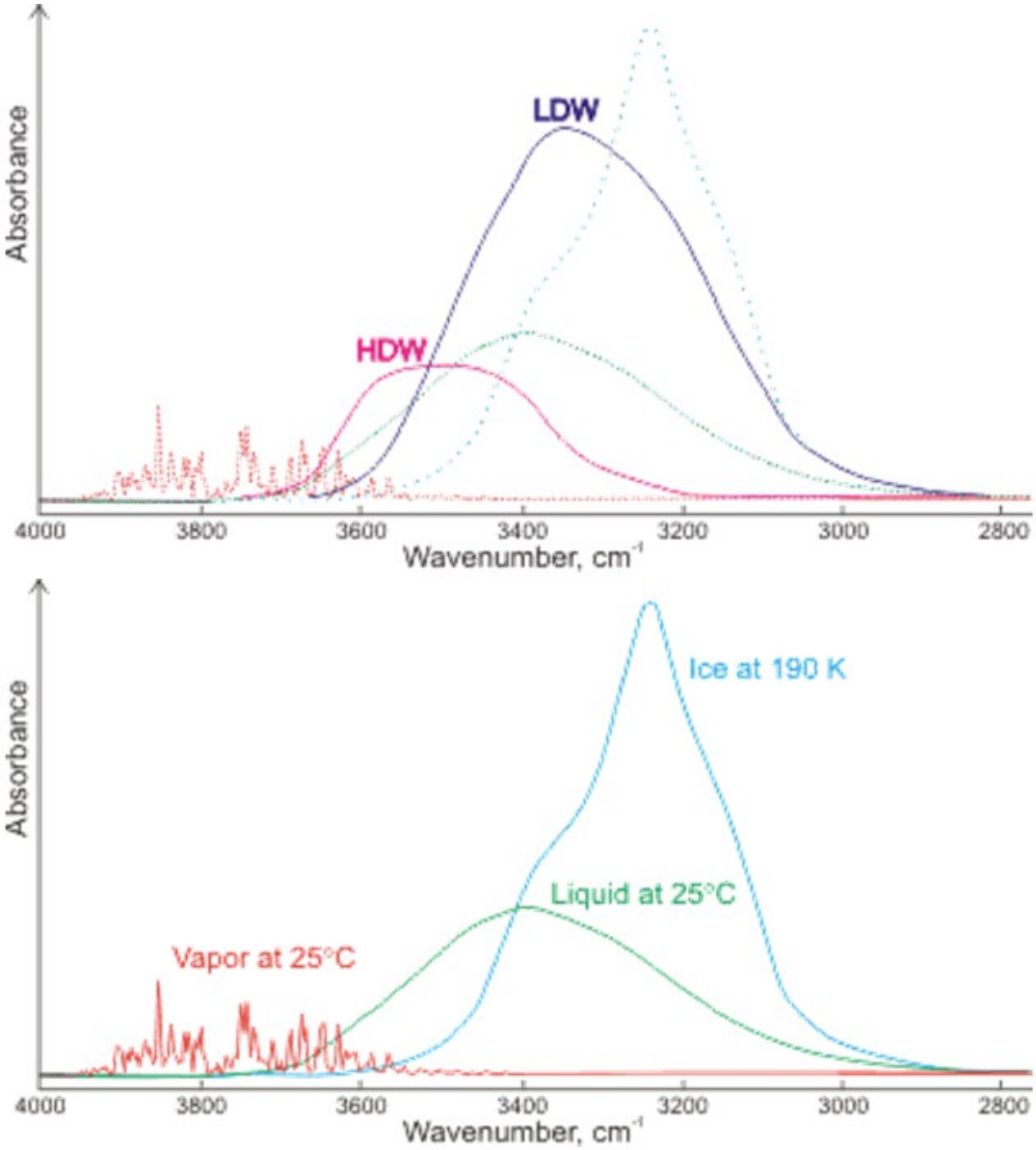

Figure 4: This figure illustrates how different water structure have different Infra red absorption spectra[20]. Amorphous ices and liquid water have a higher wavelength absorption than a more crystalline ice structure like cubic ice.

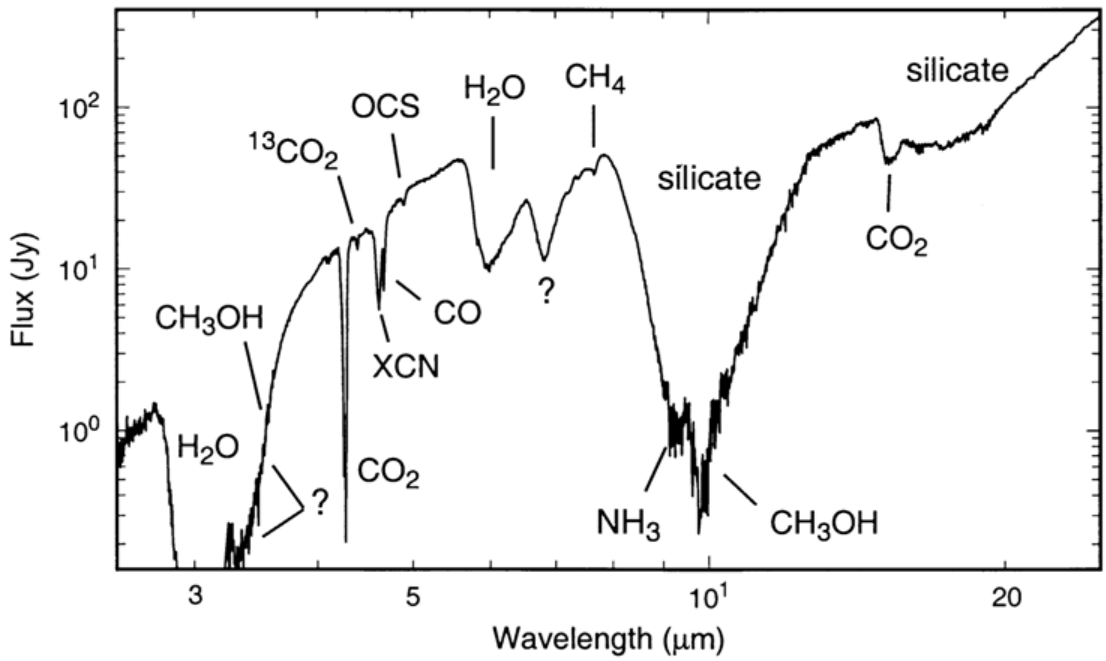

Figure 5: Shows the absorption spectra from the ISO SWS telescope for the embedded protostar w33a. The principal identified and unidentified spectral features are labelled. The water signatures at 3 - 3.5 and 6μm suggest that icy mantles are amorphous as O-H bonds are being stretched and bent respectively[16].

Results from the Infrared Space Observatory Short Wavelength Spectrometer (ISO SWS)[16] shown in Figure 5 indicate that water ice is the most abundant ice species in the universe due to this IR peak at 3 – 3.5 and 6μm. Figure 4 above suggests that this water ice is a combination of crystalline and amorphous ice. This is further reinforced by the O-H stretching and bending features between 3 – 4.5 and 6μm respectively suggesting that icy mantles are amorphous.

1.2.5 Star forming regions/protostellar disks

As mentioned previously bare dust grains in the diffuse ISM, and the abundance of molecular hydrogen and CO_2 in molecular clouds maintains a dense core temperature of around 10K. This allows vital chemical processing in this ISM region through surface chemistry on dust grain surfaces, producing, among other species, molecular hydrogen which is pivotal for star formation. In molecular clouds gas and gravitational pressure counteract each other creating a stable equilibrium. However, as molecules "freeze out" on dust grain surfaces the gas phase pressure decreases and this region of

the molecular cloud is subject to gravitational collapse (shu model[35]), producing a Prestellar object.

1.2.6 *Prestellar Cores*

Prestellar objects have comparatively higher densities than molecular clouds , typically 10^{6-7} atoms cm^{-3}. However, the prestellar envelope and core temperature remains at 10K[13]. Prestellar objects are densest at the core, with outer shells decreasing in density, and are comprised almost entirely of molecular hydrogen and helium. It is currently believed that the abundance of CO in prestellar objects is 1-2 orders of magnitude lower than in molecular clouds[13].

1.2.7 *Protostellar Cores*

Further gravitational collapse of prestellar cores results in an increase in core temperature. During this process molecular hydrogen dissociates into atomic hydrogen, allowing nuclear fusion to occur producing a protostellar core[36,37]. The thermal radiation emitted from this protostellar core evaporates icy mantles on icy dust grains releasing complex molecules back into the gas phase. Furthermore, this radiative pressure disperses surrounding matter in the protostellar envelope as shown in Figure 6. In doing so the radiative pressure within the protostellar core decreases, resulting in further gravitational collapse. Angular momentum is conserved during star formation therefore gas and dust grains from the collapsing envelope form a protostellar disk around this protostellar core.

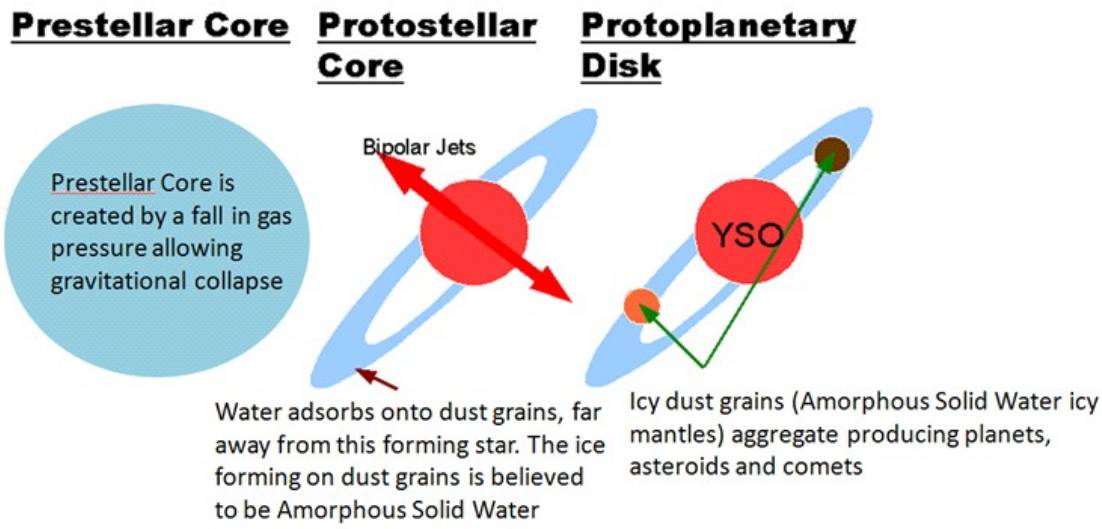

Figure 6: Illustrates the crucial role Amorphous Solid Water (ASW) plays in star, planet, asteroid and comet formation in the universe. The initial drop in gas pressure which results in a prestellar core is due to molecules "freezing out" on ASW icy dust grains. The prestellar core's intense thermal radiation evaporates ASW icy mantles which then re-condense on dust grain surfaces far away from the star forming region. In addition to this, Bipolar jet C-shocks provide sufficient energy for molecular hydrogen to combine with oxygen producing gas phase water which also condenses on dust grain surfaces far away from the star forming region. As this prestellar core stabilises and becomes a young stellar object (YSO), ASW icy mantles aggregate to form planets, asteroids and comets.

during this protostellar phase, two bipolar jets[36] form on the magnetic north and south poles of this protostellar core and are shockwaves of protostellar matter which typically have speeds around 25 km/s during this process dust grains located near the north and south poles of this protostellar object are sputtered and destroyed, further defining the protostellar disk. If these bipolar jets have a velocity less or greater than 50 km/s they are classed as C-type and J-type shocks respectively, C-type shocks maintain hydrodynamic consistency (with regards to density and temperature) and molecular hydrogen does not dissociate and can form water with free oxygen atoms provided the gas envelope temperature is around 200K[2]. This is significant as water can then physisorb back onto distant dust grains under cooler conditions (re-condensation) through physical vapour deposition, forming an amorphous solid water icy mantle which is pivotal for planet, asteroid and comet formation in the universe.

1.2.8 *Protoplanetary Disks*

After approximately a million years the bipolar jets cease and the protostellar core becomes a young stellar object (YSO), stabilising to form a new star. Molecules produced in the shock regions through gas phase chemistry, mostly water, once again freeze out on dust grains surfaces[2] in the protostellar disk midplane where densities are high and temperatures are approximately 10K (far away from the YSO). In addition to this, icy mantles desorb off dust grains that are closer to the protostallar core and also freeze out on dust grain surfaces in the protostellar disk midplane far away from the YSO. In both cases, water is being deposited onto bare dust grains surfaces through physical vapour deposition. It is believed that icy dust grains aggregate around the equatorial plane to form planets, comets and asteroids; which cannot form at larger heights above the equatorial plane due to the abundance of UV rays as shown in Figure 6. Work by Fraser et al.[3] states that popular theory suggests that comets form on the outer bounds of the protoplanetary disk.

1.3 Questions remaining about ISM ASW

As stated in the previous section water deposited onto bare dust grain surfaces by PVD produces ASW icy mantles which play a pivotal role in planet, asteroid and comet formation in the universe. What do we know about ISM ASW dust mantles? Laboratory based experiments[21,29,34,38-42] have found that ASW grown under ISM-like conditions is porous, and its porous structure is strongly dependant on deposition conditions. This porosity generally increases with increasing deposition angle (that is, the angle between the trajectory of a depositing water molecule and the normal to the substrate) and with decreasing substrate temperature. Donev et al.[40] performed an experimental study of lab-grown ultra thin ASW films using non-contact atomic force microscopy and found that a colder substrate limits surface diffusion, which in conjunction with a tetrahedral hydrogen bonding network allows water to form hemispherical clusters[40] on the substrate. Larger deposition angles (with respect to surface normal) produce a more porous ASW due to shadowing as explained later in section 1.4. As stated in section

1.2.4, spectroscopic observations[7,8] have shown that ASW in the ISM is porous and amorphous with no sign of dangling hydrogen bonds being present. Dangling hydrogen bonds are important because they act as icy mantle absorption sites, and the more absorption sites an icy mantle has the more chemical processing can occur via surface chemical mechanisms (Langmuir-Hinshelwood and Ely Rideal). These dangling hydrogen bonds are also thought to lower the free energy reaction barriers[3] to allow more complex molecules to form, in this way ASW is thought to act as an 'astrochemical catalyst' in the ISM. However, very little is known about the following important issues:

- How does ASW act as a catalyst allowing more complex molecules to form in the ISM, given that there is no spectroscopic evidence of dangling hydrogen bonds in observational studies, but are observed in laboratory studies?
- How and why does ASW form porous structures, observed both in lab experiments and indirectly via spectroscopic measurements of the ISM, which are pivotal for planet, asteroid and comet formation?
- Does bare dust grain surface type and structure have an impact on ASW structure?
- How do deposition kinetics affect overall ASW structure?
- How does ASW structure affect chemical reactivity at the surface?
- Does ASW structure differ between the two deposition methods; chemical vapour deposition (CVD) and physical vapour deposition PVD?
- How sensitive is ASW structure to temperature, and to what extent does it anneal over long timescales?

Previous work in the literature that goes some way to addressing these issues is discussed next, but we will see that there remain many unresolved issues.

1.4 Studying ASW

ASW has been studied in laboratories under conditions similar to those in the ISM.

Laboratory studies can simulate low ISM temperatures (50-10K) using cryostats, but it is currently not possible to replicate the ISM gas density even with ultra high vacuum (UHV) equipment. Previous laboratory based experiments have managed to grow ASW on cold Gold[40], Graphite[41] and Aluminium[43] substrates using "background deposition", where water molecules are deposited at room temperature. Such vapour deposition experiments have shown that ASW morphology is fundamentally dependant on deposition kinetics. The above experimental studies measure macroscopic material properties such as density and desorption rates of ASW. Yamamuro et al.[39] carried out vapour "background deposition" experiments on a colder substrate (~8K) than previous experiments. When comparing vapour deposited ASW (8K), an annealed ASW sample (heated to 120-125K), and hexagonal and cubic ices structures (160K and 240K respectively), it was found, as expected, that the number of hydrogen bonds in vapour deposited ASW was less than in crystalline ices. Heating ASW to ~120K (annealed sample) resulted in a more ordered structure. Dohnalek et al.[44], using a quasi-effusive molecular beam where water molecules are deposited at room temperature into a UHV chamber maintained at 22K onto a platinum substrate at the same temperature, concluded both experimentally and theoretically that molecular trajectories normal to the substrate produce a highly dense and compact ASW structure, whereas random ballistic deposition trajectories produce a more porous and comparatively less dense structure.

Other experiments[40] have measured vapour deposited ASW topology using atomic force microscopy (AFM) with an accuracy of ~0.1nm, probing ASW surface topology but neglecting ASW internal structural properties. It was found that water forms hemispherical structures during deposition and that the lower the surface temperature the more concentrated the clusters. The study also reports that increasing the deposition temperature results in incoming water molecules absorbing on the sides of ASW clusters, aiding lateral growth. Interestingly, they state that there are two stages to ASW formation; firstly a nucleation phase where the hemispherical structure forms and secondly, a coral like dendritic structure phase.

Also, recent work carried out by Bowron et al.[41] attempts to investigate ASW

structural properties through neutron scattering experiments. However, before results from neutron scattering experiments can be obtained, the microporous ASW sample in this work is heated to 120K, relatively close to the cubic ice phase transition temperature at about 140K as stated by Jenniskens et al.[21]. Heating the ASW sample to such a high temperature produces a more crystalline and compact ASW. This explains why the resulting ASW radial distribution functions (RDFs) bear close resemblance to hyperquenched glassy water (HGW) RDFs.

Two recent papers investigate the effect of ASW surface morphology on desorption kinetics. Hornekaer et al.[43] showed that increased ASW surface porosity and film thickness increased deposited molecular hydrogen binding energies. Furthermore, upon heating the ASW sample its porosity decreased, with collapsing pores trapping molecular hydrogen within the ASW bulk phase. Fillion et al's work[45] supports that of Hornekaer et al, and in addition studies how atomic hydrogen recombines on ASW films producing molecular hydrogen (H_2, HD or D_2). Wang et al.[46], investigate icy dust grain aggregation kinetics and find that the dielectric properties of ASW increases icy dust grain interaction energies, aiding dust grain aggregation. They also find that ASW's inelastic mechanical properties, and its porous properties, act as an energy dissipation mechanism during collisions, where energy is dissipated through ASW sublimation.

1.5 Studying ASW using Molecular Dynamics

It is very challenging to measure the molecular scale structure of sensitive amorphous materials such as ASW experimentally. But this task is easily achieved with molecular dynamics (MD) simulations, which can be viewed essentially as 'virtual experiments' with molecular scale resolution. Provided the empirical potentials and classical trajectories of MD simulations accurately mimic natural processes then results from these simulations can be very useful and valuable, which is why they are popular in many areas of science. Experimental studies of ASW are expensive and it is difficult to accurately replicate conditions in the ISM or systematically study the effect of a number of important parameters. However, ASW can be studied more easily with MD

simulation. For example, by using MD we can study how ASW structure evolves as a function of height above the substrate, and as a function of time. We can also set the deposition temperature much lower than that of room temperature; this has so far not been achieved in experiments. In addition, an MD ASW simulation employing random ballistic deposition can achieve higher deposition angles (relative to the substrate normal) than achievable experimentally, which allows more effective investigation of shadowing effects. As ASW structure is thought to be strongly dependant on deposition kinetics this MD approach should produce a more realistic ISM icy mantle ASW structure.

A key advantage of MD compared to current experimental methods is that an MD study can recreate ISM conditions more precisely, in terms of the gas phase density and temperature. With MD gas phases of arbitrarily low density can be simulated, and through the application of simulated 'thermostats' the substrate (ISM dust grain) and ASW (icy mantle) temperature can be regulated consistent with ISM molecular cloud temperatures (10-50K).

1.5.1 Physical and Chemical vapour deposition (PVD and CVD)

This thesis will study PVD of water on ISM dust grain substrate models using MD. Initially CVD simulations were considered instead of PVD as they would model the initial ASW formation on ISM dust grains in molecular clouds more accurately. However, there are several problems in using MD to simulate CVD. First, MD simulations are classical simulations based on Newtonian mechanics and are therefore unable to properly simulate quantum effects. Quantum dynamical simulations are much more demanding computationally, and would considerably limit the size of ASW clusters that could be studied. For example, MD simulations are unable to accurately simulate chemical reactions, something essential for CVD. For chemical reactions quantum Monte Carlo simulations such as those carried out by Huppen et al.[47] to obtain rate constants can be used. Alternatively, ab-initio simulations, based on solution of the Schrodinger wave equation could be used. However, all these quantum methods are computationally very expensive. Ultimately, classical simulations are the only reasonable method available for modelling the porous nature of large ASW clusters.

As described earlier (see section 1.2.4), the formation of ASW on bare dust grains in molecular clouds occurs through CVD. But this cannot be modelled using classical Newtonian MD simulations. However, as mentioned in section 1.2.7, during the protostellar phase of star formation water desorbs from dust grains surfaces close to the protostellar object and as described in section 1.2.8 then re-adsorbs on dust grains through PVD far away from the forming star. Therefore modelling ASW formation through PVD using classical MD simulations could accurately model the formation of icy mantles on distant ISM dust grains, which eventually form the protoplanetary phase where planets, asteroids and comets form.

1.6 Thesis objective and outline

This thesis will attempt to model ISM ASW by using a PVD MD algorithm and in doing so answer some of the important questions regarding ISM ASW. As mentioned in section 1 dust grains are mainly silica or graphite in composition. This means that dust grains can either be hydrophobic (graphitic) or hydrophilic (siliceous) in nature, posing the obvious question - how does ISM dust grain surface morphology effect ASW structure? Growing ASW on both hydrophobic and hydrophilic surfaces under ISM conditions through PVD MD simulations will attempt to answer this question. Another question concerns the effect of water deposition temperature on ASW structure? Using PVD MD simulations the growth of ASW on both kinds of dust grain surface over three deposition temperatures (50, 150 and 300K) will be studied. The 300K deposition temperature is used at it closely compares to most laboratory based ASW growth studies in which dangling O-H bonds are reported, in contrast to observational studies where no O-H dangling bonds are found. Therefore, investigating ASW formation under a range of different deposition temperatures should reveal how and why O-H dangling bonds form in ASW and shed some light on the catalytic properties of ASW.

This thesis will also investigate ASW morphology (hydrogen bonding network, density, radial distribution functions), and how it changes as a function of height above the substrate, for both hydrophobic and hydrophilic dust grain surfaces. This study will analyse ASW morphology after PVD water deposition, which will provide extensive data on ASW static properties but reveal little about how these structures grow.

Therefore this thesis will also perform a detailed study of the growth process of ASW on each surface for each deposition temperature.

In summary the four main objectives of this work in relation to PVD of ASW are:

- To understand ASW morphology overall and as a function of height above both a hydrophobic and hydrophilic ISM dust grain surface.
- To understand how deposition temperature affects overall ASW structure on both dust grain surfaces, and if dangling hydrogen bonds are present.
- To investigate ASW growth mechanisms during PVD water deposition and its role in producing ASW structures.
- To understand how ISM dust grain surface hydrophobicity effects growth of ASW

Chapter 2 will give a general introduction to molecular dynamics theory. Chapter 3 will detail the PVD MD strategy, theory and algorithm. Chapter 4 will present ASW measuremets and results for all deposition temperatures for both hydrophobic and hydrophilic dust grain surfaces. Chapter 5 will investigate growth mechanisms, and chapter 6 will provide a summary of this work and indications of future directions of research.

2. Molecular Dynamics

Macroscopic material properties are produced as a result of what transpires at the atomic level. In particular intramolecular and intermolecular interactions and kinetics ultimately govern the thermodynamic and structural properties of all materials. It is possible using Newtonian mechanics to derive an analytical solution for just two interacting bodies[48]. However, materials consist of a lot more than two bodies and it is currently not possible to analytically solve such "many body systems". There is however, a way to avoid this obstacle; by employing numerical algorithms and approximate theoretical models one can model the approximate physical behaviour of many body systems.

Molecular dynamics (MD), is a computer simulation technique for numerically solving Newton's equations of motion for many body molecular systems. MD simulations can provide an accurate description of much of the behaviour of many molecular systems if the interaction potentials are suitably calibrated. One has to assess the significance of non-classical, i.e. quantum, effects for each situation. These effects occur if the interparticle distance is less than the thermal de Broglie wavelength. Generally particles at low temperature or with small atomic masses will be subject to quantum effects as can be seen from the de Broglie equation and Table 4 below:

$$\lambda = \sqrt{\frac{h^2}{2\pi m k_b T}} \tag{2.1}$$

	Atomic Weight	300K	50K	10K
Hydrogen	1	1	2.46	5.49
Helium	4	0.5	1.23	2.76
Oxygen	16	0.25	0.62	1.38
Water	18	0.24	0.58	1.3

Table 4: Shows the thermal De Broglie wavelength for hydrogen, helium, oxygen and water in angstroms for three different temperatures 300K (room temperature), 50K (ISM molecular cloud temperature) and 10K (lower ISM molecular cloud temperature)

Even if quantum effects are small, a limitation of classical MD simulations is the accuracy of the potential energy models describing interactions between molecules. Naturally, the first step in any MD simulation strategy is to derive or obtain a sufficiently accurate intermolecular potential. These potentials are commonly divided into two components; short and long range potentials.

2.1 Short Range Potentials

Short range pair-potentials attempt to model the interactions that occur between all atoms. They comprise a very short ranged repulsive interaction that arises from the Pauli exclusion principle for electrons, and a longer ranged attractive London or dispersion interaction which arises from induced dipole – induced dipole interactions [49].

Three body interaction potentials, that arise from the electron-shell deformation between neighbouring molecules are needed in principle, but in practice it is generally found that well calibrated pair-potentials, that effectively incorporate some 3-body effects, are sufficient for many situations. Recent work by Sadus et.al. [50-53] and Nasrabad and Bukowski[54,55] has showed that three body interaction potentials are superior to two body potentials (such as the Lennard-Jones and Buckingham potentials) in accurately modelling the dipole moment for water and radial distribution functions [52]. However, in our simulations of a porous solid at very low temperature we expect ASW structure to be dominated by very short ranged pair-interactions that model

hydrogen bonds, and consequently three body interactions should not be significant. Moreover, pair-interactions are less expensive computationally, and so are generally used in molecular simulation studies. Two of the most widely used short range potentials are the Lennard-Jones (2.2) and Buckingham potentials (2.3), shown below,

$$U(r_{ij}) = 4\epsilon\left[\left(\frac{\sigma}{r_{ij}}\right)^{12} - \left(\frac{\sigma}{r_{ij}}\right)^{6}\right] \tag{2.2}$$

$$U(r_{ij}) = A_{ij}\exp\left(-\frac{r_{ij}}{\sigma_{ij}}\right) - \frac{C_{ij}}{r_{ij}^{6}} \tag{2.3}$$

where U and r_{ij} are the potential energy and separation distance between atoms i and j respectively. σ and ε are the Lennard-Jones distance and energy coefficients respectively. A_{ij}, and C_{ij} are the energy parameters of the Buckingham potential. By fine tuning these parameters it is possible to model the repulsive and attractive short range interactions mentioned above. Using the Laplace equation

$$\vec{f}_{ij} = -\nabla U(\vec{r}_{ij}) \tag{2.4}$$

where

$$\nabla U = \frac{\partial U}{\partial x}\vec{i} + \frac{\partial U}{\partial y}\vec{j} + \frac{\partial U}{\partial z}\vec{k} \tag{2.5}$$

the force corresponding to the LJ potential is

$$\vec{f}_{ij} = \frac{24\epsilon}{r_{ij}^{2}}\left[2\left(\frac{\sigma}{r_{ij}}\right)^{12} - \left(\frac{\sigma}{r_{ij}}\right)^{6}\right]\vec{r} \tag{2.6}$$

Note, this only gives the force between a pair of atoms, or ‘interaction sites’. An

interaction site can represent an atom, or a group of atoms, or any other force centre. All interaction sites are defined relative to the body fixed frame of reference of a molecule. Therefore, by focusing on one site at a time (known as the ith site) and looping through site pair interactions with other sites (known as jth sites) one obtains the total force acting upon that ith site for a many body system. This summation scheme automatically incorporates Newton's 3rd law. It is important to note that if a molecule is represented by a rigid body, the potential energy and force between pairs of sites within that rigid molecule (intra molecular forces) are not computed. Consequently, applying Newton's second law one obtains molecular accelerations resulting from intermolecular forces as shown below.

$$m\ddot{\vec{r}}_i = \vec{f}_i = \sum_{k=1}^{M} \sum_{j=1}^{N} \vec{f}_{ikj} \tag{2.7}$$

where *N, M, j, k,* and *m* are the total number of sites in molecule k, the total number of molecules in the system; the jth site index, the kth molecule, and mass respectively. Molecular accelerations are integrated to give new molecular velocities and positions; this will be described later in the 2.4 section.

2.2 Boundary Conditions

Having discussed intermolecular potentials, we need to create an environment for this MD simulation to take place. A simulation cell is a 3 dimensional “work space”, or volume for MD simulations. The most convenient simulation cell is a cube; this cube will contain all molecules in the system, allowing molecules to interact within this simulation cell. Some systems have boundary walls which prevent molecules from escaping the simulation cell, whilst others, such as those in this thesis, employ periodic boundary conditions, attempting to simulate a bulk material. Fully 3-dimensional periodic boundary conditions can be considered to replicate the simulation cell in the x, y and z directions to infinity as shown in Figure 7 below.

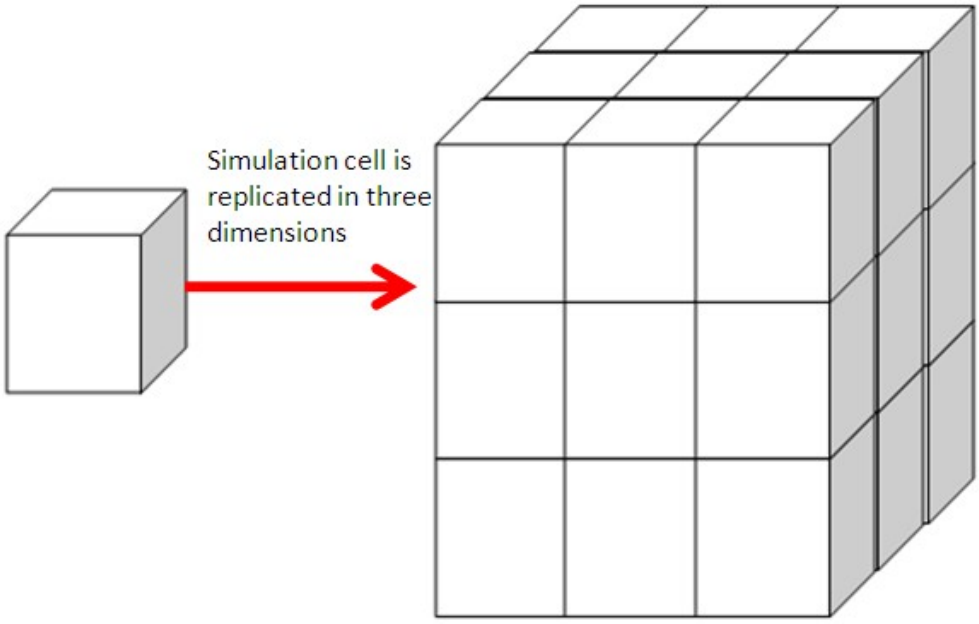

Figure 7: This figure illustrates how periodic boundarys work in MD simulations. The simulation cell is replicated in all three directions to simulate a bulk phase material.

Molecules leaving a simulation face will re-enter the opposite face, of the same simulation cell, keeping the number of molecules constant throughout the simulation. This method attempts to mimic an infinite simulation cell and is sometimes referred to as a "wrap around effect" [56] as molecules are wrapped around this simulation box. Furthermore, as molecules are free to cross simulation cell faces, molecules adjacent to face edges must interact with adjacent molecules on the opposite face. Consequently, potential energies, forces, and equations of motion are calculated using periodic boundary conditions. This means that molecular positions must be checked at every time step to ensure they are within the simulation cell boundaries; if a molecule lies out with this simulation cell it must be reinserted through the opposite face in order for the simulation to proceed. Even with periodic boundary conditions, if a simulation cell is not large enough results might be subject to finite size effects. In this case comparison of results for simulations of increasing size will reveal when a sufficiently large system has been simulated.

2.3 Cut-offs and Interaction Computations

To increase computational efficiency a cutoff radius is often applied to intermolecular potentials. This reduces the number of pair interactions that need to be calculated, since only jth molecules close to the ith molecule (typically a few molecular diameters) are included in potential energy and force calculations. This cutoff radius effectively cuts the potential energy between pair interactions, returning the potential energy to zero at intermolecular distances greater than the cut off radius. There is however a problem associated with applying a cut off radius as there is a stepwise change in potential energy at the cutoff. From equation (2.1) this produces an instantaneous impulse which leads to physically unrealistic results. Often, a 'ramp' function or 'shifted' potential circumvents this problem. A ramp function gradually increases the potential energy around the cut off radius allowing a smoother transition, whereas, a shifted potential shifts the whole potential energy to ensure there is no stepwise behaviour at the cutoff radius. Because we expect interactions between water molecules at the low temperatures studied in this thesis to be dominated by short ranged hydrogen bonds this kind of cutoff is expected to be reasonable provided the cutoff range is sufficiently large.

2.3.1 All pairs method

As the name suggests all molecular pair separations are calculated for the entire system. This method usually uses a cut off radius to increase computational efficiency. However, this method is hugely inefficient for large systems even with a cut off radius, as all intermolecular separations have to be calculated in order to ascertain which molecules lie within the ith molecule's cut off radius. As the computational effort scales as $O(N^2)$, where N is the number of molecules, this method is appropriate only for small systems.

2.3.2 Linked cells method

In order to overcome the computational inefficiencies of an all pairs method, the linked cell method attempts a more linear computational approach. It is obvious that the inherent problem with an all pairs method is that all molecular pair separations have to be calculated before a cut off radius is applied. In order to increase computational

efficiency a decrease in the amount of redundant intermolecular distances calculated is desirable. By dividing the simulation cell up into multiple mini simulations cells, each with a length greater than the cut off radius, where molecules are only allowed to interact with others in that mini simulation cell, and the next nearest mini simulation cell, it is possible to drastically reduce redundant intermolecular distance calculations. Such a method is more difficult to implement as it requires a more robust data structure where molecules have to be organised into a network, as accurate book-keeping of which molecule belong to which mini simulation cell is required. The computational effort scales as $O(N^{3/2})$ as only molecular pairs within each and neighbouring mini simulation cell are calculated therefore reducing the number of redundant intermolecular distances being calculated per MD cycle.

2.3.3 Neighbourhood lists

The Neighbourhood List method adopts a similar principle to that of the Linked Cells method. However instead of the simulation cell being divided up into mini simulation cells, a list of all molecules which "neighbour" the ith molecule is generated. This neighbourhood list consists of all the jth molecules which surround the ith molecule. Only molecules within the cut off radius are added to this list and distances are calculated accordingly. Neighbourhood lists have to be updated as molecules move with time. The Neighbourhood List method has an advantage over the Linked Cells method in that it can be applied to non-uniform systems as it is atom or molecular centric, linked cells can still be applied to non-uniform systems but as the number of atoms/molecules may vary greatly within each mini simulation cell for a non-uniform system it is more efficient and easier to use a neighbourhood list. For larger systems both the Linked Cells and Neighbourhood List methods can be used in conjunction to improve efficiency. The computational effort also scales as $O(N^{3/2})$ for the same reasons as described in section 2.3.2.

2.4 Integration algorithms

Once intermolecular forces have been calculated an integration algorithm then resolves molecular velocities and positions based on Newton's laws of motion. Integration algorithms in MD simulation should be simple due to the computationally demanding

interaction algorithms which scale as N^2 to $N^{3/2}$ as described in the sections 2.3.1, 2.3.2 and 2.3.3 above. Consequently, two straightforward algorithms are widely used in MD simulations: leap frog and Predictor-Corrector algorithms.

2.4.1 Leap frog

The most widely used integration method is that developed by Verlet in 1967[57], known as the Verlet or Leapfrog integration algorithm which is third order accurate. This method is also called a Leapfrog type algorithm because velocities and positions are computed for different time steps. By applying a Taylor series expansion around position *r(t)* we arrive at the Verlet integration algorithm as shown below

$$\vec{r}(t+h)=\vec{r}(t)+h\dot{\vec{r}}(t)+(h^2/2)\ddot{\vec{r}}(t)+O(h^3) \tag{2.8}$$

where *t*, *h*, $\dot{r}$ and $\ddot{r}$ are the current time, time step, velocity and acceleration respectively. By expanding in the opposite direction r(t – h) and substituting into equation (2.8) above we obtain the following.

$$\vec{r}(t+h)=2\vec{r}(t)-\vec{r}(t-h)+h^2\ddot{\vec{r}}(t)+O(h^4) \tag{2.9}$$

As the two third order terms cancel out to $O(h^3)$ this shows that the Verlet algorithm is third order accurate. To obtain velocities at the current time the following equation is used,

$$\dot{\vec{r}}(t)=\left[\vec{r}(t+h)-\vec{r}(t-h)\right]/2\mathrm{h}+O(h^2) \tag{2.10}$$

Derivation of the Leapfrog algorithm, which is algebraically identical to the Verlet algorithm, starts by re-writing equation (2.10),

$$\vec{r}(t+h)=\vec{r}(t)+h\left[\dot{\vec{r}}(t)+(h/2)\ddot{\vec{r}}(t)\right]+O(h^3) \tag{2.11}$$

Note that as $\dot{r}(t+h/2)=\left[\dot{r}(t)+(h/2)\ddot{r}(t)\right]+O(h^2)$ the Leapfrog algorithm for

calculating velocities and positions are shown below

$$\dot{\vec{r}}(t+h/2)=\dot{\vec{r}}(t-h/2)+h\ddot{\vec{r}}(t) \tag{2.12}$$

$$\vec{r}(t+h)=\vec{r}(t)+h\dot{\vec{r}}(t+h/2) \tag{2.13}$$

With this algorithm velocities and positions are calculated at different times, this presents no immediate problem. However, if velocities are required for the same time step as positions the equation below can be used.

$$\dot{\vec{r}}(t)=\dot{\vec{r}}(t\mp h/2)\pm(h/2)\ddot{\vec{r}}(t) \tag{2.14}$$

2.4.2 Predictor-Corrector

Predictor-Corrector algorithms (PC) are comparatively more computationally expensive and difficult to implement than leap frog type integration algorithms. However, this method is considerably more accurate than leapfrog algorithms. In addition to this, the user can also define to which order the integration algorithm is accurate. There are two types of PC algorithms. One computes new positions based on higher order accelerations over the same time step (Nordsieck); another calculates new positions based on accelerations from previous time steps (Adams-Bashforth). PC methods essentially attempt to solve a second order differential equation (acceleration) as shown below,

$$\ddot{\vec{r}}=f(\vec{r},\dot{\vec{r}},t) \tag{2.15}$$

There are two equations, *P(r)* and *C(r),* for predicting and correcting new molecular positions respectively. New molecular positions and velocities are predicted using the following *P(r)* equations.

$$P(\vec{r}):\vec{r}(t+h)=\vec{r}(t)+h\dot{\vec{r}}(t)+h^2\sum_{i=1}^{k-1}\alpha_i f(t+[1-i]h) \tag{2.16}$$

Using this Adams-Bashforth equation calculated positions are exact to within $O(h^{k+1})$ (assuming that $q \le k$). This is in contrast to the fixed 3rd order accuracy obtainable through leapfrog type algorithms. All symbols have their usual meanings. In order for this $O(h^{k+1})$ accuracy to hold the α_i coefficients must satisfy the set of k-1 equations [56].

$$\sum_{i=1}^{k-1}(1-i)^q\alpha_i=\frac{1}{(q+1)+(q+2)} \tag{2.17}$$

where q = 0, 1....., k - 2

Therefore coefficients are all rational functions. Predicted velocities are calculated as follows.

$$P(\dot{\vec{r}}):h\dot{\vec{r}}(t+h)=\vec{r}(t+h)-\vec{r}(t)+h^2\sum_{i=1}^{k-1}\alpha_i' f(t+[1-i]h) \tag{2.18}$$

with the following coefficients.

$$\sum_{i=1}^{k-1}(1-i)^q\alpha_i'=\frac{1}{q+2} \tag{2.19}$$

after the (1 – i) coefficients and f(t + h) are evaluated, the predictor part of this method is complete. Predicted positions and velocities are corrected using the following Adam-Moulton equations.

$$C(\vec{r}):\vec{r}(t+h)=\vec{r}(t)+h\dot{\vec{r}}(t)+h^2\sum_{i=1}^{k-1}\beta_i f(t+[2-i]h) \tag{2.20}$$

and for velocity correction.

$$C(\dot{\vec{r}}):h\dot{\vec{r}}(t+h)=\vec{r}(t+h)-\vec{r}(t)+h^2\sum_{i=1}^{k-1}\beta_i' f(t+[2-i]h) \tag{2.21}$$

Where position and velocity coefficients are shown below respectively.

$$\sum_{i=1}^{k-1}(2-i)^q\beta_i=\frac{1}{(q+1)+(q+2)} \tag{2.22}$$

$$\sum_{i=1}^{k-1}(2-i)^q\beta_i'=\frac{1}{q+2} \tag{2.23}$$

2.5 Orientational Integration algorithms

The previous section dealt with translational equations of motion and appropriate methods for integrating these equations of motion to obtain new molecular positions and velocities. However, it is sometimes more computationally efficient to group atoms within a molecule together as either rigid bodies or intra-molecular bonded bodies. When molecules are treated as a single rigid body, and not a flexible collection of bodies, forces act about the molecular centre of mass and the computational demand of the integration and force algorithms are greatly reduced, as intramolecular forces do not need to be calculated and integrated. In addition to this, the absence of intramolecular force calculations allows for larger time steps, which also reduces computation demand for MD simulations. Of course, rigid bodies cannot display the intramolecular dynamics of real molecules, and this can be a significant issue for some kinds of simulation, such as biomolecular simulations (protein folding for example). For the work in this thesis

involving water molecules, which are very small, we expect the rigid body approximation to be adequate. There are two methods for computing rotational dynamics; Euler angles and Hamilton's quaternions[58]. The use of quaternions to resolve rotational dynamics was first used by Evans et.al. in 1977[59], and is the most commonly used orientational integration algorithm in MD simulations. Both methods are similar in the sense that they calculate torques about a fixed centre of mass. However, there are major differences in how they compute angular displacements, velocities and accelerations. There are also two types of rigid body; linear and non linear, corresponding to two or three rotational degrees of freedom. An issue with rigid-body dynamics is that the three degrees of rotational freedom are coupled. This is due to the fact that angular moment around one axis is dependent on the angular momentum and moment of inertia about the other two axes; this is known as precession. The simulations use non-linear rigid water molecules, where water molecules are allowed to rotate freely about all three axes. Rotational dynamics are calculated based on two reference frames; a body fixed frame and an inertial fixed frame[57]. A body fixed reference frame is a local reference frame for a local rigid molecule, whereas an inertial fixed reference frame is fixed in free space independent of molecular orientational displacements. Both reference frames do not change with time. However, there are comparative changes between body and inertial fixed reference frames which account for orientational molecular displacements. Another way of conceptualising this is that the body fixed reference frame rotates with respect to the inertial reference frame.

2.5.1 Euler angles

Quaternions are most widely used in modern MD simulations. However, a description of Euler angles provides more insight in explaining the quaternion method. The first stage is to calculate rotational inertia about x, y, and z axes in the body-fixed reference frame based on the following definition.

$$I_{aa} = \sum_{i=1}^{N} m_i r_i^2 \tag{2.24}$$

where I_{aa}, *N, i, r,* and *m* are the moment of inertia about axis *a* (x,y,z), number of atoms within that molecule, atomic index, interatomic distance from the molecular centre of mass (which is also the axis of rotation), and the atomic mass respectively. A rotational matrix relates the body fixed and inertial fixed reference frames.

$$\vec{r}_b = R\,\vec{r}_s \tag{2.25}$$

where *R,* $\vec{r}_b$ and $\vec{r}_s$ are the rotational matrix, body fixed and inertial fixed displacement vectors respectively. The rotational matrix is a 3 x 3 trigonometric matrix consisting of Euler angles (θ, ϕ, ψ which are rotations about the x, y, z axes).

$$R = \begin{bmatrix} \cos\phi\cos\psi - \sin\phi\cos\theta\sin\psi & \sin\phi\cos\psi + \cos\phi\cos\theta\sin\psi & \sin\theta\sin\psi \\ -\cos\phi\sin\psi - \sin\phi\cos\theta\cos\psi & -\sin\phi\sin\psi + \cos\phi\cos\theta\cos\psi & \sin\theta\cos\psi \\ \sin\phi\sin\theta & -\cos\phi\sin\theta & \cos\theta \end{bmatrix} \tag{2.26}$$

It is important to stress that for rigid bodies, the position of sites within the body fixed referenced frame do not change with time. For example if there is a bond vector between two atoms its body fixed displacement vector components will remain unaltered. However, its inertial frame displacement vector will change with time. Atomic velocities are calculated simply by computing the vector cross product of molecular angular velocity and atomic position in the inertial fixed reference frame.

$$\dot{\vec{r}}_s = \dot{\vec{r}}_b + \omega_s \times \vec{r}_s = \omega_s \times \vec{r}_s \tag{2.27}$$

where ω_s is the angular velocity in the inertial fixed reference frame. Torques are computed on the body fixed reference frame. In MD simulations $\dot{L}^b$ is calculated from the vector cross product of forces acting on sites and site displacement distances from the molecular centre of mass.

$$T^b = \dot{L}^b + \omega^b \times L^b \tag{2.28}$$

where

$$\dot{L}^b = \vec{f} \times \vec{r_{cm}} \tag{2.29}$$

where $\dot{L}, L, T, \vec{f}, \vec{r_{cm}}$ are the rate of change of angular momentum (a torque), angular momentum, torque, force acting on site, and distance between site and molecular centre of mass respectively. When starting an MD simulation both $L^b, \omega^b, L^s, \omega^s$ are initialised to zero. Therefore, having obtained torques in the body fixed reference frame one can compute angular accelerations.

$$\dot{\omega}_x^b = \frac{T_x^b}{I_{xx}} + \left[\frac{I_{yy} - I_{zz}}{I_{xx}}\right]\omega_y^b \omega_z^b \tag{2.30}$$

$$\dot{\omega}_y^b = \frac{T_y^b}{I_{yy}} + \left[\frac{I_{zz} - I_{xx}}{I_{yy}}\right]\omega_z^b \omega_x^b \tag{2.31}$$

$$\dot{\omega}_z^b = \frac{T_z^b}{I_{zz}} + \left[\frac{I_{xx} - I_{yy}}{I_{zz}}\right]\omega_x^b \omega_y^b \tag{2.32}$$

These equations are for a body fixed reference frame so we need to use the rotational matrix to convert to the inertial fixed reference frame using the equation below. From an algorithmic point of view $\dot{\omega}^b, \dot{L}^b$ are then integrated (using either a Leapfrog type or PC integration algorithm) at this stage producing ω^b, L^b respectively, which will be reinserted into equation (2.28) for the next integration cycle after the new rotational matrix has been computed using the equations below.

$$\dot{\omega}^s = R^{-1} \cdot \dot{\omega}^b \tag{2.33}$$

Inertial fixed angular accelerations are integrated using either a Leapfrog type or PC

integration algorithm, as described previously, producing inertial fixed angular velocities. Euler angular rates can then be computed.

$$\dot{\phi} = -\omega_x^s \left(\frac{\sin\phi\cos\theta}{\sin\theta} \right) + \omega_y^s \left(\frac{\cos\phi\cos\theta}{\sin\theta} \right) + \omega_z^s \tag{2.34}$$

$$\dot{\theta} = \omega_x^s \cos\phi + \omega_y^s \sin\phi \tag{2.35}$$

$$\dot{\psi} = \omega_x^s \frac{\sin\phi}{\sin\theta} - \omega_y^s \frac{\cos\phi}{\sin\theta} \tag{2.36}$$

θ, ϕ, ψ can be obtained by using a leap frog type or PC integration algorithm. These new Euler angles are then inserted into the rotational matrix equation (2.26) and the process is iterated starting from equation (2.28).

2.5.2 Hamilton's Quaternions

The major limitation of using Euler angles is that there is singularity in computing Euler angles as shown in the equations above (when $\sin\theta \approx 0, \pi$). One way around this trigonometric singularity is to use Hamilton's quaternions. These quaternions are essentially a four dimensional vector representing a surface point on a four dimensional hypersphere. If one imagines a three dimensional sphere, any point on the surface of this sphere has an x, y, z coordinate. A hypersphere has these three coordinates plus an additional one for dealing with singularity at the north and south poles namely, x, y, z, and w. These four coordinates are normalised such that the magnitude of these vectors is equal to 1, and are normally expressed as q_1, q_2, q_3, q_4. The last quaternion represents the rotational component and is dimensionless; consequently, it is a redundant variable when computing new quaternions. These quaternions are defined in terms of Euler angles.

$$q_1 = \sin(\theta/2)\cos((\phi - \psi)/2) \tag{2.37}$$

$$q_2 = \sin(\theta/2)\sin((\phi-\psi)/2) \tag{2.38}$$

$$q_3 = \cos(\theta/2)\sin((\phi+\psi)/2) \tag{2.39}$$

$$q_4 = \cos(\theta/2)\cos((\phi+\psi)/2) \tag{2.40}$$

These quaternions are then normalised using the equation below.

$$\sum_{i=1}^{4} q_i^2 = 1 \tag{2.41}$$

Euler angles can be obtained using the following relations.

$$\sin\theta = 2\sqrt{(q_1^2+q_2^2)(1-q_1^2-q_2^2)} \tag{2.42}$$

$$\cos\theta = 1-2(q_1^2+q_2^2) \tag{2.43}$$

$$\sin\phi = 2(q_1q_3+q_2q_4)/\sin\theta \tag{2.44}$$

$$\cos\phi = 2(q_1q_4-q_2q_3)/\sin\theta \tag{2.45}$$

$$\sin\psi = 2(q_1q_3-q_2q_4)/\sin\theta \tag{2.46}$$

$$\cos\psi = 2(q_1 q_4 + q_2 q_3)/\sin\theta \tag{2.47}$$

Substituting the above relationships into the rotational matrix described above produces the following rotational quaternion matrix.

$$R = 2\begin{bmatrix} q_1^2 + q_4^2 - 1/2 & q_1 q_2 + q_3 q_4 & q_1 q_3 - q_2 q_4 \\ q_1 q_2 - q_3 q_4 & q_2^2 + q_4^2 - 1/2 & q_2 q_3 + q_1 q_4 \\ q_1 q_3 + q_2 q_4 & q_2 q_3 - q_1 q_4 & q_3^2 + q_4^2 - 1/2 \end{bmatrix} \tag{2.48}$$

There are now no trigonometric functions for evaluating the rotational matrix, this not only increases computational efficiency but also prevents the trigonometric singularity in determining Euler angles. Angular acceleration and velocity are computed using equation (2.28) to equation (2.32), as was the case with the Euler angles method. New quaternions rates are obtained using the equation below.

$$\begin{pmatrix} \dot{q}_1 \\ \dot{q}_2 \\ \dot{q}_3 \\ \dot{q}_4 \end{pmatrix} = \frac{1}{2} W \begin{pmatrix} \omega_x^b \\ \omega_y^b \\ \omega_z^b \\ 0 \end{pmatrix} \tag{2.49}$$

where

$$W = \begin{bmatrix} q_4 & -q_1 & -q_2 & -q_3 \\ q_1 & q_4 & -q_3 & q_2 \\ q_2 & q_3 & q_4 & -q_1 \\ q_3 & -q_2 & q_1 & q_4 \end{bmatrix} \tag{2.50}$$

Having obtained the quaternion rates, we now have to integrate using either a PC or Leapfrog algorithm to obtain the new quaternions. A simplified integration is shown in the equation below,

$$q(t+\delta t)=q(t)+\delta t\,\dot{q}(t) \tag{2.51}$$

Once the new quaternions have been calculated, they are then renormalised using above. Subsequently, the renormalised quaternions are then inserted into the rotational matrix before the process is repeated from equation (2.48) to equation (2.51).

2.6 Long Range Potentials

When atoms form chemical bonds with other atoms the centre of mass of electrons for both atoms are displaced from atomic nuclei, this gives rise to long range electrostatic forces. It is common practice to represent electrostatic interactions between molecules and ions in terms of partial charge sites. For 4 site water models an off-centre charge site attached to the oxygen atom via a spring, altering the dipole moment of individual water molecules, this is known as a drude oscillator. The interaction between dipolar and ionic species is long-ranged and special techniques, such as Ewald Summation[60] are required to handle these interactions. These long range interaction calculation methods are comparatively much more computationally expensive than those for short range interactions (by at least a factor of 5[61]) and omitting these interactions can, in many cases, adversely affect the accuracy of results. For long-ranged interactions the energy is computed by summing all pair interactions between charges in the central simulation cell and all the image cells.

2.7 Ensembles

Previous sections assume that the number of molecules N, simulation cell volume V and total system energy E are all constant; this is known as an NVE or microcanonical ensemble. Although this ensemble is commonly used, other MD ensembles such as NVT or NPT are particularly useful as they allow one to maintain a constant temperature and/or pressure when studying materials. DL_POLY also has a NST ensemble which maintains the system temperature and stress where the user can control the all the components of the stress tensor, which is important for analysing materials (such as polymers or metals) under stress.

2.7.1 NVT ensemble

An NVT ensemble maintains a constant simulation system temperature through the use of a virtual 'thermostat'. This thermostat, that represents the effect of a heat bath in good contact with the simulation cell, adjusts molecular velocities[56] so that they are consistent with a desired temperature. A consequence is that the energy of an NVT ensemble simulation is no longer constant. For a system at equilibrium it instead fluctuates around an average value, and the relative size of these fluctuations decreases as the system size increases. One such method is the Berendsen thermostat[48] which rescales molecular velocities as follows. First a scaling parameter, X, is calculated,

$$X = \sqrt{\left[1 + \frac{\Delta t}{\tau}\left(\frac{T_{ext}}{T} - 1\right)\right]} \tag{2.52}$$

where $\tau, \Delta t, T_{ext}$ and T are the relaxation time constant, time step, calculated system temperature, and desired system temperature respectively, where the calculated system temperature is

$$T_{ext} = \sum_{i=1}^{N} \frac{m_i \dot{r}_i^2}{n k_b} + \sum_{i=1}^{N} \frac{I_i \omega_i^2}{n k_b} \tag{2.53}$$

where N, n and k_b are the number of molecules, number of degrees of freedom and Boltzmann constant respectively. The number of degrees of freedom is three rotational and translational motions per rigid molecule. New velocities are calculated as follows.

$$\dot{r}(t + h/2) = \left[\dot{r}(t - h/2) + h\ddot{r}(t)\right] X \tag{2.54}$$

$$\omega(t) = \omega(t) X \tag{2.55}$$

2.7.2 NPT ensemble

In addition to applying a virtual thermostat, a virtual barostat can also be applied to maintain a desired system pressure by altering the simulation cell volume. A Berendsen barostat[48] cell vector coefficient, η, is calculated to scale the simulation cell volume to a desired value. At equilibrium the system volume will fluctuate around an average value and again, the relative size of these volume fluctuations decreases with increasing system size. The equations below show how Berendsen barostats operate in MD simulations,

$$\frac{\partial P_{ext}}{\partial t} = \frac{P_{ext} - P}{\tau_p} \tag{2.56}$$

where P, P_{ext}, τ_p and t are the calculated system pressure, desired pressure, pressure relaxation constant and time respectfully. The equation above states that greater fluctuations in pressure will result from smaller pressure relaxation constants. Berendsen barostat cell vector coefficients are estimated from the following equation.

$$\eta = 1 - \frac{\beta \Delta t}{\tau_p}\left(P_{ext} - P\right) \tag{2.57}$$

where η and β are the simulation cell vector coefficient and isothermal compressibility respectively. Cell vectors (x, y, z components of a cubic cell) are scaled as the cubic root of the simulation cell vector coefficient, $\sqrt[3]{\eta}$.

2.8 Macroscopic thermodynamics Properties

As with any simulation model, the model and its parameters must be validated by comparison with reference data. Once validated, a simulation can be used to make predictions provided it is used sensibly within its domain of validity. In order to validate the simulation model and make predictions it is necessary to understand how measurements of relevant physical parameters or phenomena can be made. Quantities

measurable through MD simulation are outlined below in terms of equilibrium and non-equilibrium properties.

2.8.1 Equilibrium

A system is in equilibrium if thermodynamically stable or metastable. Temperature is calculated using equation (2.53) above. The mass density (g/cm^3) is calculated as follows;

$$\rho = \frac{\sum_{i=1}^{S} m_i N_i}{V N_A} \tag{2.58}$$

where m, V, N_A, N and S are the atomic mass, simulation cell volume (in Angstroms), Avogadro's number (6.0221415×10^{23}), number of molecules in the simulation cell volume and number of different molecular species in the simulation cell respectively. Atomic distributions are measured via radial distribution functions, which measure the probability distribution for the separation of atoms of different kinds. This is measured by counting the average number, $n_j(r)$, of atoms of one kind, j, within a concentric sphere of thickness Δr and radius r centred on atoms of another kind, i. This average number is then normalised with respect to the expected number of j-atoms in the concentric shell assuming a uniform density of j-atoms in the simulation,

$$g(r_{ij}) = \frac{n(r_{ij})}{\gamma 4\pi r_{ij}^2 \Delta r} \tag{2.59}$$

where γ is the atomic number density (which is the number of atoms present in the simulation cell divided by the simulation cell volume). Pressure is most commonly calculated using the viral equation as shown in equation (2.60) below.

$$P = \gamma k_B T + \frac{1}{V}\left\langle \sum \vec{f}_{ij} \cdot \vec{r}_{ij} \right\rangle \tag{2.60}$$

where $\gamma, k_B, \vec{f}_{ij}$ and $\vec{r}_{ij}$ are the number density, Boltzmann constant, inter molecular force and distance between molecules i and j respectively. The angle brackets denote that this is an ensemble average which is defined as the mean of a quantity of a function within a micro-state of a system. Internal energy is derived as follows.

$$U_{Internal} = U_{Potential} + U_{Kinetic} \tag{2.61}$$

Therefore heat capacities (for constant volume and pressure) for given MD simulations are computed by using the following equations.

$$c_v = \left(\frac{\partial U}{\partial T} \right)_V \tag{2.62}$$

$$c_p = \left(\frac{\partial H}{\partial T} \right)_P \tag{2.63}$$

3. Molecular dynamics simulation of ASW formation

As discussed previously in sections 1.2.4 through to 1.2.8 of chapter one the molecular abundances in molecular clouds are almost entirely driven by surface chemistry on ISM dust grains which is in turn pivotal in star, planet, asteroid and comet formation, laying down the foundations for life to exist in the universe. As outlined in section 1.6 this thesis will focus on studying ASW formation on ISM dust grains using molecular dynamics (section 2.) PVD simulations and not using CVD simulations for the reason outlined in section 1.5.1. Previous simulation studies of amorphous ices have primarily focused on hyper quenched glassy water (HGW)[62], low density amorphous ice (LDA) [63-66], high density amorphous ice (HDA)[63-66], and very high density amorphous ice (VHDA)[63-66]. But MD simulation studies of vapour deposited amorphous ices are sparse in comparison to studies of these metastable bulk amorphous ices.

The first MD simulation of physical vapour deposited (PVD) amorphous ice was carried out by Buch in 1991[67]. In this study 450 water molecules, with initial velocities consistent with 10 K, were randomly deposited every 8-14 ps onto an amorphous ice cluster also at 10 K. However, we know from experimental and observational studies that depositing ASW water molecules generally tend to have a higher temperature than the substrate, both in space and in experiments. This temperature difference is important because it can significantly affect the trajectories of depositing water molecules, as well as previously deposited ones, in several ways. For example, depositing water molecules with higher momenta will generally take a straighter path towards the previously deposited ASW cluster, and *vice-versa*. In general, depositing water molecules will tend to orient themselves, i.e. orient their electric dipoles, such that they are drawn towards any pre-existing ASW cluster. Due to the long-range nature of electric interactions this could happen over quite large distances as shown in Figure 8 below. In this thesis this phenomenon is called “Electro-steering”.

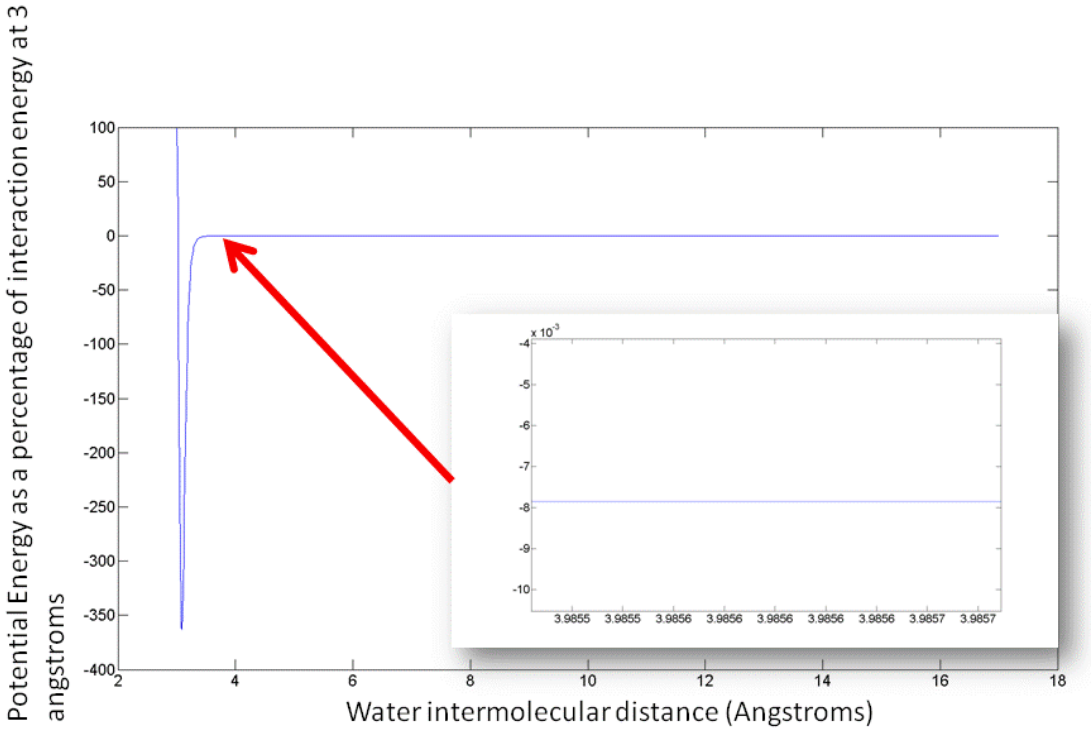

Figure 8: This figure illustrates the total (long and short range) interaction energy between two water molecules at increasing intermolecular distances. The 'y' values are presented as a percentage of the hydrogen bond energy a 3 angstroms. It can be seen here that long range interactions persist even at large distances (0.008%, 1x10-7% at 4 and 10 angstroms respectively).

Moreover, when depositing water molecules impact with any pre-existing ASW cluster their potential and kinetic energy is substantially transferred to the ASW and/or substrate in the local area of the impact. This transfer of energy can enable molecules close to the impact site to reconfigure into more energetically favourable configurations. This effect is called 'impact annealing' in this thesis. Clearly, the higher the temperature and hence energy of depositing water molecules, the more energy should be transferred on impact, and the greater the degree of impact annealing. Returning now to the article by Buch, by initialising depositing water molecules at a very low temperature compared to both space-like and experimental environments, the effects of steering and impact annealing will be over and under-emphasized respectively. In addition, because depositing water molecules in those simulations are

assigned an initial velocity vector directed towards the cluster centre of mass, any potentially important 'shadowing' effects[70], that arise from oblique deposition angles, would also be absent. Bearing these issues in mind, water molecules deposited in these simulations had an average of 3.75 hydrogen bonds per molecule. Incoming water molecules are deposited 10Å above the ice cluster within an 11Å potential cut off radius. As no molecular potential ramp is applied to the cut off radius, there is a discontinuity in molecular force calculations, which might contribute to the overheating reported in this paper.

Wilson et. al.[68] carried out deposition simulations with 2-D boundary conditions where 200 water molecules were deposited on each side of a 77 K amorphous ice substrate every 10 ps. Water molecules were deposited at 77 K and 300 K in random directions, with the z component being directed towards the substrate (on both sides), with an initial random position 8Å above the ASW film. Each deposition event is split into two stages; a constant energy (non-thermostatted) stage is simulated for the first 8 ps followed by a 2 ps cooling phase after the impact has occurred. This deposition strategy allows a simulation performed at a very high effective deposition rate to mimic the much slower deposition rates seen in lab experiments and in space. It was found that ASW porosity increased with decreasing deposition temperature. However, these simulations are relatively small, and initialising depositing molecules only 8Å above the ASW film limits the potential for steering. It is also unclear how electrostatic forces were computed in that work.

In 1995 Essmann and Geiger[69] investigated PVD of amorphous ice on a Lennard Jones (20x20Å) substrate using MD with 2-D periodic boundary conditions, where water molecules were deposited normal to the substrate at random positions in the x-y plane every 4ps. A total of 500 water molecules are deposited above the substrate at an initial distance equal to that of the cutoff radius (8.5Å), and are subject to a 60K Berendsen system thermostat (applied to all molecules except the last 100 deposited) through rescaling molecular velocities. Atoms in the bottom substrate layer are attached to lattice points via harmonic forces allowing small fluctuations about a fixed point in

the simulation cell. A small cutoff radius is applied (8.5Å) to the interaction potentials and long range water-water interactions are included through a reaction field technique[48]. They calculate radial distribution functions, the average density (both including and excluding the pore volume), and pair wise energy distributions. Pores in this context are defined as the microscopic pores or the space between ASW tendril structures. They also investigate substrate topology and ASW density as a function of height above the substrate. It was found that the resulting ASW structures resembled bulk HDA more than LDA, and they claim their results compared well with neutron diffraction experiments[69] in which water molecules were deposited at room temperature, at normal deposition angles, onto a 10K cadmium substrate. However, in these experiments the resulting vapour deposited ice structures are heated up to 100K, prior to neutron scattering, producing an annealed, non-porous and metastable structure, which is not the kind of porous ASW that we are interested in here. Consequently, it is not surprising that neutron scattering results for this annealed vapour deposited ice closely resemble HDA. Moreover, due to the choices made by Essmann and Geiger (low deposition height, initial trajectory normal to the substrate, 60 K thermostat applied to most of system, no quenching stage), their simulations are also likely to lead to annealed ASW as they are unlikely to accurately model the effects of impact annealing, shadowing or steering. Essmann and Geiger performed two further simulations with simulation cell lengths of 17.8 and 35.6Å respectively to investigate finite size effects. They concluded that a simulation cell length greater than 18Å is large enough to eliminate finite size effects. They find, like Buch[67], that the average number of hydrogen bonds per molecule is close to 3.75.

Kimmel et al.[70] performed simple but large-scale vapour deposition simulations, where water molecules were represented as cubes on a cubic lattice. Adopting a “stop and stick” principle it was found that shadowing was very important, i.e. deposition angles affected material density, and large deposition angles (measured from the substrate normal vector) produce a highly mesoporous structure. At deposition angles less than ~40º, where shadowing effects are largely absent, resulting structures are more compact and dense. Simple annealing algorithms (based on hop diffusion) were

employed to model impact annealing. They were found to promote pore collapse and annealing of the ASW film as the number of hops was increased. Although these simulations highlighted possible large-scale features of ASW, the restriction to cubes on a cubic lattice is quite severe. Indeed, by ignoring molecular scale detail and energetics it is possible that the large-scale structure is also inaccurate.

Finally, work carried out by Guillot and Guissani in 2003[71,72] investigated vapour deposited amorphous ice on HGW and cubic ice substrates, where the substrate is placed at the centre of the simulation cell (as was the case with Wilson et. al.) and, using an Ewald summation technique with 3-D periodic boundary conditions, two water molecules are deposited on either side of the substrate every 0.5 ps (1 every 0.25 ps). Water molecules are deposited either normal, or near normal to the substrate (within a deposition cone of 60º), at 3Å above the ASW film, at several temperatures, producing a non-porous ASW film. Three system temperatures (substrate and water molecules) were considered; 50, 100 and 150K, where the substrate temperature is re-set by a single rescaling of system velocities 1000 timesteps (0.5 ps) after each deposition event. They found the amorphous ice density to be independent of deposition temperature. This result contradicts a similar study carried out by Wilson et al. However, their result can be explained by the extremely high deposition rates used and the absence of a quenching stage, which together would result in the ASW film heating up significantly during the simulation. They also find that clusters are able to form above the ASW film prior to deposition. Their use of near-normal initial velocity vectors and an initial position only 3Å above the ASW surface will also reduce the degree of steering and shadowing. Essentially, their ASW films are dominated by impact annealing, resulting in dense ASW structures irrespective of which deposition temperature is considered. Furthermore, as substrate and deposition temperatures are the same for each simulation, i.e. incoming water molecules and substrate temperatures are both 10, 50, 100, and 150K (depending on which deposition temperature is considered), the substrate temperature is not constant throughout this study. Therefore, Guillot and Guissani's conclusion that deposition temperature does not affect ASW morphology must be interpreted with caution, as changes in substrate temperature are likely to play a role in

ASW morphology.

This review of the literature indicates that there are no simulation studies at all that provide reasonably accurate and detailed information about ASW structure, and that there are no attempts to properly simulate the effects of shadowing, steering, and impact annealing in one work. The work of Essman and Geiger is perhaps the most detailed, although as discussed above their simulation strategy is unlikely to be accurate for ASW deposited under astrophysical conditions. On the other hand, the simulation strategy of Wilson et.al. is probably the most accurate, but their simulations are quite small and their results are not described in much detail. Their use of an 8Å deposition height could also be significant because it limits the potential for steering. The aim of this work is to perform more accurate PVD simulations for ASW growth and structure that attempt to properly incorporate the effects of shadowing, steering and impact annealing under conditions relevant to PVD of ASW under astrophysical and experimental laboratory conditions, and to describe the results in more detail. To achieve this, the open source code DL-POLY was modified to model the non-equilibrium process of ASW formation via PVD.

3.1 How DL_POLY was altered for PVD simulation

DL_POLY is an open source MD simulation package written by William Smith and T.R. Forester at Daresbury Laboratory[73]. The DL_POLY software project was funded by the Engineering and Physical Sciences Research Council (EPSRC)[74] in collaboration with Collaborative Computational Project for the Computer Simulation of Condensed Phases (CCP5)[75] and the Molecular Simulation Group (MSG)[76] at Daresbury Laboratory. DL_POLY is designed to perform computer experiments of material equilibrium and static properties, such as density, pressure, temperature, radial distribution functions, as well as material transport properties such as viscosity, elastic modulus, and diffusion coefficients. DL_POLY is written in Fortran 77 and is fully parallelized (MPI), allowing molecular dynamics simulations on high performance computing clusters (HPC) and makes use of precompilers which the user specifies in

order to activate machine specific functionality. DL_POLY can be downloaded from: http://www.cse.scitech.ac.uk/ccg/software/DL_POLY_CLASSIC/index.shtml

The structure of DLPOLY is illustrated below in Figure 9.

As DL_POLY is a generic simulation package for parallelised MD simulations, the user must initialise/set up the simulation accordingly. There are three input text files which allow the user to set up an MD simulation:

- The field file contains short and long range force parameters for all atoms in the simulation. These will, for instance, include the Lennard Jones and Ewald summation parameters for any given simulation.
- The configuration file provides initial Cartesian coordinates of all atoms within the simulation cell.
- The control file contains all the simulation set up parameters, such as total number of time steps, cut off radii, which ensemble should be used, etc.

These three input files are read in to DL_POLY by initialisation of subroutines sysgen.f, sysbook.f, sysinit.f and sysdef.f which in turn dynamically allocate memory and populate data structures. Once these data structures are assigned the array sizes will not change during the simulation. Once the arrays have been populated and the setup has been initialised, the MD simulation begins, passing these data structures to the user specified ensemble. Note that each ensemble has a constant number of atoms (which is why the data structures do not change in size during the simulation). The following ensembles are available in DL_POLY: NVE, NPT, NVT and NST.

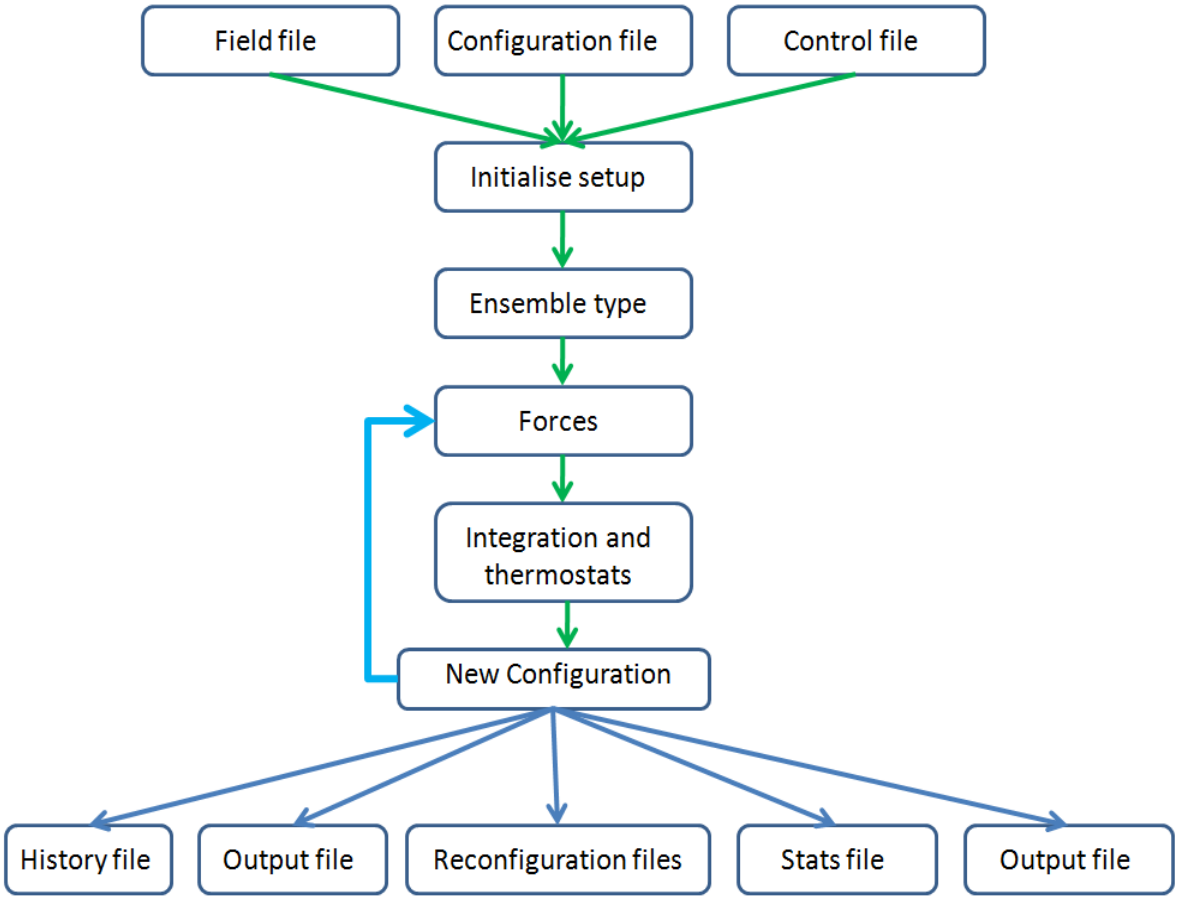

Figure 9: Illustration of the structure of DL_POLY.

The forces.f subroutine deals with all long and short range interatomic forces as well as intramolecular forces. Two subroutines within forces.f called srfce.f and could0.f compute short and long range forces respectively as discussed in the previous chapter. Once forces have been calculated the selected ensemble then performs an integration algorithm (Verlet or Leapfrog as described in section 2.4.1) in conjunction with a thermostat or barostat (Berendsen or Hoover as outlined in sections 2.7.1 and 2.7.2) in order to obtain new atomic velocities and positions which are then fed back into the forces calculation until the simulation is complete. During this iteration process DL_POLY records statistical information in five output files after so many timesteps (this is specified by the user in the Control input file; typically a few hundred or thousand timesteps). The history file contains all the atomic trajectories for the entire simulation, and as such this file can easily be several GB in size even for relatively small simulations. The output file records simulation parameters such as translational

energy, rotational energy, potential energy, temperature, pressure, entropy, enthalpy and radial distribution functions. There are two reconfiguration files “Revive” and “Revcon” which record the simulation parameters and atomic coordinates of the simulation after so many timesteps (once again this is specified by the user in the control input file again typically a few hundred or thousand timesteps). This allows the user to restart the simulation after it has finished if desirable. The stats file records simulation statistical data for calculating time dependent phenomenon such as viscosity and transport coefficients.

3.2 Alterations to DL_POLY to support PVD simulation

In order for DL_POLY to support a PVD simulation where the number of atoms and molecules are increasing as the simulation progress, alterations have to be made to the existing data structures. At the start of this PVD MD simulation the DL_POLY arrays and data structures have to be allocated statically so that they are large enough for the final system size. Also, these static arrays have to be populated with the correct initial deposition values so that they can be introduced into the simulation. These include Cartesian coordinates, molecular centre of mass coordinates, molecular translational and rotational velocities and accelerations. After each deposition event the number of molecules in the system is incremented by one and another molecule is deposited. Each new molecule that is introduced to the system has molecular velocities assigned consistent with a desired temperature using a Maxwell-Boltzmann distribution (where the z-velocity component is directed towards the substrate). This introduction and deposition algorithm is discussed in more detail in later sections of this chapter.

3.2.1 Forces

It is important to stress that DL_POLY does not compute pair-separations on a molecular basis even for rigid bodies. Instead, pair separations are computed on an atomic basis. For bulk simulations this is not a problem as long as an Ewald Summation technique is used. However, the simulations performed in this thesis are very long, and an Ewald summation technique is not practicable. Instead a cutoff is used. However, specifying a cutoff radius in DL_POLY intrinsically leads to problems due its use of

atomic-based, rather than molecular-based, pair separations. This means, for example, that if two molecules are 10 Angstroms apart, and the cut off radius is 8 Angstroms, not all the pair-interactions for the pair of molecules will be calculated. This is illustrated in Figure 10 below.

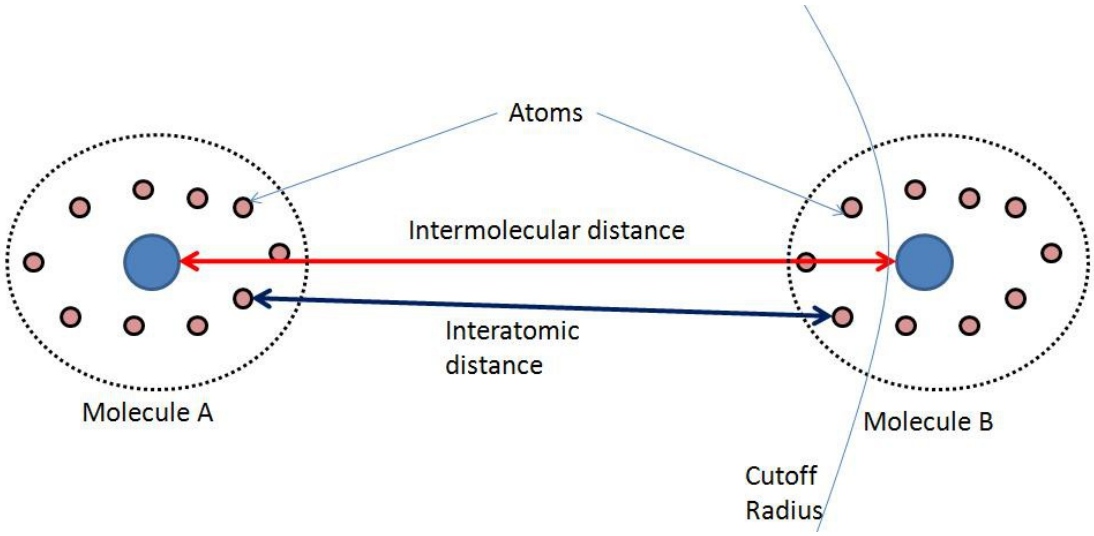

Figure 10: DL_POLY uses only an atomic-based cutoff radius. Therefore if we are computing the forces between two molecules A and B respectively, if the intermolecular separation is 10 angstroms and the atomic cutoff radius is 8 angstroms only some atom pairs will be included in the forces calculation. This leads to non-neutral charge sums in the calculation of electrostatic interactions, and un-physical results.

Consequently, when calculating the force between a pair of molecules some atom pairs within a molecule will be within the specified cutoff radius whilst others are not, resulting in unrealistic physical behaviour. For example, when one tries to perform PVD simulations with this kind of setup, incoming molecules experience a stepwise impulse force as a depositing water molecule approaches the ASW and/or the substrate. Therefore, it was necessary to modify DL_POLY in order to accurately simulate PVD without an Ewald sum. It was also necessary to modify DL_POLY to take account of the increasing number of molecules in the system as the simulation progresses.

The former issue is solved by creating a new molecular index in forces.f ensuring that DL_POLY uses molecule-based separation calculations. That is, all atomic pair-interactions between two molecules are calculated if the molecular centre-of-masses are within the cutoff distance (interactions between atoms within the same molecule are

ignored). Code has been modified in the srfce.f and could0.f subroutines in order to ensure a molecular-based cutoff is incorporated with this new molecular indexing. However, as mentioned in the previous chapter, forces are the first order derivative of the potential energy. Consequently, applying a cutoff to molecular-based separations will produce a stepwise molecular interaction at the cut off radius. This is problematic as un-physical phenomena can be introduced into the simulation. In order to overcome this, a ramp-function is incorporated at the cutoff radius. This allows molecules to reorient smoothly as they approach the cutoff separation by gently introducing molecular forces. This ramp function is applied to both Lennard Jones and electrostatic forces in the srfce.f and coul0.f respectively.

3.2.2 Thermostats

DL_POLY can use both the Nose – Hoover and Berendsen thermostats. Both of these thermostats rescale molecular velocities (translational and rotational) to a desired temperature as set by the user. For normal MD simulation this thermostat would be applied to every molecule in the system so that all molecule are rescaled to the same desired temperature. However, for a non-equilibrium MD simulation such as a MD PVD we require multiple thermostats

- One for the ISM dust grain surface
- Another to hyperquench the ASW

This is described in detail in the 3.5 and 3.6 sections.

3.2.3 VMD

DL_POLY does have a simple light weight visualisation tool for displaying molecular configurations before and after simulation runs but does not monitor how the simulation is progressing. Alterations were made to DL_POLY so that Visual Molecular Dynamics (VMD) XYZ files are written out for visual inspection. VMD is an open source, script based visualisation package based on VRML, it contains a number of rending tools such as POV-Ray, Renderman and Tachyon which can be used to generate MD simulation

movies in mpeg3 format.

3.3 Water models

Water is the most fundamental molecule for supporting life, and consequently there has been a lot of interest in developing water models which accurately reproduce the characteristic properties of water such as the density anomaly. There are over 25 water models with each model tailored for a specific region of the water phase diagram. For example TIP4P/2005[77] and TIP5P[78] accurately reproduce the temperature of maximum density at 5 and 4 °C respectively (3.984 °C experimentally[79]). However, these models do not accurately reproduce water's dielectric constant (60 and 81.5 respectively[77,78], in comparison to the experimentally obtained value of 78.4 at 298K). The SPC/Fw[80] and TIP4P/FQ[81] models, however, reproduce this value more accurately at 79.6 and 79 respectively. In addition to this the aforementioned models all fail to accurately reproduce the dipole moment of water (the TIP4P/2005, TIP5P, SPC/Fw and TIP4P/FQ model dipole moments for liquid water at room temperature are 2.305, 2.29, 2.39 and 2.64 debye respectively (2.95 debye experimentally) whereas the GCMP[82] model is closer 2.723. TIP4P/2005 is the best model for reproducing the expansion coefficient (2.8 10^{-4} $°C^{-1}$ compared to 2.53 10^{-4} $°C^{-1}$ experimentally), whereas the previously mentioned models are noticeably inaccurate (TIP5P, SPC/Fw, and TIP4P/Ew model expansion coefficients of 6.3, 4.98 and 3.1[83] respectively).

Overall, the TIP4P/2005 model most accurately reproduces the phase diagram of water ice and solid phases when compared with other water models[78], and it accurately reproduces the temperature of maximum density and the expansion coefficient. TIP5P more accurately models the dielectric constant and the temperature of maximum density but is mainly use for condensed phases and is more computationally expensive than TIP4P/2005. With the exception of the temperature of maximum density, the TIP5P model does not offer a greater degree of accuracy when compared to four site models (TIP4P). Therefore the additional computational cost for using such a model is not justified. Recent work[78] has shown that the SWM4-NDP model can be more accurate than TIP4P models across several characteristics such as the dipole moment, dielectric

constant, self-diffusion and average configuration energy. However, the computational cost involved in using such a model in a PVD MD simulation is prohibitively expensive due to the presence of a drude oscillator (see section 2.6). Furthermore, as water is being cooled to 10K in the PVD MD simulations in order to simulate ISM conditions, such accuracy is not needed as water will form a tetrahedral hydrogen bonding network. Because we expect to form an amorphous solid ASW cluster, we expect any relatively simple water model able to reproduce bulk water ice and fluid phase equilibrium with reasonable accuracy should be sufficient. Hence, the TIP4P/2005 water model is selected.

3.4 Quantum Effects

Previous theoretical studies (MacRury and Steele) have found that quantum effects are observed for rotational modes of motion for water at 300K, as water is simulated at very low temperatures (10K) in this thesis it is anticipated that this rotation quantum effect will increase therefore quantum effects must be considered see section 2. As the average separation distance between hydrogen-bonded water molecules is 2.9 angstroms the simulations are well within the classical limit as the de Broglie wavelength for water at 10K is 1.3 angstroms as shown in Table 4. However, for the hydrogen atoms in water the de Broglie thermal wavelength, using equation (2.1), is approximately 4.2 times larger. But this estimate of the positional uncertainty of hydrogen atoms does not take into account their covalent bonding to the oxygen atom which severely constrains them. Physically, it is unreasonable for the hydrogen atoms to have greater positional uncertainty than a water molecule as a whole, and so it is concluded that quantum effects are largely absent. It is possible that quantum effects may weaken hydrogen bonds via quantum tunnelling therefore creating 'softer' more weakly bound hydrogen bonds. However, hydrogen bonds at 10K are very strong bonds and in light of this it is not anticipated that quantum effects will significantly change the ASW structure. Furthermore, there no classical MD models for modelling water at 10K and sufficiently capturing quantum behaviour, Car–Parrinello (Ab intio) molecular dynamics could be used to simulation these quantum effects but these simulations are too computationally expensive for this study. Therefore this thesis is going to use the

TIP4P/2005 water model for PVD MD simulations, as it offers a good compromise between accuracy and computational cost.

3.5 Deposition algorithm

DL_POLY, an open source MD simulation package, has been adapted to simulate PVD, where water molecules are randomly deposited onto a cold substrate. We define a simulation cell with 2D periodic boundary conditions in the x and y directions parallel to the substrate. We adopt a deposition strategy similar to that of Wilson et.al. for each deposition event. That is, we split each deposition event into two distinct stages; a deposition/annealing stage and a hyperquenching stage which are described in detail later (section 3.6). This strategy ensures that impact annealing is simulated accurately and that the substrate is at the correct temperature before deposition of each molecule, thereby mimicking a much slower deposition rate. The substrate is maintained at a temperature which is much lower than that of depositing water molecules initially, ensuring that simulations mimic conditions both in laboratory experiments and in space as described previously in section 1.2.2; this is discussed in detail later in section 3.6. We expect the substrate composition might affect ASW structure, and so have chosen to perform simulations on two kinds of substrate that are representative of a wide range of substrate types; a Lennard-Jones substrate as described in Essmann and Geiger[69] representative of hydrophobic dust grain surfaces such as graphite, and a cubic water ice substrate representative of hydrophilic dust grain surfaces such as silica (section 3.7). To investigate how deposition temperatures affect ASW morphology, three deposition temperatures are considered; 50 K, 150 K and 300 K. Note, the deposited water molecules have initial velocities consistent with these temperatures via a Maxwell-Boltzmann distribution. The substrate temperature is always maintained at 10 K. A leap frog integration algorithm (as outlined in section 2.4.1) used to calculate new molecular velocities and positions. Structural order parameters are introduced to describe the evolution of ASW structure with height above the substrate, and are described in the results chapter.

3.6 Deposition/annealing and hyperquenching strategy

Deposited water molecules are initially assigned random coordinates in an x-y plane at a distance equal to the cutoff radius (1.4 nm) above the top-most water molecule in the ASW film (or the substrate for the first deposited molecule), which should allow reasonably accurate modelling of molecular steering. All depositing water molecules have the same initial orientation, this is was done for simplicity and will not bias the deposition results as incoming trajectories are of different lengths and angles with different initial rotational velocities. They are initiated with a random velocity consistent with 300 K, 150 K or 50 K using a Maxwell-Boltzmann velocity distribution, depending on which deposition temperature is considered. A Maxwell-Boltzmann distribution was chosen as it is a high temperature approximation to either a Fermi-Dirac and Bose-Einstein distributions which are quantum distributions. Of course, the z-component of the initial velocity is always towards the substrate. Velocity density of states are derived from statistical mechanics and assumes that particles move freely (not subject to bond interaction energies) between short range interactions and that the system is in thermodynamic equilibrium. The probability of a molecule having a particular velocity is dependent on its mass and temperature. The velocity density of states for each depositing water molecule are unique for each deposition temperature as shown in equations (3.1) and (3.2) below representing translational and rotational density of states respectively.

$$P_i = \sqrt{\left(\frac{m}{2\pi\ k_b T}\right)} \exp\left(\frac{-m\,\dot{\vec{r}}_i^{\,2}}{2\mathrm{KT}}\right) \tag{3.1}$$

$$P_i = \sqrt{\left(\frac{I_i}{2\pi\ k_b T}\right)} \exp\left(\frac{-I\,\omega_i^2}{2\mathrm{KT}}\right) \tag{3.2}$$

where P_i, m, k_b, T, r_i ω and I_i represent the velocity density of states, molecular mass, Boltzmann's constant, desired deposition temperature, initial random translational velocity, initial random rotational velocity and molecular inertia respectively. The

subscript *i* indicates that this process is repeated for each x, y and z component of velocity (both translational and rotational). By computing the inverse of the integral of this velocity distribution, random translational and rotational velocity vector components consistent with a desired temperature can be calculated from uniformly generated random numbers on the interval [0,1]. Equations (3.1) and (3.2) above produce the same angular distribution for all deposition temperatures as only the initial trajectory vector magnitude changes with increasing deposition temperature. Below shows that most of the deposition angles are at 70 – 80 degrees of the substrate normal vector.

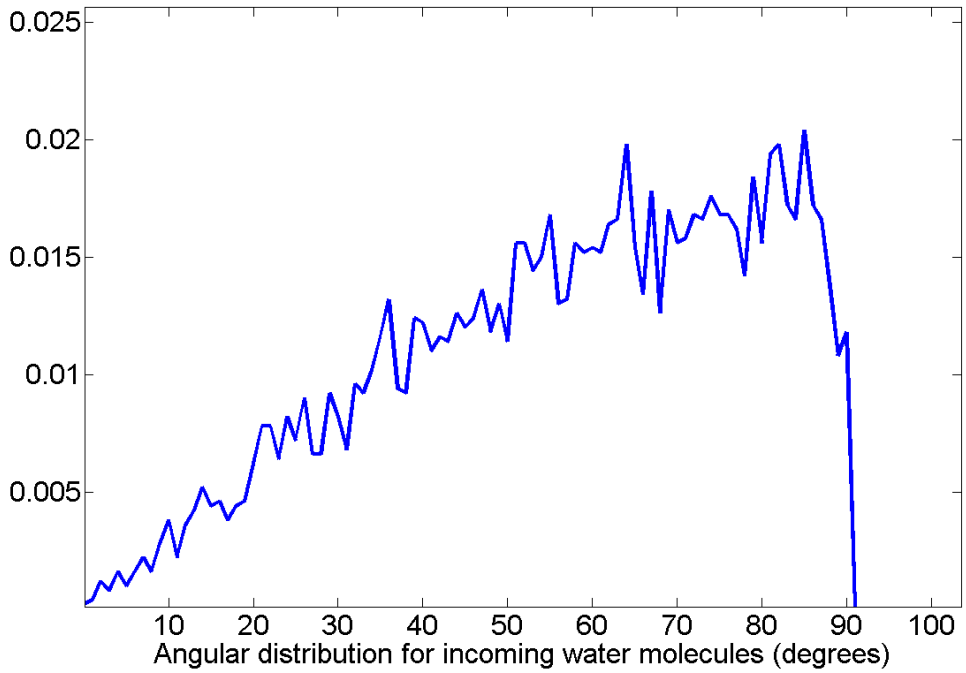

Figure 11: Shows the angular distribution of incoming water molecules with respect to the substrate normal. It can be seen that most incoming molecules are being deposited 70 - 80 degrees from the substrate normal.

Once the initial state is chosen for a depositing water molecule the simulation proceeds, based on 0.1 fs intervals, until the depositing water molecule physisorbs to the surface. A physisorption event is registered when the depositing water molecule's z-component of momentum changes sign, indicating a collision. After this deposition stage a further 4000 time steps (0.4 ps) are assigned for the annealing stage. Because depositing water

molecules are hotter than the substrate and ASW, and because of the thermal energy released when several hydrogen bonds are formed during physisorption, a thermal gradient is generated between the region where a water molecule impacts (the impact zone) and the substrate. As a result, a thermal wave propagates via conduction down through the ASW towards the substrate, exciting water molecules trapped in metastable configurations, and potentially enabling molecules near the impact zone to reconfigure into more energetically favourable structures; this is known as impact annealing. We assume that heat transfer through radiation is insignificant, and that all thermal energy from impacting water molecules, is transferred down through the ASW film by thermal conductivity. This assumption is supported by experimental observations[21,29,30] which indicate that if deposition rates are increased, the vapour deposited ice film melts as the cryostat cannot extract heat from impacting water molecules quickly enough. Therefore, the vast proportion of impacting thermal energy is dissipated by thermal conductivity and not radiation.

To accurately model impact annealing, neither ASW water molecules nor the deposited molecule are subject to a thermostat during the deposition/annealing stage, because this could interfere with the impact annealing process. Instead, a thermostat is applied to cool only the substrate during the deposition and annealing stages.

	Deposition rates
Observational	6.9444×10^{-7} molecules hour^{-1} nanometer^{-2}
Experimental	2×10^{5} molecules hour^{-1} nanometer^{-2}
Simulation	4×10^{14} molecules hour^{-1} nanometer^{-2}

Table 5: showing deposition rates

Table 5 shows typical PVD deposition rates for experimental and observational studies, and simulations performed for this study. Given that our deposition rates are vastly higher than those experienced in the ISM, we apply 'aggressive' thermostating this effectively simulates an infinitely slow deposition rate as molecules are being hyperquenched instead of being allowed to cool down over a longer period of time. As discussed previously (see section 3.2.2) a substrate thermostat is used to maintain a

substrate temperature of 10K at all times during the MD PVD simulation. Initially, it was thought that applying an aggressive substrate thermostat, where substrate molecular velocities would be rescaled at every simulation time step (0.1fs) would be adequate to cool the ASW structure back down to 10K through molecular thermal conduction after each deposition. However, it was found that even with an aggressive substrate thermostat thermal energy was not extracted from the ASW structure quickly enough. This is because the substrate's ability to remove thermal energy from the ASW structure depends on thermal contact as well as conduction. Therefore, short range substrate interactions do not provide adequate thermal contact with the ASW structure and as a result the simulation time required for the ASW structure to reach 10K after each deposition event (the condition required for depositing another water molecule), would be prohibitively long. To overcome this problem water molecular velocities are abruptly rescaled (hyperquenched) to 10K after the annealing phase for 1000 timesteps (0.1ps) to allow the system to equilibrate at this temperature. During this final 'hyperquenching' equilibration stage a Berendsen thermostat acting on the whole system is applied every time step. This hyperquenching phase is over 1000 time steps as water ASW molecules need to reconfigure into the most energetically favourable position to ensure the ASW structure is stablised before another water molecule is added. If the hyperquenching phase were only over one time step the ASW structure would simply convert potential energy into thermal energy and increase the ASW temperature. Another water molecule is deposited after this equilibration phase when the overall ASW temperature is 11K. If any water molecule moves beyond 30 angstroms above the top of the ASW film (perhaps by bouncing off the ASW film or substrate) then it is deleted from the simulation. The simulation cell x-y area is kept constant throughout the simulation and 500 water molecules are deposited on to each substrate.

3.7 Water and substrate models

The tip4p/2005 water model is a four site model consisting of three partial charge sites and a Lennard-Jones site. The Lennard-Jones site models core repulsion and attractive dispersion interactions between two water molecules. Two partial charge sites are placed where hydrogen atoms are located, and a third charge site, commonly referred to

as a 'q-site', is placed slightly off-centre from the Lennard-Jones site to account for the particular electrostatic properties of water molecules (i.e. the dipole moment and hydrogen bonding). The tip4p/2005 model is shown below in Figure 12

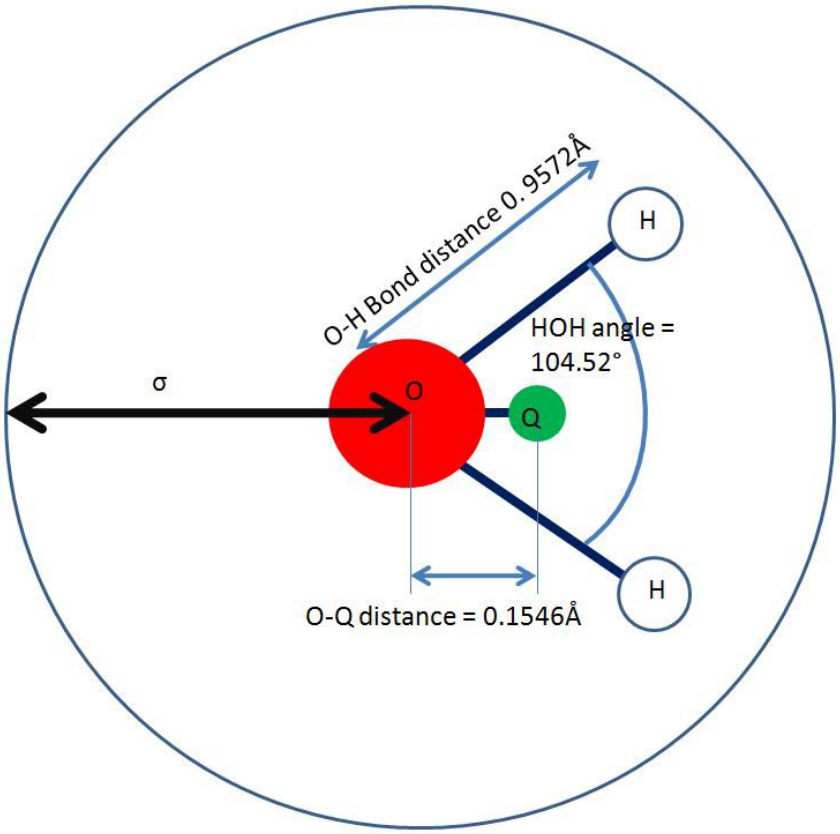

Figure 12: illustrates the tip4p/2005 water model. Hydrogen and oxygen atoms are shown in white and red respectively, while the q-site is shown in green.

Forces are calculated between appropriate pairs of sites on a pair of molecules, where the resultant molecular force, acting through each centre-of-mass, is the sum of all site-site forces between a pair of molecules. Electrostatic interactions in simulations of water are often treated by employing an Ewald summation technique[60], or similar method, to take account of interactions at long range. However, this technique is rather expensive and typically results in reducing computational efficiency[61] by about an

order of magnitude. A single MD PVD simulation takes around 2 months, which is quite demanding already for a typical desktop workstation, using an Ewald summation each simulation would take around 2 years which is unacceptable or this study. Hence, to improve computational efficiency a cutoff radius and ramp function is applied as discussed previously in section 2.3. A ramp function is used to overcome the overheating problems reported in previous simulation studies[68,71,72]. This ramp function is only applied to the electrostatic (long range 2.6) part of the interaction potential as the discontinuity produced by the (short range 2.1) Lennard – Jones is insignificant as shown in the Figure 14 below where the interaction energy at 14 angstroms is only 0.03% of the interaction energy at 3 angstroms.

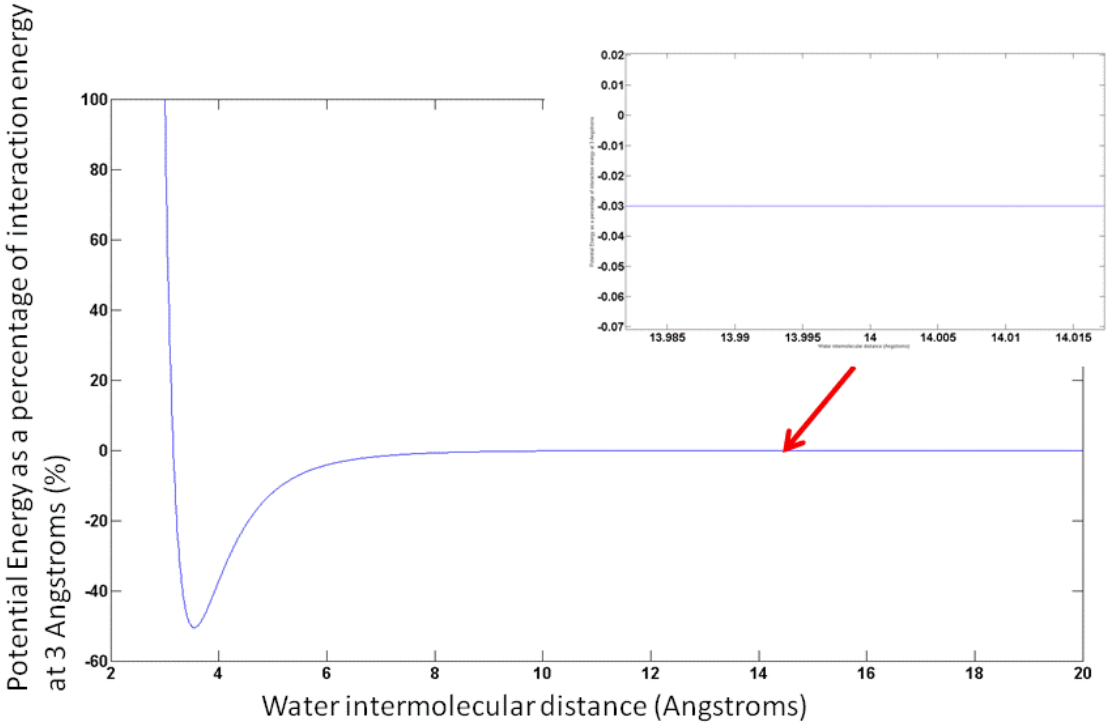

Figure 13: This figure illustrates the short range interaction energy between two water molecules at increasing intermolecular distances. The 'y' values are presented as a percentage of the strong interaction energy a 3 angstroms. It can be seen here that Lennard-Jones interactions at 14 are only 0.03% of the interaction strength at 3 angstroms.

The ramp function applies to the whole molecule for electrostatic forces only and the cutoff radius is measured from oxygen atoms within each water molecular pair. Equation (3.3) below shows the ramped water inter-molecular force. The ramp function

is only applied to forces and not to pairwise energies. This does mean that there is an inconsistency between forces and energy at the cutoff radius but seen as the potential energy at 14 angstroms is so low (as shown in Figure 13) this inconsistency is insignificant.

$$\vec{F}_{lm} = \frac{24\epsilon}{\left|r_{lm}^{2}\right|}\left[2\left(\frac{\sigma}{r_{lm}}\right)^{12} - \left(\frac{\sigma}{r_{lm}}\right)^{6}\right]\vec{r}_{lm} + \sum_{ij=1}^{3}\frac{q_i q_j}{4\pi\epsilon_o r_{ij}^{3}}\vec{r}_{ij} f(\vec{r}_{lm}) \tag{3.3}$$

where

$$f(r_{lm}) = \frac{\left[\cos\left((r_{lm} - (r_{cut} - 1\text{A}))\pi/1\text{Å}\right) + 1\right]}{2} \tag{3.4}$$

for $(r_{cut} - 1\text{Å}) < r < r_{cut}$ and

$$f(r_{lm}) = 1 \tag{3.5}$$

for $r < (r_{cut} - 1\text{Å})$

where l and m are the molecular indices, i and j are the atomic indices on molecules l and m respectively, and r_{cut} is the cut-off radius. F_{ij}, r_{ij}, r_{lm}, ε_o, $\boldsymbol{\varepsilon}$, q and σ are the force between two molecules, the separation between the centres of molecules l and m, the separation between sites i and j, the permittivity of free space, the Lennard-Jones energy coefficient, the atomic charge of the charge site, and the Lennard-Jones length coefficient respectively 1A is one Angstrom. The molecular torques are calculated using equation (2.29) to (2.51). The corresponding intermolecular energy, U_{lm}, is taken to be as shown in (3.6) below.

$$U_{lm} = 4\epsilon\left[\left(\frac{\sigma}{r_{lm}}\right)^{12} - \left(\frac{\sigma}{r_{lm}}\right)^{6}\right] + \sum_{ij=1}^{3}\frac{q_i q_j}{4\pi\epsilon_o r_{ij}} f(r_{lm}) \tag{3.6}$$

Equations (3.5) and (3.6) are not quite consistent over the range of the ramp function, due to a missing term, $f'(r_{ij})$, in equation (3.5). However, we find that including this term in the inter-molecular force once again results in unphysical behaviour, and so prefer to use the equations as given above. This problem is typical when using a cut-off with electrostatic interactions. In order to overcome this an Ewald summation would have to be employed but as described in section 3.7 using this method imposes a massive computational cost, which is unacceptable for this work. However, we can justify using the equations above because at the temperatures considered here short range forces and in particular hydrogen bonding are dominant. Centre-of-mass accelerations are obtained by Newtonian law, where the resulting molecular force vector acting on molecular mass centres is divided by the molecular mass (18AU for water). Velocities and positions are calculated using a leap frog algorithm (section 2.4.1), using a Berendsen thermostat as described in sections 2.7.1 and 3.6 using equations (2.52) and (2.53). Orientational dynamics are computed using Hamilton's quaternions as described in section2.5.2. A Berendsen thermostat is also applied to angular velocities using Equations (2.52) and (2.53).

Two substrates are considered; a (hydrophobic) Lennard-Jones substrate and a cubic ice (hydrophilic) substrate, measuring 30 angstroms in the x and y directions. These two substrates were chosen as they represent ISM dust grains (1.2.4). Dust grain surfaces are Silica or graphitic in nature therefore are hydrophilic and hydrophobic respectively. Analysing how the ASW structure is affected by either a silica or graphite dust grain morphology is important for the protoplanetary disk phase (1.2.8) and subsequently for planet, asteroid and comet formation. Furthermore, analysing how deposition temperature affects ASW structure will shed light on how significant ISM gas phase temperatures are on ASW icy mantle morphology and the role that plays on the prestellar cores (1.2.6), protostellar cores (1.2.7) and protoplanetary disk (1.2.8) phases of stellar evolution.

3.7.1 Hydrophobic Substrate

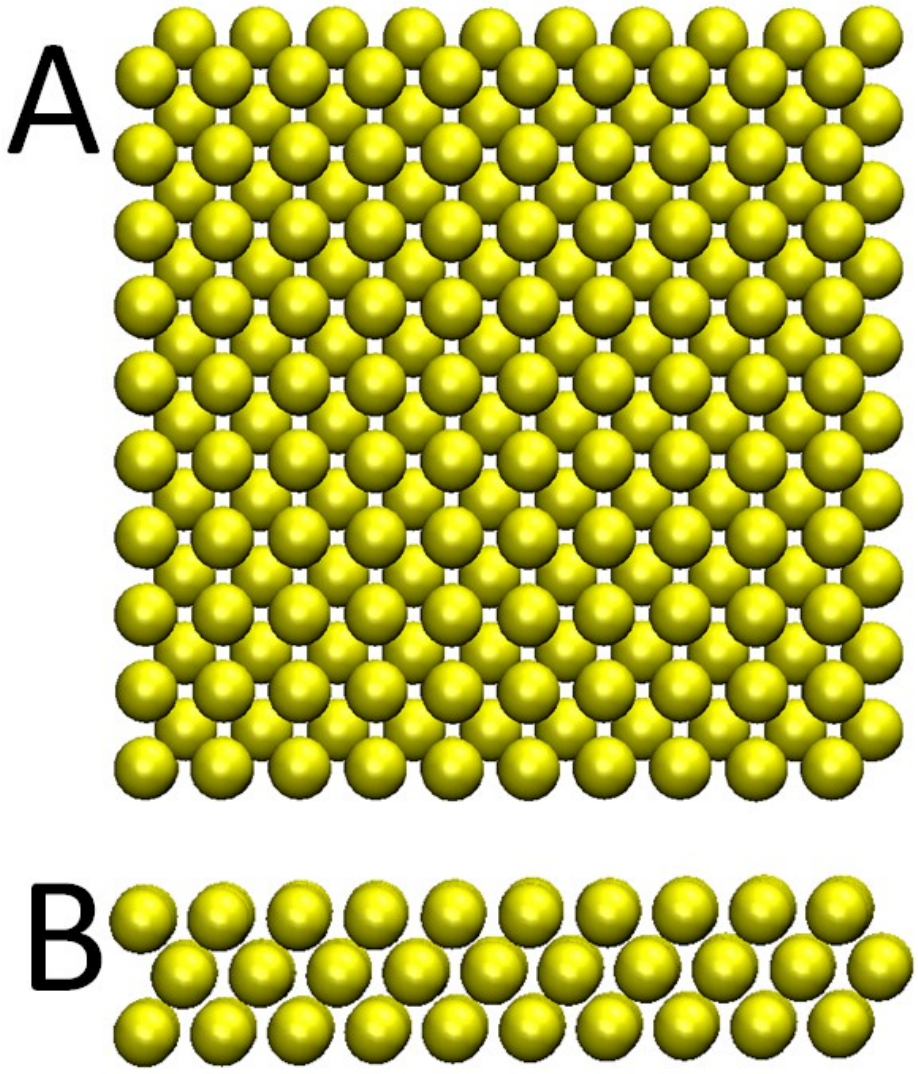

Figure 14: Illustrates the cross sectional view of the hydrophobic substrate. Figures A and B represent the X - Y and Z -X views respectively.

The Lennard-Jones substrate consists of 300 Lennard-Jones (LJ) particles arranged in a body-centered-cubic (bcc) structure forming three layers with 100 LJ particles each. Lennard Jones particles are chosen to represent a hydrophobic substrate as these particles do not have any partial charge sites. This accurately models a hydrophobic substrate as water – water interactions will be much stronger than water substrate interactions meaning that surface tension will be much greater than surface diffusion.

The substrate is held at a fixed space in the simulation by summing up all the substrate atoms z velocity components and applying a counteracting z velocity component to every substrate atom. This ensures that the substrate z position does not drift as the simulation progresses. Due to the simplicity of this substrate the interaction potential energy and interaction forces can be tabulated in a one dimensional array in memory. As calculating the LJ interaction for each substrate LJ atom is more expensive than looking it up in memory, this further increasing computational efficiency.

3.7.2 Hydrophilic Substrate

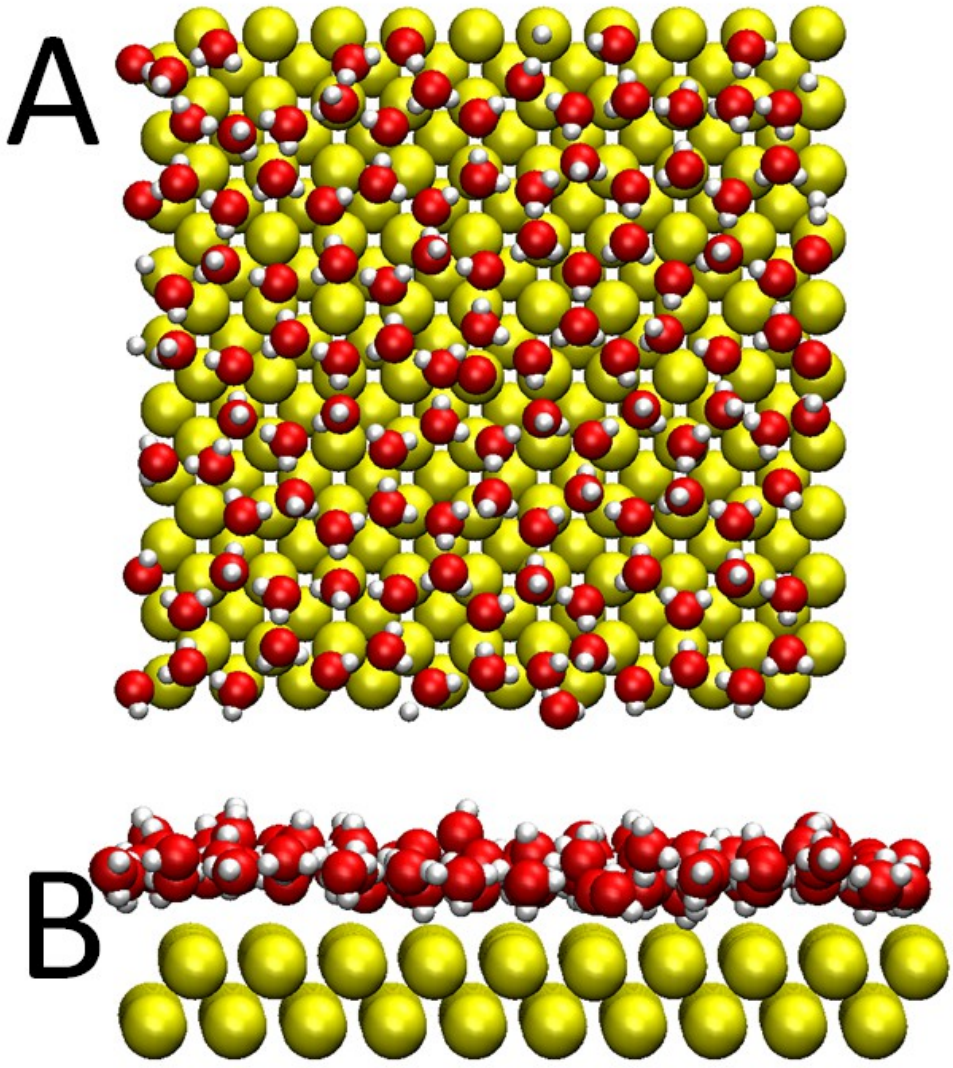

Figure 15: illustrates the cross sectional view of the hydrophilic substrate. Where A and B represent the X - Y and Z -X view respectively.

The cubic ice substrate consists of 2 LJ layers with 100 LJ particles in each layer arranged in a bcc configuration with 118 water molecules placed above these LJ layers. Water molecules in the top layer of the substrate are arranged in a cubic ice monolayer configuration where each water molecule is attached to lattice points via harmonic forces. This kind of substrate model was chosen because it was found in previous simulations that an isolated layer of cubic ice is not stable, due to the fact that the stability of the cubic ice structure is dependent on the interactions between layers. Previous simulations found that at least 4 bilayers were required to stabilise the cubic ice structure. However, introducing 4 layers of water to the substrate was considered too computationally expensive. Instead, harmonic forces, which in computational terms scale linearly with system size, were introduced to stabilise the water layer.

Translational springs were attached to hydrogen and oxygen atoms in order to constrain translational and rotational motion and are shown in equation below.

$$F_i = k(\vec{r}_0 - \vec{r}_i) \tag{3.7}$$

where F_i, k, r_0 and r_i are the atomic force, spring stiffness constant, initial cartesian coordinates and deviated coordinates for atomic species i respectively. A spring stiffness of 10,000N/Å was used for this simulation. In order for adsorption to occur these water molecules in the cubic ice bilayer must be able to redistribute impact energy, or incoming water molecules will simply rebound off the substrate immediately after impact. It was found in previous simulations that applying only harmonic forces attached to lattice points provided no energy dissipation mechanism and in order for adsorption to occur, some interaction potential between substrate atoms was required. Therefore, water Lennard-Jones sites in this cubic ice substrate are able to interact with each other, and all LJ substrate atoms beneath them. This allows energy dispersal through LJ interactions, as described previously (3.6) This dissipated thermal energy is then removed from the simulation by a thermostat. Electrostatic forces are neglected for molecules within the cubic ice bilayer to increase computational efficiency. However, electrostatic forces are calculated for incoming water molecules when they interact with water molecules within the cubic ice substrate.

All substrate, ASW film and depositing water molecules interact (within the cut-off range), and water- LJ substrate interactions are described using Lorentz-Bethelot rules as shown in (3.8)and (3.9) below.

$$\sigma_{LJ-water} = \left(\frac{\sigma_{LJ} + \sigma_{water}}{2} \right) \tag{3.8}$$

$$\epsilon_{LJ-water} = \sqrt{(\epsilon_{LJ}\epsilon_{water})} \tag{3.9}$$

where ε_{LJ} and σ_{LJ} are the Lennard-Jones substrate energy and length parameter respectively. Tables 2 and 3 give the interaction coefficients and partial charge parameters for all interactions. The substrate values were taken from Essman and geiger[69] and water values were taken from the tip4p/2005 model of Abascal et.al.[77].

Interactions	Energy (kJ/Mol)	Length (Angstroms)
Substrate – Substrate	5.7631	2.8
Substrate - Water	2.1133	2.979
water -water	0.7749	3.1589

Table 6: Shows the Lennard - Jones interaction parameters for water and substrate pairs.

Sites	Charge (Electron unit charge)
H1	0.5564
H2	0.5564
O	0
Q	-1.1128

Table 7: Shows the charge sites parameters for water interaction energies.

3.8 Electro-steering algorithm

As mentioned in the first two chapters, ASW morphology is fundamentally dependent

on deposition kinetics. The deposition simulations described in the previous section allow one to investigate ASW structural properties but not the underlying deposition kinetics of ASW formation. It is interesting to note that a previous experimental study of ASW formation[40] has shown that deposited water molecules tend to aggregate when deposited onto cold substrates, producing hemispherical clusters and subsequent island growth. Given the very low substrate temperatures used in this experimental study (10 K) it is thought unlikely that these clusters form via diffusion of water molecules across the surface. Instead, they are thought to form by a steering process, whereby incoming water molecules are directed towards existing surface clusters. This 'steering' effect is very likely generated by the electrostatic dipole moment of water. This behaviour is analogous to randomly depositing small magnets onto a magnetic cluster located on a surface. Irrespective of the initial trajectory, a depositing magnet will orient itself into the most energetically favourable orientation with respect to the magnetic cluster and be attracted towards that cluster. Similarly, water molecules deposited onto a cold surface will re-orient into the most energetically favourable orientation and be “steered” towards deposited water molecules. We call this process 'Electro-Steering'.

Donev et al.[40] carried out stick-and-stop PVD simulations of water molecules represented as cubes on a lattice. Although electro-steering is not present in these simulations another interesting concept is reported. Water cubes with shallow trajectories, that is trajectories near parallel to the substrate plane, adsorb laterally onto water clusters. This process of water molecules adsorbing onto the sides of water clusters is known as “shadowing” as water clusters effectively prohibit other potential adsorption sites.

We suggest that electro-steering could be responsible for the initial formation of water clusters on cold substrates, and that a combination of electro-steering and shadowing is responsible for the subsequent growth of these ASW surface clusters. Electro-Steering has not been investigated before (to my knowledge). Measuring the degree of electro-steering is not straightforward, as it requires one to quantify the deviation of depositing

water molecule trajectories. We devised the simulation procedure outlined below to measure this deviation.

100 water molecules are deposited onto both hydrophobic and hydrophilic substrates to form an initial cluster on the substrate as described in the deposition simulations above. Then, each subsequent water molecule is assigned random coordinates in the x-y plane, 1.4 nm above the top most water molecule in the initial ASW water cluster. Water molecules are initiated with random velocities corresponding to a Maxwell-Boltzmann velocity distribution of 50K, 150K and 300K, with the z velocity component always pointing towards the substrate, as described in the deposition section above. A physisorption event is registered when the velocity of an incoming water molecule goes from negative to positive, signifying a collision has occurred with either the water cluster or substrate. After this collision is detected a further 4000 time steps (0.4ps) is allocated for hyperquenching the water cluster down to a temperature of 10K, this is achieved by rescaling the velocity vectors for each time step for this 4000 timestep hyperquenching phase. Once this hyperquenching phase is complete the 'landing coordinates' are recorded and the adsorbed water molecule is deleted from the simulation, after which another depositing water molecule is created and deposited using the same algorithm and the same initial cluster. In total 1000 water molecules are deposited onto both substrates for each deposition temperature (50K, 150K, 300K).

The electro-steering simulations described above investigate 1000 independent deposition trajectories. To quantify how deposition temperature effects steering we divide the simulation cell x-y plane into a grid. As there are 1000 water molecules deposited there will be 1000 grid-square hits. Therefore, it is possible to calculate the probability that a water molecule will deposit onto a certain area of the substrate as a function of deposition temperature. We perform further simulations to act as a 'control' so that the effect of steering can be clearly seen. In these control simulations the intermolecular forces are turned off, and a deposition event is recorded when a depositing water molecule comes within 3 angstroms of an ASW molecule. We call these 'ballistic' simulations. As with the electro-steering simulations 1000 water

molecules are deposited, allowing one to compare ballistic trajectories against electro-steering influenced trajectories.

Such a small cluster is unlikely to capture shadowing effects at all. Therefore, these simulations investigate steering in isolation, effectively ignoring the role shadowing plays in ASW formation. To investigate shadowing a larger deposited water cluster is required. Consequently, a second batch of electro-steering simulations is performed. These simulations follow the same process as described above for the 100 water molecule ASW cluster except that a 450 water molecule cluster is used. In addition, ballistic trajectory simulation are performed on this larger water cluster, thus investigating shadowing for this larger cluster in isolation. Comparing the result obtained from both electro-steering and ballistic trajectories, for both the small and large clusters, one should be able to ascertain which phenomenon is more significant (steering or shadowing).

4. Measurements and Results

4.1 Measurements

A set of measurements have been developed to provide a detailed analysis of the ASW structures grown by PVD simulations. They allow comparison of ASW physical properties to those of other ices. To make these measurements we simulate the final ASW structures formed at a constant temperature of 10K for a further 100,000 time steps, with samples taken every 100 time steps. We divide the simulation cell into a series of 'bins'. Each bin is a horizontal 'slab' of the simulation cell volume measuring 30x30x3Å. A total of 180 bins are used, each successive bin placed 0.5Å vertically above the previous bin. So, in total the bins cover a height of 92.5Å. 3Å slabs are used to reduce statistical noise below an acceptable level. The bins are used to measure the variation with height above the substrate of the ASW mass density and the number of hydrogen bonds per water molecule. We also measure interaction energy – radial distance distributions (which are referred to as GE plots from now on), as described next.

Clearly, hydrogen bonding plays a crucial role in water ice structure, but the definition of what constitutes a hydrogen bond is not so clear. Work by Swiatla-Wojcik[84] defines a hydrogen bond using both a geometric and energetic criteria for liquid water at 298K ($0.998 gcm^{-3}$) under ambient conditions and at sub-critical conditions at 573K and a density of $0.72 gcm^{-3}$. This work claims that focusing too much on a purely geometrical criteria does not cover the case where two water molecules are subject to repulsive forces. Under this scenario if a geometry criteria only is applied pairwise repulsion would be considered as a hydrogen bond. This paper concludes that although a purely geometric criteria is sufficient for liquid water at ambient condition it is not suitable for sub-critical water at 573K.

Previous simulation studies, such as those by Buch[67] and Essmann and Geiger[69], have defined a hydrogen bond in terms of geometric and potential energy criteria (G and E respectively). In order to ascertain G and E criteria for ASW, an NVT simulation

of bulk crystalline cubic ice containing 520 water molecules was performed at 10K at zero pressure for 100,000 time steps. The simulation was performed at 10K as that is the same equilibrium temperature as the ASW simulations. Molecular velocities were scaled via a Berendsen thermostat (3.2.2) at every time step 1fs and a cutoff radius of 14 angstroms was applied (in the same manner as for ASW deposition algorithms outlined in section 3.5).The GE distribution function for this bulk cubic ice sample is defined as

$$G\,E(r,E)=\frac{\left\langle \frac{1}{N}\sum_{i=1}^{N} N_i(r,E)\right\rangle}{4\pi r^2 \Delta r \Delta E} \tag{4.1}$$

where N is the total number of molecules, $N_i(r,E)$ is the number of water molecules surrounding the ith molecule that have oxygen-hydrogen separation between r and $r + \Delta r$ and pair- wise energy between E and $E + \Delta E$, and the angle brackets denote an ensemble average. Δr and ΔE are the incremental O-H separation and pair-wise energy bin widths respectively.

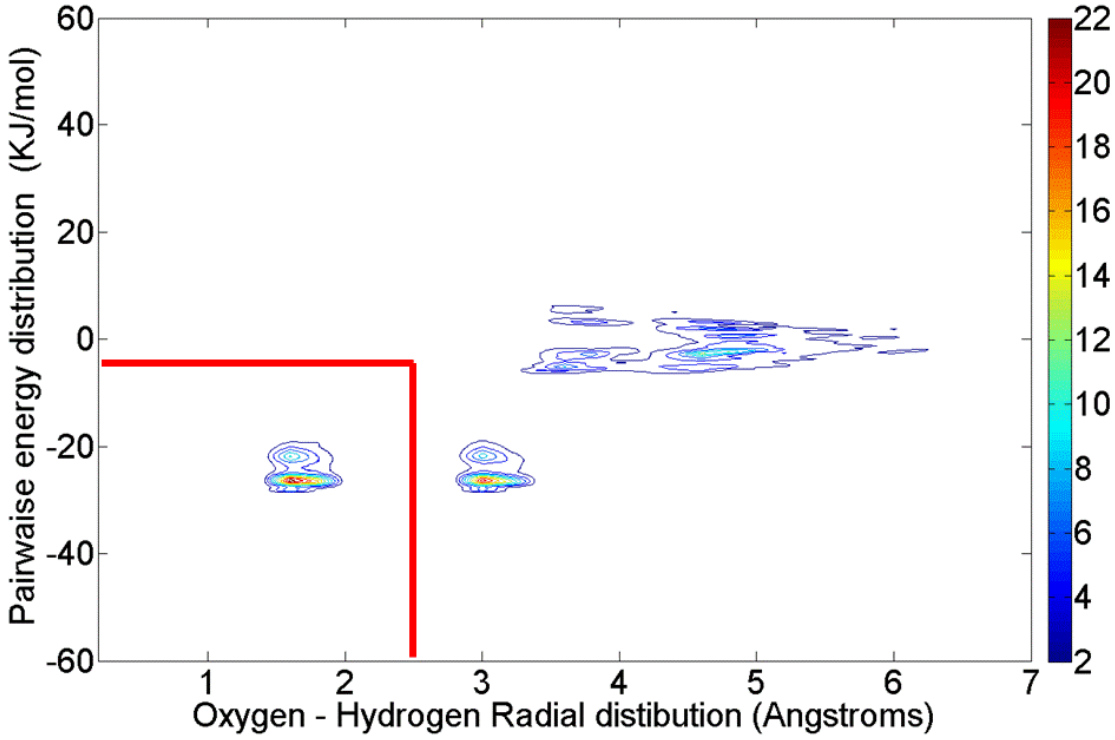

Figure 16: Shows the GE plot for cubic ice at 10K. The first and second peaks at (1.8, -30) and (3.1,-30) corresponds to hydrogen bonding and the next nearest neighbour respectively. Hydrogen bonding is defined in the first red quadrant of this figure.

The results of this simulation are shown in Figure 16. We define the lower quadrant where pair-wise energies are less than 7 $KJmol^{-1}$ and where O–H separations are less than 2.5Å as the region of hydrogen bonding. This is because, given the interaction model for water, we should expect the closest approach of oxygen and hydrogen atoms to be slightly less than the water van der Waals diameter, less the O-H bond length (see Figure 10), i.e. to be slightly less than 2.0 Angstroms. Moreover, given the geometry of a water molecule (see Figure 10 again) we expect the next-nearest O-H distance to be similar to the water model's Van der Waals diameter, i.e. 3.0 Angstroms. We use the same definition of a hydrogen bond for our ASW structures. Because ASW is considerably less ordered than crystalline cubic ice, the first two peaks of the ASW GE plots should be less well-defined. Using these G and E criteria, the average number of hydrogen bonds per molecule for our simulated ASW structures is calculated for each

bin by integrating the respective GE distribution over the range of the GE criteria defined above.

4.2 Results

Three different ASW structures are obtained for each deposition temperature and each substrate, giving a total of 18 simulations. Detailed results from the three simulations at each temperature for each substrate are averaged. In each case we compare our results with those produced by simulating a block of cubic ice, consisting of 520 water molecules, at 10 K on each substrate.

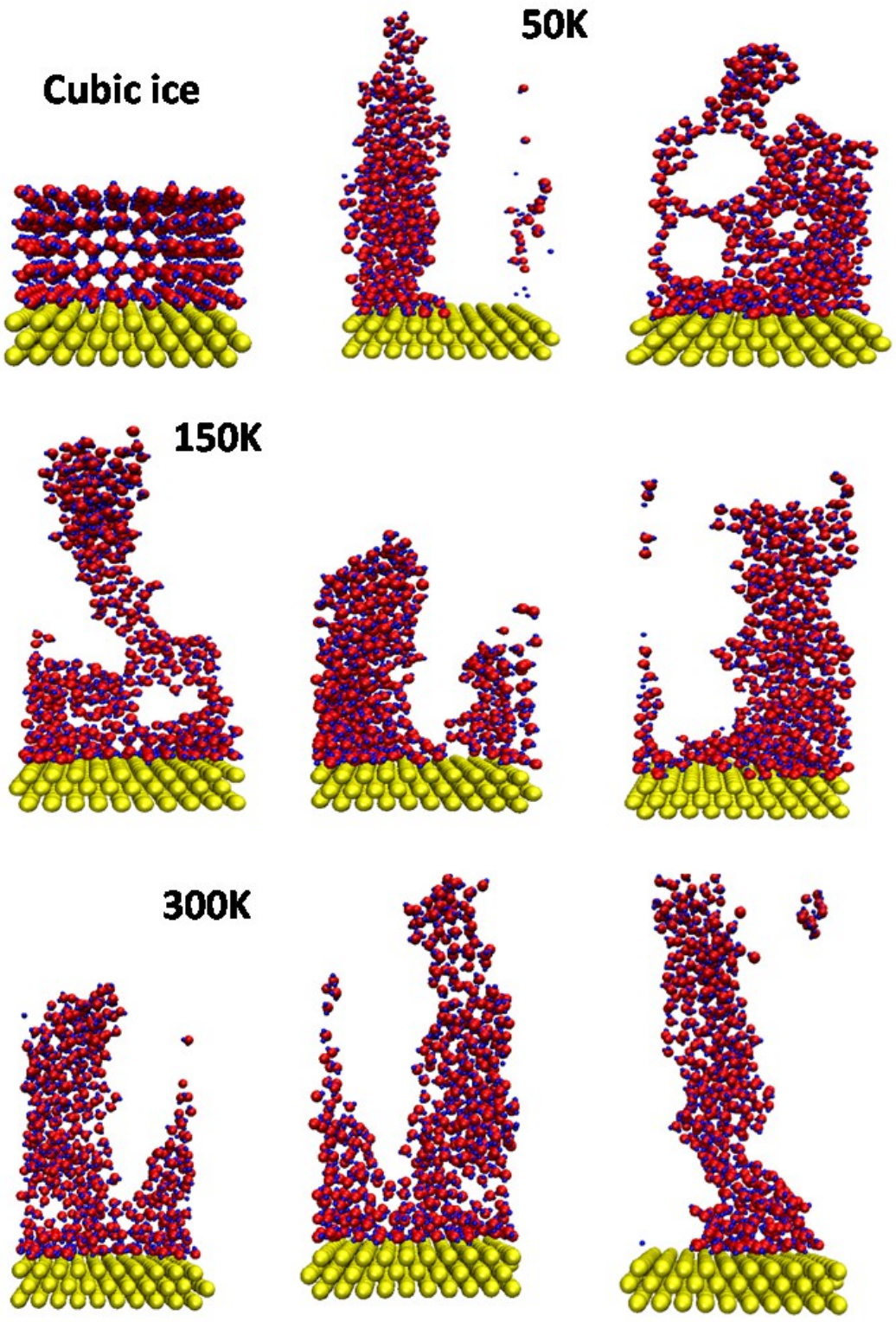

Figure 17: Snapshots of the final ASW structures grown on a Lennard-Jones (hydrophobic) substrate.

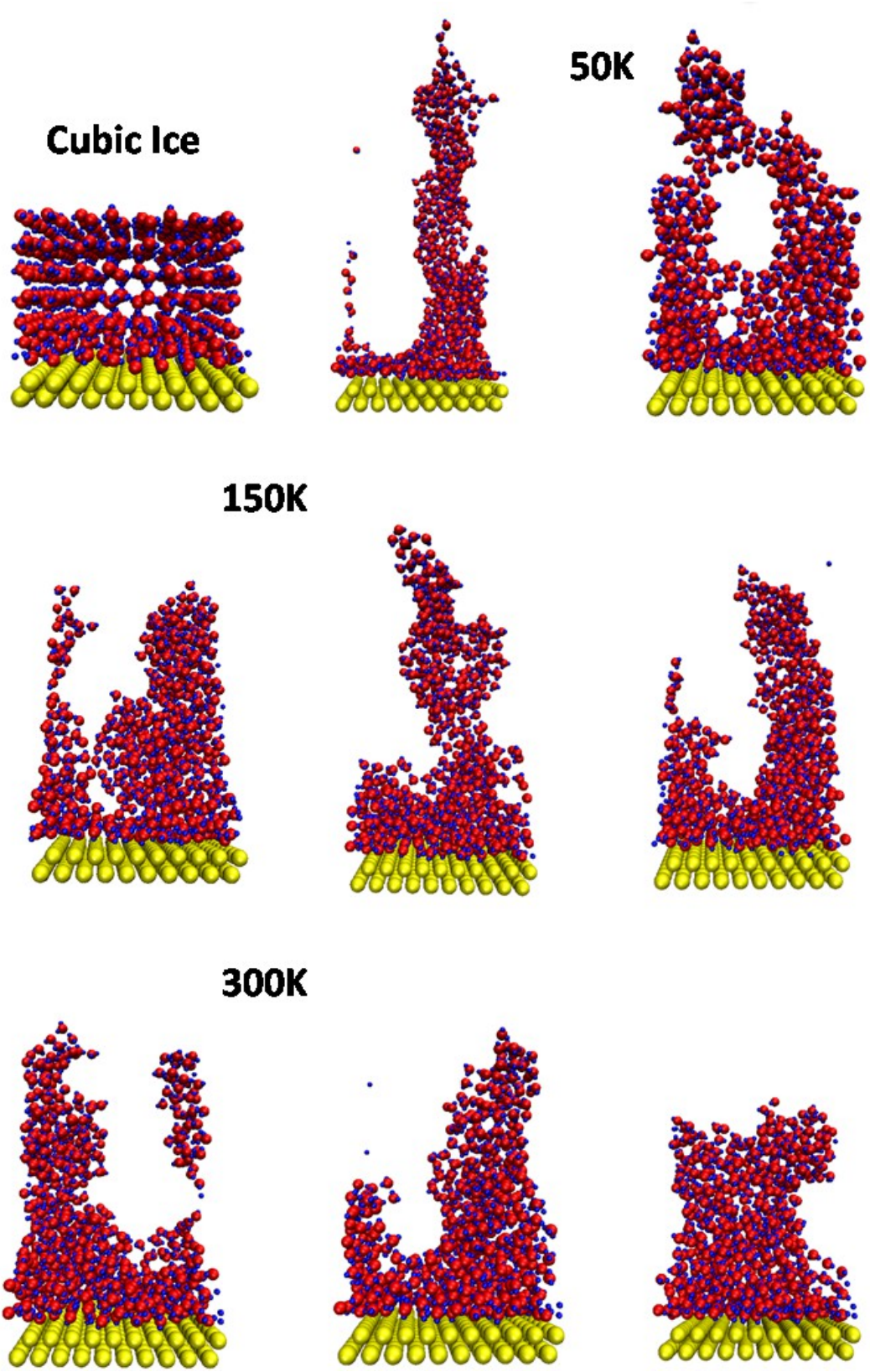

Figure 18: Snapshots of the final ASW structures grown on a cubic ice (hydrophilic) substrate.

Snapshots of the final ASW configurations for each temperature are shown in Figure 17 (Lennard-Jones substrate) and Figure 18 (cubic ice substrate), and we provide some basic observations first before describing the detailed measurements. We see that for the hydrophobic LJ substrate in Figure 17 the final ASW structures tend to consist of long, roughly vertical filaments or strands which are highly porous for all deposition temperatures (for clarity, note that the temperature referred to here is the temperature of the incoming water molecule – the substrate and previously deposited water molecules are always close to 10 K before each deposition impact). These strands tend to be broader where they meet the substrate than at their tops, but it is clear that they do not spread across the whole substrate. Overall, the picture is one of amorphous solid nano-droplets with a high contact angle that lead to long filaments. The snapshots for the hydrophilic surface show somewhat different behaviour. Here, we see much more spreading of deposited water molecules across the substrate, and the structures appear to depend on deposition temperature. For the lowest deposition temperature, 50 K, the snapshots are not very different to those on the LJ substrate at this deposition temperature, except that there is more spreading on the substrate. But for higher deposition temperatures, and at 300 K in particular, there appears to be almost complete spreading of water molecules at the substrate, and the filaments are also much squatter. The results show graphically that surface hydrophobicity effects local surface interactions only. The pore-size distribution of these structures has not been calculated, but both Figure 17 and Figure 18 indicate that there is significant porosity on the scale of the simulation cell and a lesser amount of smaller-scale porosity.

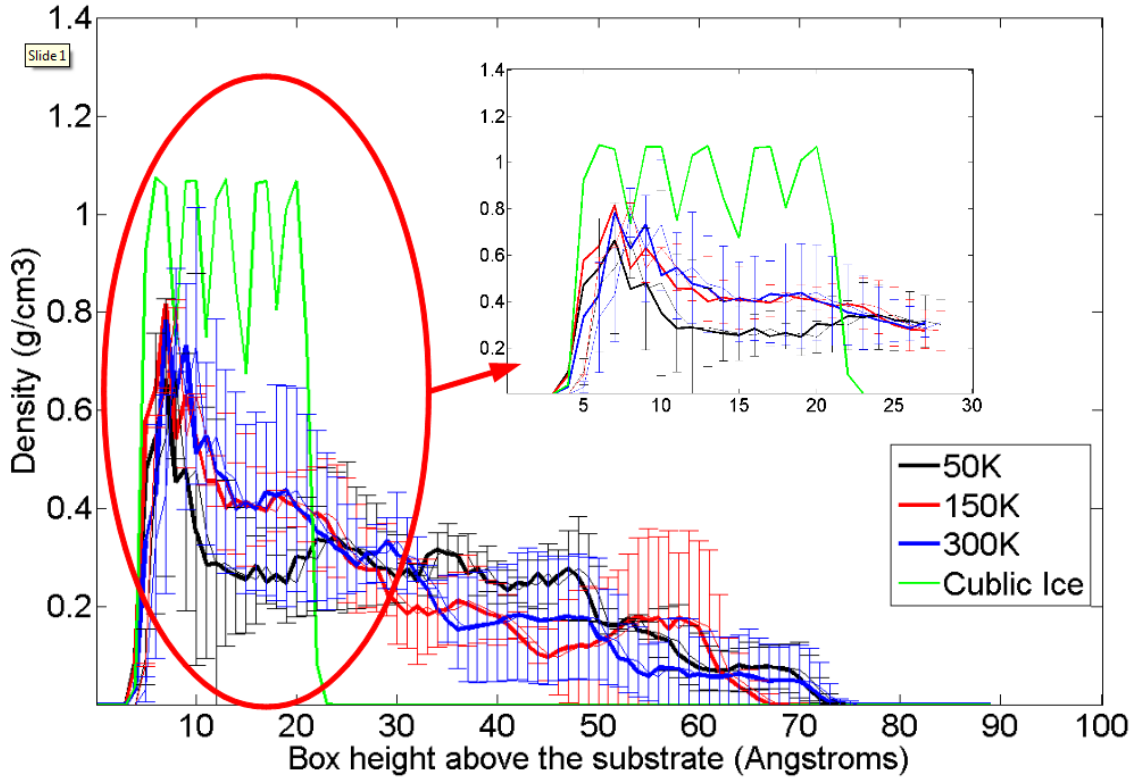

Figure 19: the average density as a function of height above the substrate for a hydrophobic substrate. Statistical errors, as can be estimated by visual inspection of the results, are much smaller for the cubic ice simulation.

We now analyze these structures in more detail. Figure 19 shows the variation of mass density with height above the substrate. We stress that the 'density' referred to here is, according to our definition, the average density in a bin of height 3 A, and that the 'height' is the z-coordinate of the top of each bin relative to the substrates uppermost LJ particle layer. In the inset we can see the effect of packing at the surface, which is similar to that of a fluid adsorbed at a planar solid surface[85]. At least two packed layers can be seen at about 7 A and 9 A, corresponding to the first layer at the substrate and a second layer hydrogen bonded to the first, i.e. an ASW bilayer. The density decays after these first two layers as the vacuum is approached, subject to some considerable fluctuations. Although it is not obvious from inspection of the snapshots in Figure 17, there does appear to be a statistically relevant reduction in the density at less than 25 A from the substrate for deposition at 50K compared to 150 or 300 K, which could indicate a reduction in the degree of steering and/or shadowing at higher

temperatures when fewer molecules have been deposited on the substrate during the initial stages of each simulation. However, at over 25 A above the substrate any clear difference in density between the three deposition temperatures appears to disappear, which could indicate that the degree of steering is independent of deposition temperature once the strands have reached this height. Note that the density in this region between 25 A and 60 A is about 0.25 to 0.3 g/cm^3. This rather low value is the average density at this height and does not correspond to the intrinsic density of the filaments, which is not measured.

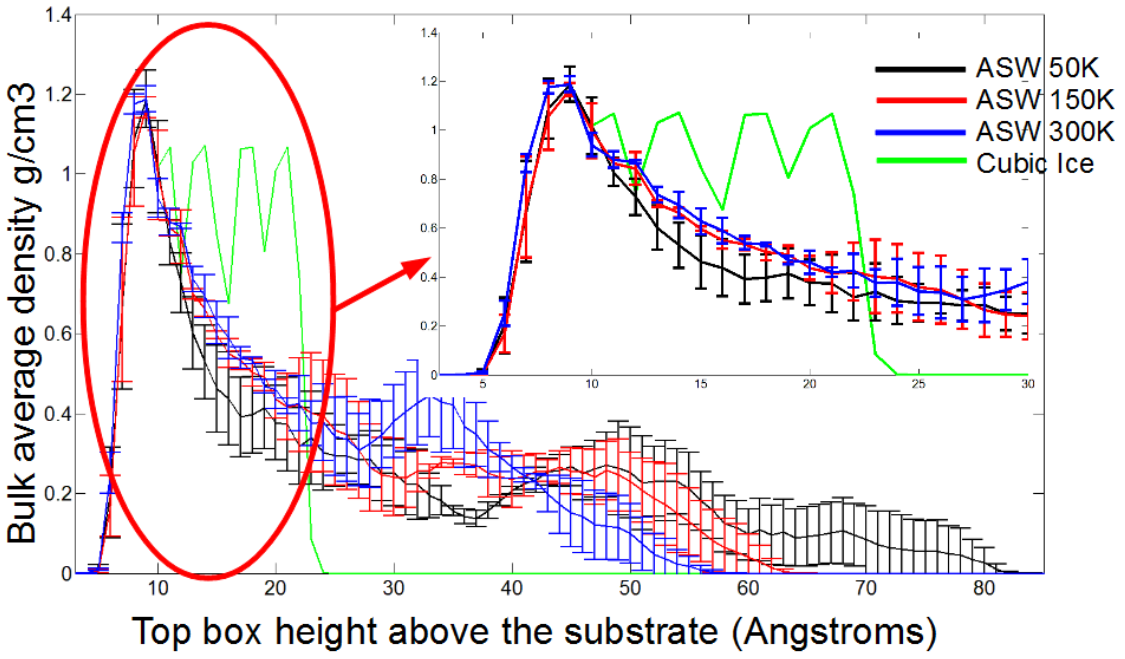

Figure 20: shows the corresponding density plot for a hydrophilic cubic ice substrate

We immediately see quite different results close to the substrate. First, the density right next to the substrate (the first peak) has quite high values (~1.2 g/cm^3) similar to that of HDA ice for all deposition temperatures (remember, the density is defined as the average within a 3A high slab). A second layer of ASW on top of the first is just visible in the inset (except perhaps at 50 K) with density 0.85-0.9 g/cm^3. However, the density quickly decays with height above the substrate. Once again, the density of ASW appears to decay more quickly when deposited at 50 K than at the higher temperatures,

even for this hydrophilic substrate, although this trend is less significant than for the hydrophobic substrate. The density between 25 and 50 A above the substrate for deposition at 50 K and 150 K is roughly the same as for the hydrophobic substrate at about 0.25 – 0.3 g/cm3. However, as is obvious from inspection of the snapshots in Figure 17 and Figure 18, the filaments become increasingly short and squat as deposition temperature is increased.

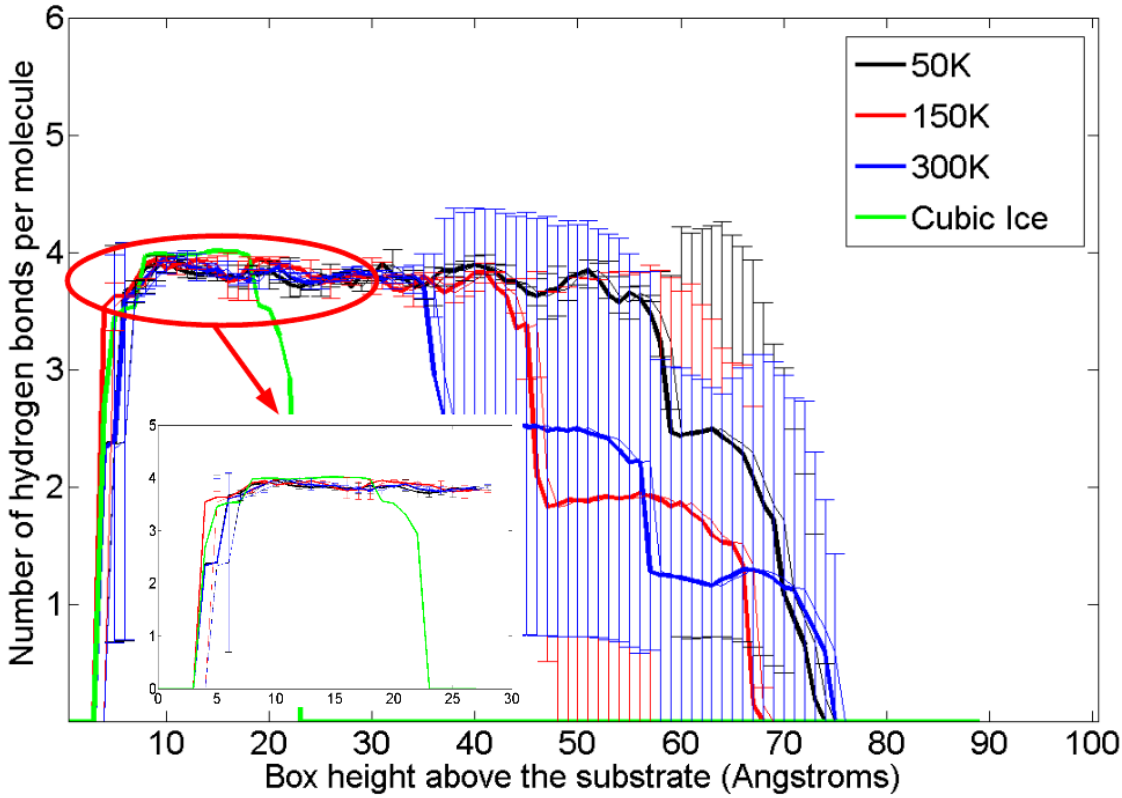

Figure 21: the number of hydrogen bonds per water molecule as a function of height above the substrate for a hydrophobic Lennard Jones substrate.

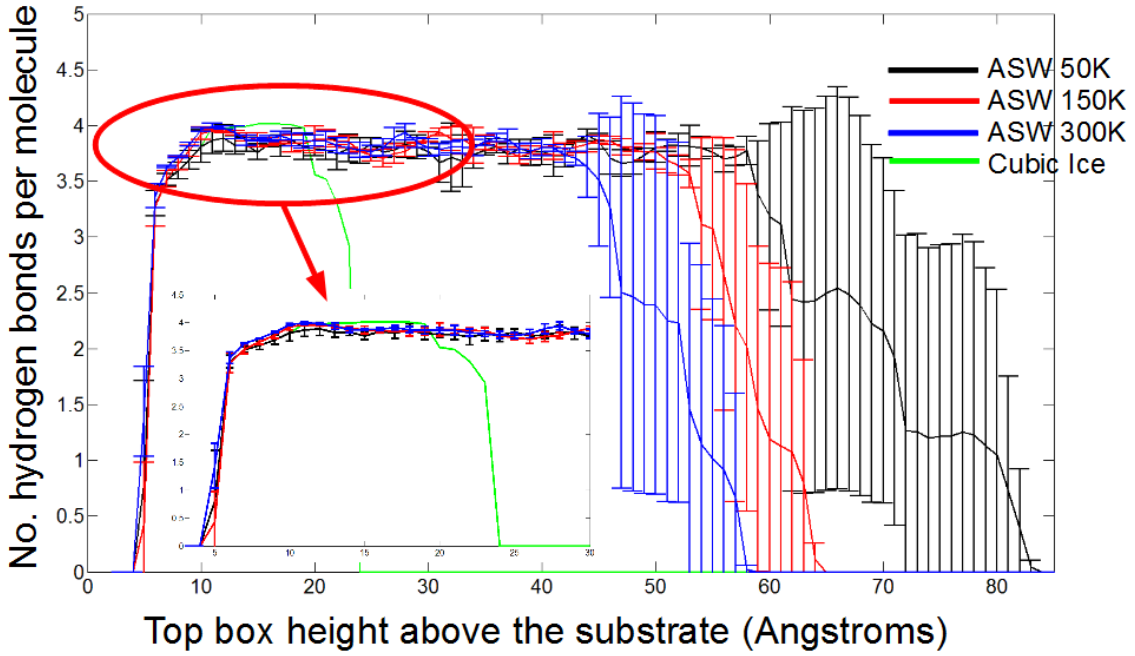

Figure 22: the number of hydrogen bonds per water molecule as a function of height above the substrate for a hydrophilic cubic ice substrate.

Figure 21 and Figure 22 show how the average number of hydrogen bonds per water molecule varies with height above the substrate for each deposition temperature for the LJ and cubic ice substrates. Unlike density, the number of hydrogen bonds per water molecule appears to be unaffected by either temperature or the kind of substrate. Close to the substrate there are about 3.85 bonds per molecule, but this decays to about 3.7 with increasing height above the substrate. This result broadly agrees with the previous results of Buch[67] and Essman and Geiger[69] who found from their very different simulations on average 3.75 hydrogen bonds per water molecule.

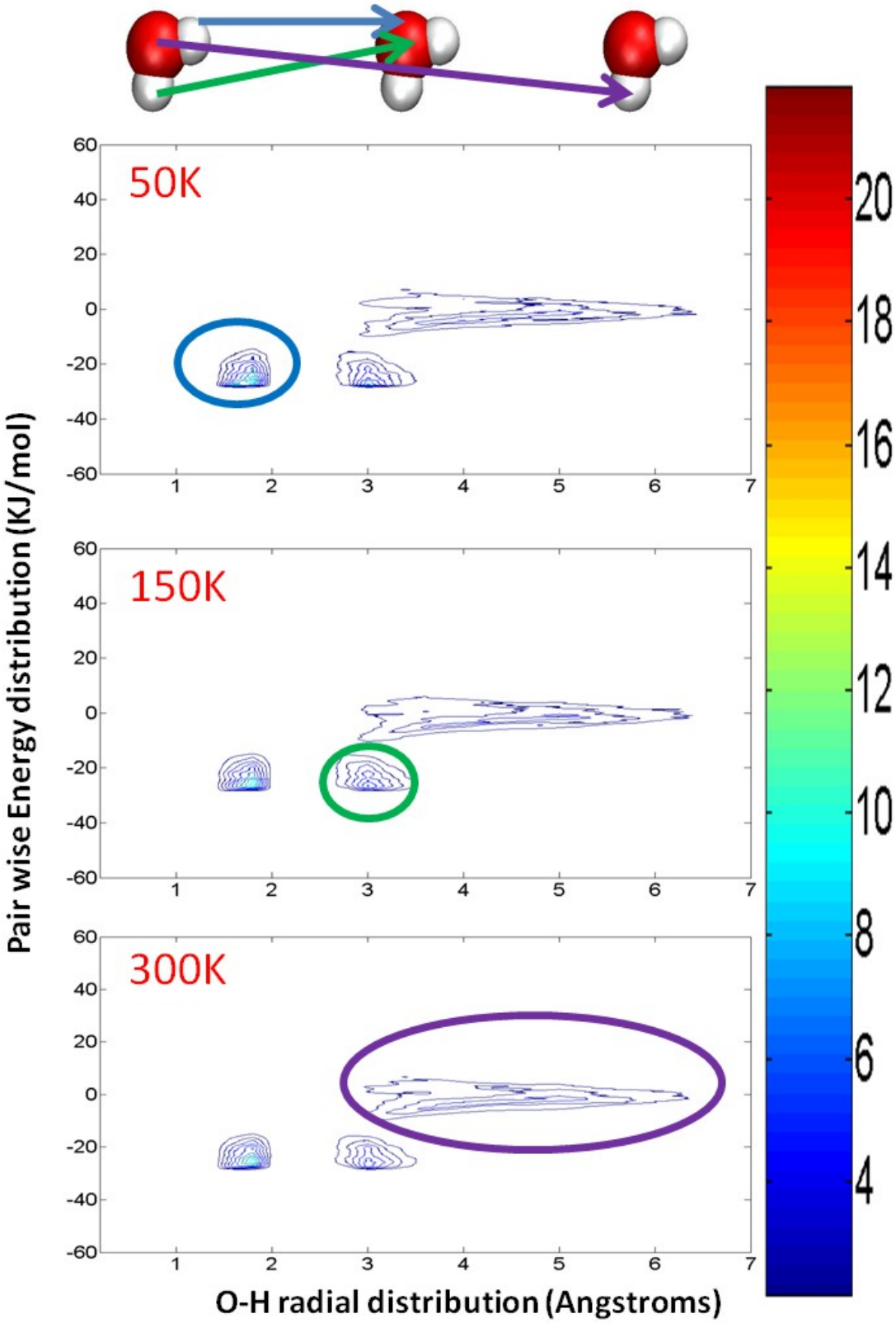

Figure 23: Shows the GE plots for ASW grown on a hydrophobic Lennnard Jones substrate.

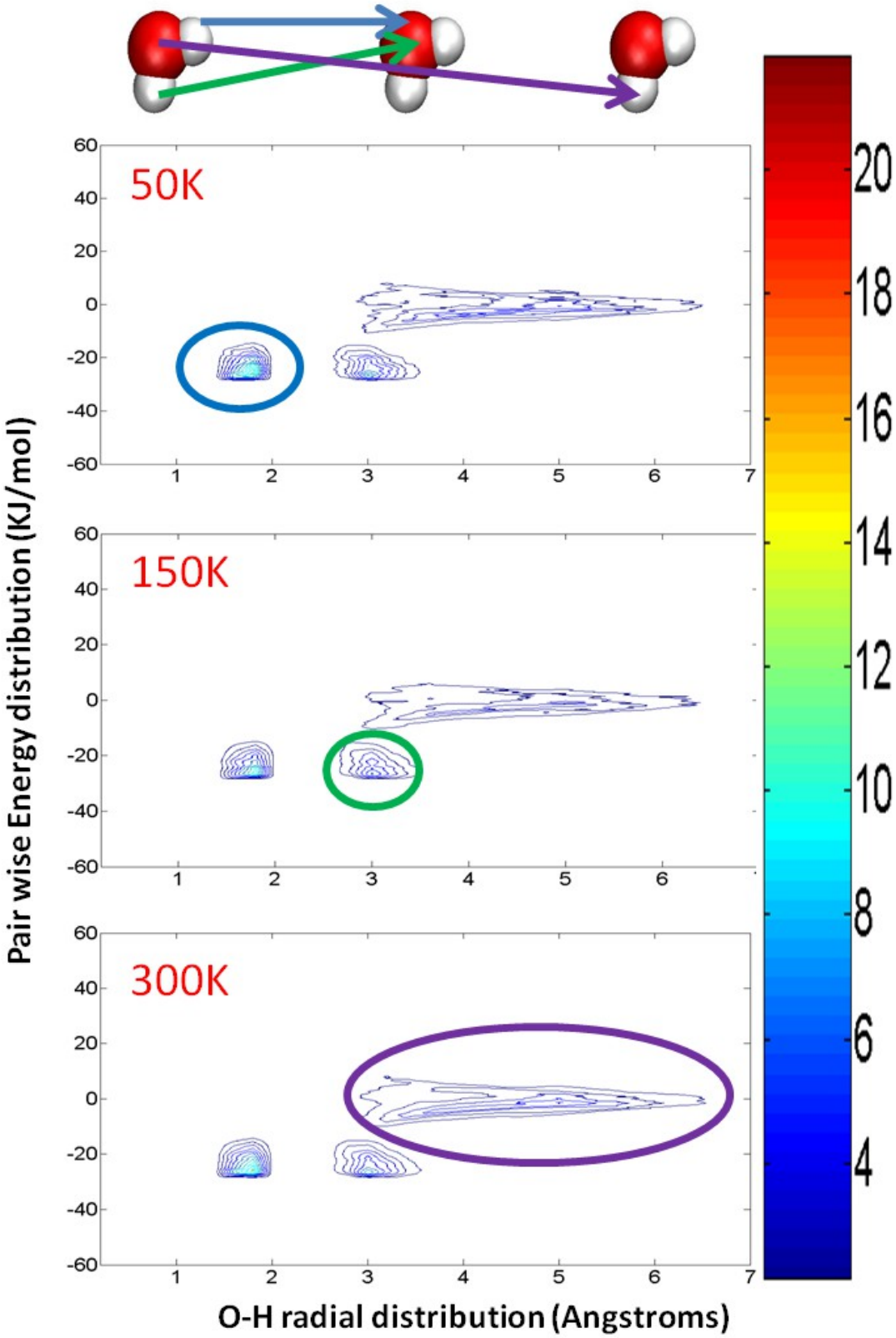

Figure 24: Shows the GE plots for ASW grown on a hydrophilic Cubic ice substrate.

Figure 23 and Figure 24 display the GE contour plots, as defined via equation (6), for ASW at each deposition temperature on the LJ and cubic ice substrates. Once again, these GE plots suggest that neither deposition temperature or substrate kind significantly affect ASW structure at small distances, i.e. the local structure (at the level of nearest and next nearest neighbours) is dominated by hydrogen bonding.

4.3 Discussion

It is clear from these results that there is a significant dynamical effect that causes depositing water molecules to form long amorphous filaments. We call this effect steering and shadowing and suggest that it is caused by the competition between attractive, essentially electrostatic, interactions of the substrate and the growing ASW film on depositing water molecules. We propose that steering influences our simulations as follows. Because the hydrophobic substrate interacts relatively weakly with water molecules at long range steering dominates for this substrate. Of course, the first water molecule can settle anywhere on the substrate, but subsequent water molecules are attracted towards the first. The effect is reinforcing, and soon a small amorphous solid nano-droplet is formed, out of which a filament grows. This nano-droplet remains stable on the hydrophobic substrate due to the fact that surface diffusion is extremely limited on a 10K substrate, and thus hydrogen bonding (surface tension), plays a dominant role in stabilising this nano-droplet. As more water molecules are deposited, they are steered onto this nano-droplet. The incoming molecule strikes this nano-droplet not only with the initial deposition velocity but also the accelerated velocity which the incoming molecule acquires through forming hydrogen bonds with previously deposited molecules in this nano-droplet. Consequently, the temperature of the nano-droplet increases initially at the impact point. Thermal energy from this impact point is then transferred throughout the ASW by heat conduction. This thermal transfer from molecule to molecule can be thought of as a propagating thermal wave originating at the impact point and dispersing throughout the ASW structure. As this thermal wave propagates through the nano-droplet, previously deposited water molecules reconfigure into more energetically favourable positions. This localised annealing brought about

through thermal dissipation from an impact point is called 'impact annealing', and is considered important for ASW formation as it provides kinetically hindered or trapped ASW molecules the kinetic energy required to reconfigure and form more hydrogen bonds, thereby stabilising these long ASW filaments. The rate at which the filament grows depends slightly on temperature. At the lowest deposition temperature steering is most dominant and so the average water density decays quickly until ASW growth is completely determined by steering via vertical growth of the filament. At higher deposition temperatures steering is not so dominant so quickly, i.e. more water molecules are required until steering is dominant and growth occurs via the filament.

On the other hand, the hydrophilic substrate competes roughly equally with any deposited water molecules in terms of attractive interactions (as both the substrate and ASW have the same long range interactions), and so no obvious steering effect is seen initially. Instead, deposited water molecules are spread across the substrate quite evenly. Steering only starts to dominate when, by chance, one region of the ASW film has grown significantly higher than other regions. Since the probability of this happening also depends on the deposition temperature, we find that ASW structures on the hydrophilic substrate depend strongly on deposition temperature. In other words, the steering effect is weaker for the hydrophilic substrate, and weakens further with increasing deposition temperature. Hence the effect of temperature is most obvious for the hydrophilic substrate. This basic conclusion agrees with the work of Wilson et.al. [68]

This steering effect, which is influenced by both the substrate and temperature, dominates in most, if not all, the simulations presented here and so is clearly important. Yet it has not been remarked on before in other simulations of ASW formation. This is probably because of various issues with the simulation strategies used in that earlier work, described in section 1 above. Note that Kimmel et.al., who studied the very simple deposition model of cubes on a cubic lattice, also found significant mesoporosity and growth of ASW filaments. However, mesoporosity and filament growth in their study occurs due to shadowing, which is only apparent at low deposition angles. There can be no steering in their study. Wilson et.al. also observed significant microporosity in

their simulations that varied with deposition temperature, but attributed it to what they call ‘shrouding’, which we interpret as shadowing. Due to the smaller number of water molecules deposited, their shorter cutoff range and deposition height, and their use of a hydrophilic substrate they did not appear to observe the filaments seen in Figure 17 and Figure 18. Our simulations are the first to highlight the importance of steering in ASW formation. Shadowing might also occur to a degree in our simulations, but we leave discussion of the relative importance of each effect to Part II of this work.

Interestingly, steering might have been observed previously in experiments concerning ASW. Donev et.al.[40] performed water PVD experiments on to a cold 80K gold substrate and found that depositing water molecules formed hemispherical clusters on a hydrophobic substrate. Donev et.al. suggest that these clusters form via a steering effect because i), their water molecules are deposited normal to the substrate and so shadowing is not experienced during this experiment, and ii) surface diffusion is considered to be severely limited on an 80K surface. Our results suggest that it might also be because they used a hydrophobic substrate for which steering is dominant.

Our simulations support the view that deposition conditions (at least over the range of conditions investigate here), or even the simulation strategy, are not very significant for ASW hydrogen bonding statistics. That is, at these low temperatures a high proportion of hydrogen bonds are satisfied, even though most water molecules are at, or near, the ASW surface. In particular, we find that on average each water molecule forms in the region of 3.7 to 3.85 hydrogen bonds, which agrees with earlier work described in section 1. Instead, it is the nature of intermolecular forces themselves which dominate hydrogen bonding, i.e the adsorption energy itself is sufficient to cause significant impact annealing. A quick calculation, also described in the work of Wilson et.al., reveals that more thermal energy is generated by conversion of the potential energy in two hydrogen bonds than is generated by the conversion of kinetic energy for most deposited water molecules, even at a deposition temperature of 300 K. If this energy is conducted away from the impact site sufficiently slowly it will allow the depositing water molecule and its neighbours time to attain a highly favourable configuration. This issue was investigated in more detail by Zhang and Buch who found that most (~ 60%)

impact events caused significant local re-ordering of the hydrogen bond network. Indeed, in the region of 2 to 5 hydrogen bonds per impact were changed as a result of impact annealing, with a significant fraction of impacts changing 10 or more bonds. This local impact annealing can clearly influence ASW structure over a short range (a few molecular diameters), and could also explain the apparent observation of a high contact angle for the ASW structures on the hydrophobic substrate. Without this local impact annealing we might expect to see greater spreading of the ASW across this substrate. However, we suggest that that impact annealing allows water molecules adjacent to the substrate to find very energetically favourable configurations that have a high contact angle. From this argument, it follows that impact annealing further enhances, or reinforces, the effect of steering during the initial stages of each simulation on the hydrophobic substrate.

Impact annealing excites water molecules on the periphery of ASW filaments, allowing these previously kinetically suppressed molecules to form hydrogen bonds with other ASW molecules. As a result there are very few dangling OH bonds in any of our ASW structures; Figure 21 and Figure 22 show that there are between 3.85 – 3.7 hydrogen bonds per water molecule. This is in good agreement with previous simulation studies (Buch[67] and Essman and Geiger[69]) and obervational studies[19,20]. This is particularly important from an astrochemistry perspective as it is currently believed[3] that ASW dangling OH bonds act as a catalyst on interstellar icy dust grains, leading to the formation of more complex interstellar molecules. These results imply that the Langmuir-Hinshelwood reaction mechanism, that is surface chemistry by surface diffusion, could be more likely than the Ely Rideal mechanism, in which an incoming molecule reacts with a chemisorbed reactant see section 1.2.4.

Finally, it is clear that significant mesoporosity on the scale of the simulation cell exists in each simulation, which potentially indicates strong finite-size effects. We consider this mesoporosity could be an artifact of our simulations. It is not clear from these simulations whether a natural length-scale for ASW porosity exists or whether, as seems likely to us, fractal-like behaviour with porosity on all length-scales (larger than a molecule and up to the system size) would be observed in much larger samples of ASW.

5. Electro-steering Simulations and Results

In previous chapters (3. and 4.) MD simulations of PVD of water onto model dust surfaces were performed under conditions relevant to ASW formation. The ASW structures grown appear to depend quite sensitively on the nature of the surface, i.e. its hydrophobic/hydrophilic character, but there is also a dependence on the temperature of depositing water. The aim of this chapter is to better understand the formation process that leads to these structures. Improved understanding of the dominant formation process should ultimately allow prediction of ASW structure for a range of conditions.

Several processes were mentioned in previous chapters that are thought to influence ASW structure. One such process is shadowing, where incoming molecules preferentially adsorb onto the sides of ASW structures growing upwards from (or normal to) the dust grain surface. This process where incoming molecular trajectories are being shadowed by ASW tendril, is enhanced for 'lower' deposition trajectories due to an increase in the apparent collision area of incoming molecule with upwardly growing ASW structures. It is a purely geometrical effect. On the other hand, another mechanism suggested in the previous chapter that might dominate ASW formation and growth processes is 'electro-steering'. With this process, depositing molecules are drawn or deflected strongly towards growing ASW structures through strong and long-ranged electrostatic interactions. The higher ASW structures will have a stronger attractive influence on water molecule trajectories, which in turn leads to their further growth. This effect is a result of both geometric (height of ASW tendril) and energetic (long-ranged electrostatic interactions) factors. Essentially, the symmetry of the dust grain surface is broken and tall thin ASW structures can be expected as incoming molecules are being steered towards the ASW tendril tip. Another factor relevant to ASW structure and growth is impact annealing, whereby the kinetic and potential energy of a deposition event are sufficient to rearrange the local ASW structure around the impact site to generate nearly optimal h-bonded networks. However, this latter factor is ubiquitous, i.e. occurs whether shadowing or electro-steering dominates.

Currently it is uncertain whether shadowing or electro-steering dominates ASW formation, or whether these mechanisms are of roughly equal importance. So, in order to investigate which is more significant for ASW growth a series of simulations will be performed that are designed to isolate, and hence measure, the importance of each effect.

The first batch of simulations aims to isolate the effect of electro-steering by almost eliminating any potential shadowing effects. This is achieved by depositing 1000 water molecules onto a small ASW water cluster consisting of 100 water molecules. Using a small cluster will ensure that we are investigating electro-steering in isolation (i.e. almost no shadowing effects). A range of deposition temperatures are used to investigate its effect on electro-steering, and each kind of surface (hydrophobic and hydrophilic) will also be used. These substrates are the same as those used in chapter 3 (3.7).

A second batch of simulations will investigate the combined effect of shadowing and electro-steering by depositing 1000 water molecules onto a large ASW water cluster consisting of a 450 water molecules. Again, several deposition temperatures and both kinds of surface will be investigated.

A third and fourth batch of simulations consisting of 'ballistic' trajectories designed to elucidate the effect of shadowing by eliminating electro-steering. In these simulations water molecules are assigned random x and y coordinates 25 angstroms above the uppermost ASW water molecule. No molecular forces are computed for the incoming water molecule, and consequently depositing water molecules follow a ballistic trajectory towards the ASW cluster, i.e. no electro-steering is possible. A collision event is detected when a depositing water molecule approaches within a water molecular diameter (3 angstroms) of any ASW water or substrate molecule. At this point the collision location is recorded, the simulation is stopped, and the next trajectory is started. The third and fourth batches of simulations use the small (100 molecule) and

large (450 molecule) ASW clusters mentioned above. For the small ASW cluster used we expect shadowing to be almost entirely absent. Note that the temperature of the deposited water molecules is irrelevant here since it has no effect on their trajectories.

Finally, a batch of non-ASW ballistic simulations will be performed around simple shapes (i.e. a hemisphere and cylinder), again as there are no MD force calculations we will be looking at the effects of shadowing in isolation. These results will serve as a control for ASW comparisons.

Comparison of all these results for a range of temperatures and each kind of surface should allow separation and analysis of individual effects to determine which mechanism dominates under each deposition condition. A detailed summary of the results will be presented at the end of this chapter, and the astrophysical implications will also be discussed.

5.1 Simulation details

The simulation strategy for these simulations is almost identical to that of the ASW simulations in the previous chapter. Depositing water molecules are assigned random initial x and y coordinates with the z coordinate being 25 angstroms above the upper-most ASW water molecule. Initial translational and rotational velocities are selected randomly from a Maxwell-Boltzmann distribution corresponding to the deposition temperature, as described in Chapter 3, with z-component of the translational velocity always towards the substrate. The deposition and annealing phase are identical to that outlined previously in sections 3.5 and 3.6. However, unlike previous ASW simulations, after the hyper-quenching phase the deposited water molecule coordinates are recorded, the deposited water molecule is removed from the simulation, and the original configuration of the ASW cluster is restored, before another water molecule is deposited. The final deposited water molecular coordinates are called the landing coordinates. 1000 water molecules are deposited in this manner for each deposition temperature (50K, 150K, 300K), each kind of substrate and both the small and large

ASW clusters (that is 12 simulations in total). Each set of results are repeated for ballistic trajectories only (a further 12 simulation and 24 in total for this chapter).

5.2 Hydrophobic substrate

5.2.1 Small cluster

An ASW cluster consisting of 100 ASW water molecules should have a nearly uniform distribution of landing coordinates if electro-steering is not significant. On the other hand, if landing coordinates are concentrated around the ASW cluster then steering must clearly be playing a pivotal role in ASW formation. The two figures Figure 25 Figure 26 below show the landing coordinates for three different deposition temperatures and the ballistic control simulation for the case with the small ASW cluster on the hydrophobic substrate.

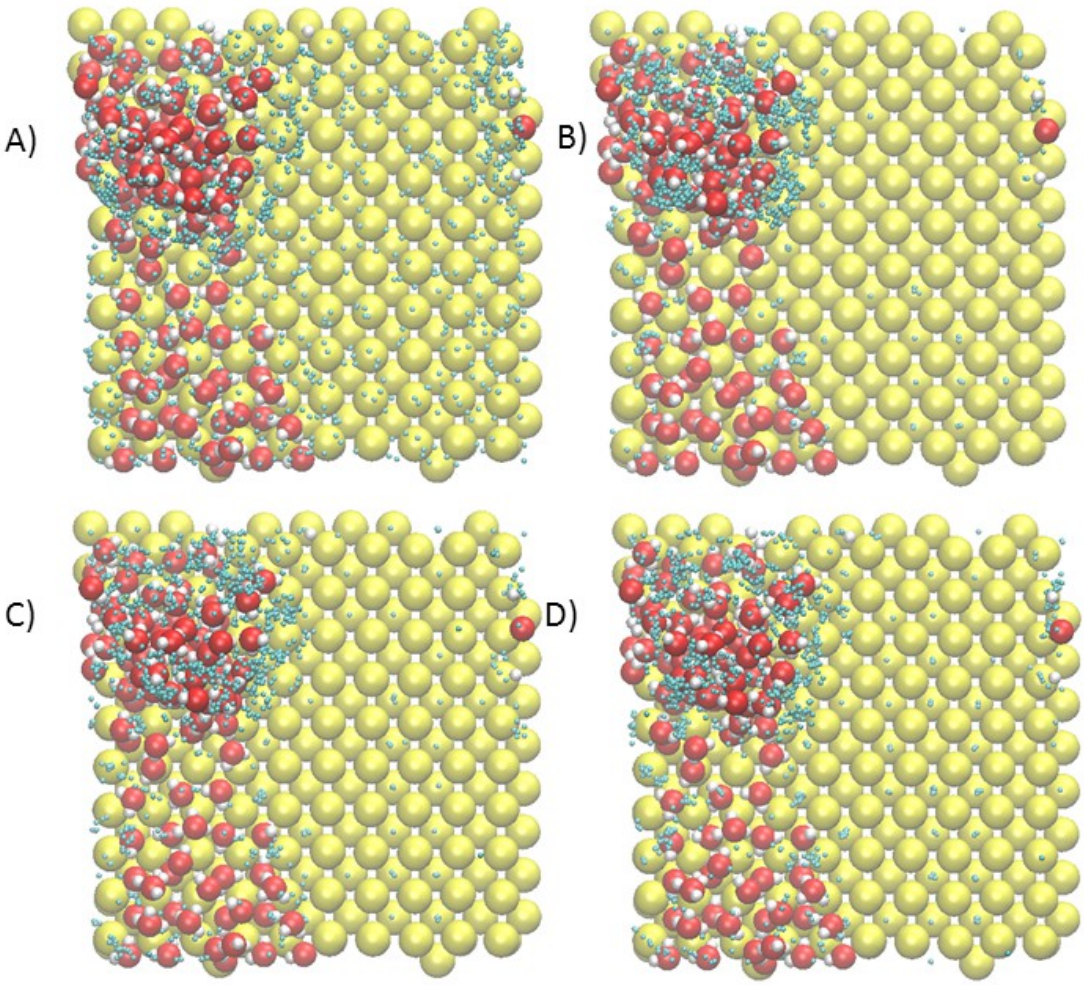

Figure 25: Landing coordinate distribution for three different deposition temperatures; 50, 150 and 300K; B, C and D respectively (A is the Landing coordinates for the ballistic control simulation) for a small ASW cluster on the hydrophobic substrate.

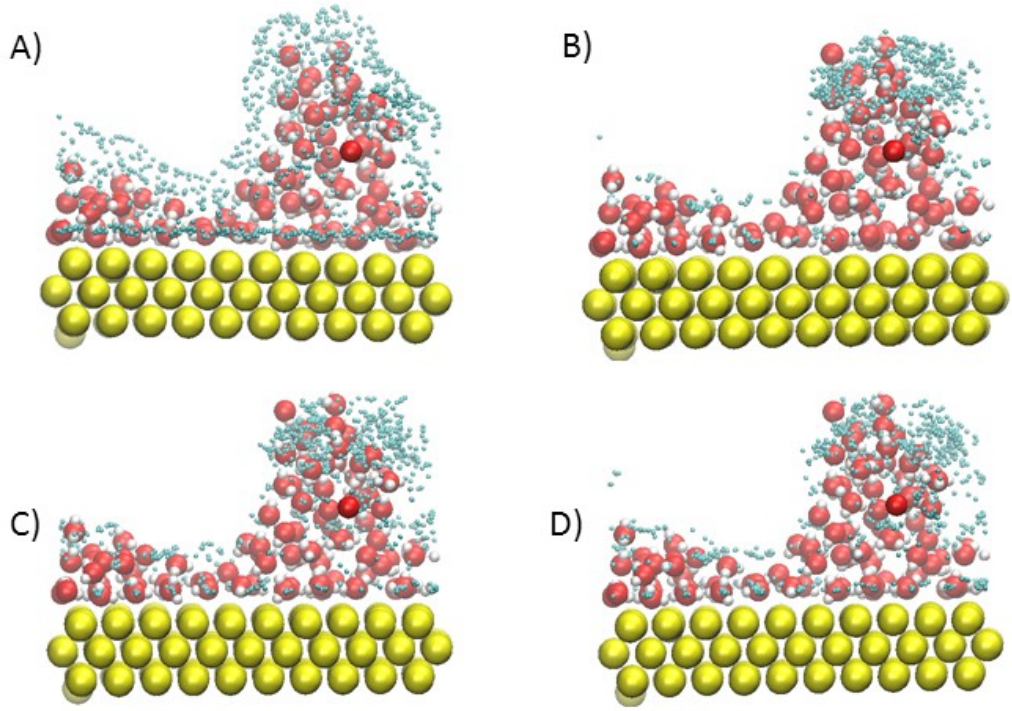

Figure 26: Landing coordinate distribution for three different deposition temperatures; 50, 150 and 300K; B, C and D respectively (A is the ballistic control simulation Landing coordinates) for a small ASW cluster on the hydrophobic substrate.

Figure 25 and Figure 26 above show that there is a greater probability of deposition close to the ASW water cluster for all deposition temperatures compared to the ballistic control simulations. Although there is some clustering of landing coordinates in the ballistic control simulations, indicating a degree of shadowing even for this small cluster and for diffuse initial deposition angles, this clustering is not as significant as for the case when depositing water molecule interacts with the cluster and substrate. We can conclude that depositing water molecules are steered from their initial trajectory by strong interactions with the ASW cluster and substrate. It seems likely that it is the long-range electrostatic interactions that are primarily responsible for this steering, since these interactions would be significant even when the depositing water molecule is far above the ASW cluster, hence the term 'electro-steering'. Figure 25 and Figure 26 show more water molecules 'miss' the cluster as temperature increases, although the effect is not dramatic. This is in line with expectations; higher temperature water

molecules will have greater momentum, on average, and be deflected less from their initial deposition trajectory (or initial ballistic trajectory).

5.2.2 Large cluster

The second batch of simulations used a large ASW cluster of 450 ASW water molecules instead of the small cluster used in the previous batch (5.2.1), but was identical in all other respects. Landing coordinates for this larger ASW cluster are shown in Figure 27 and Figure 28 below.

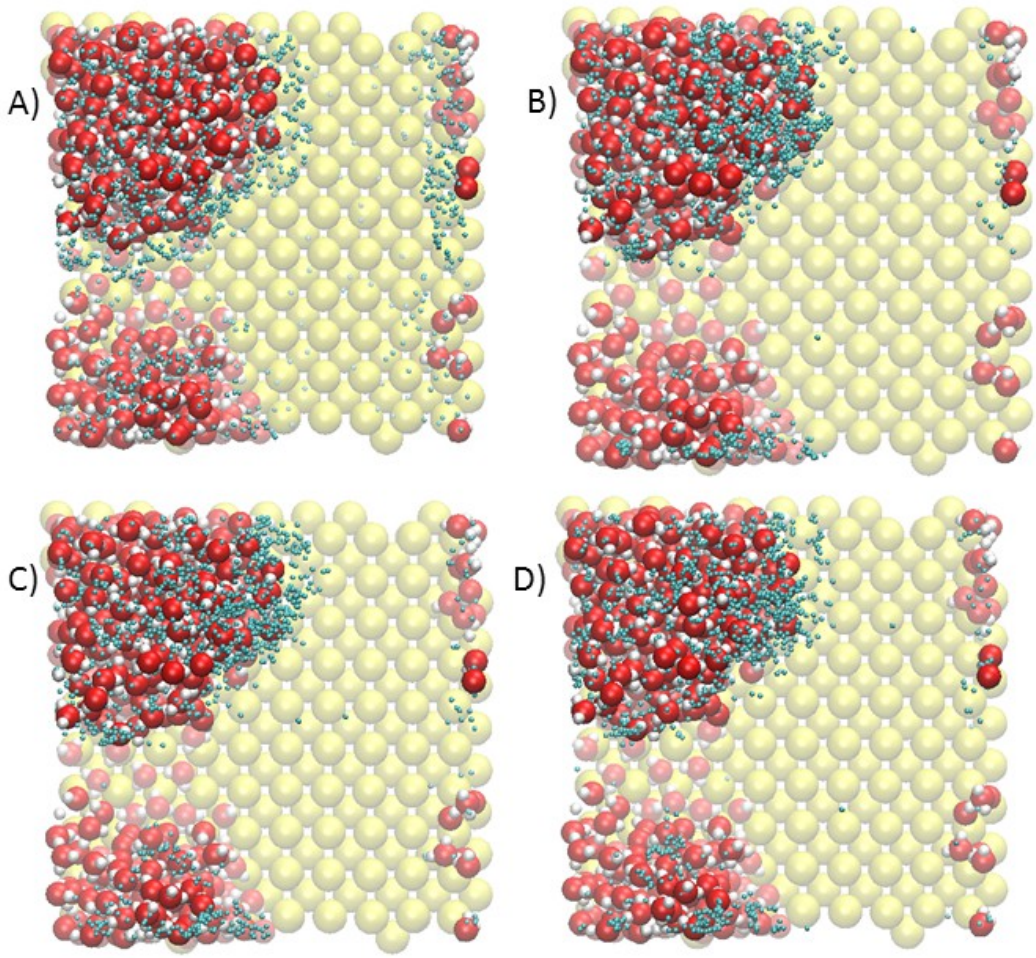

Figure 27: Landing coordinate distribution for three different deposition temperatures; 50, 150 and 300K; B, C and D respectively (A is the ballistic control simulation Landing coordinates) for a large ASW cluster on the hydrophobic substrate.

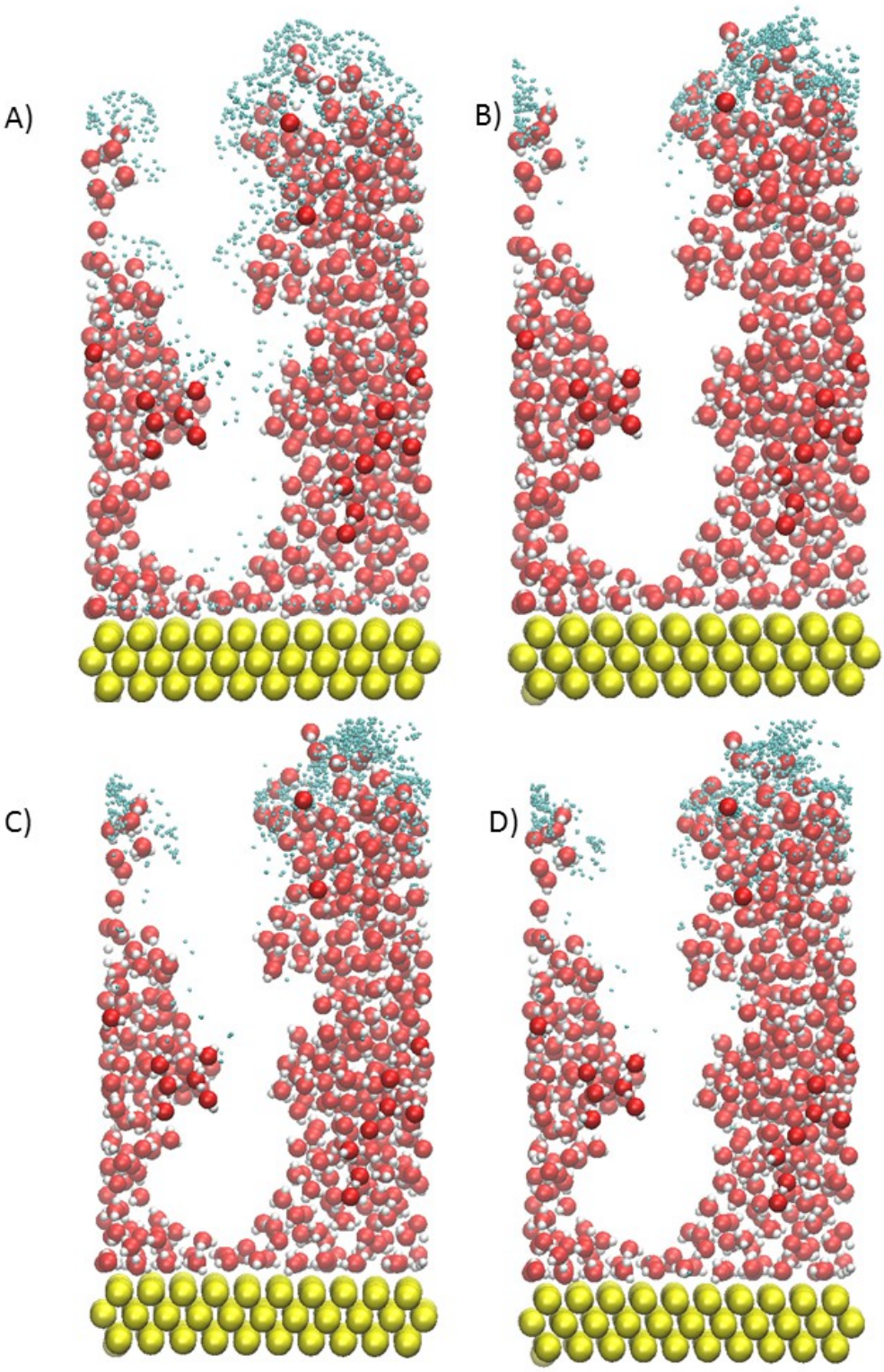

Figure 28: Landing coordinate distribution for three different deposition temperatures; 50, 150 and 300K; B, C and D respectively (A is the ballistic control simulation Landing coordinates) for a large ASW cluster on the hydrophobic substrate.

Figure 27 and Figure 28 show that incoming water molecules are steered towards the peaks of the ASW clusters and consequently do not physisorb into the ASW pores. However, as the deposition temperature increases more incoming water molecules are settling in the ASW pores. Again this is to be expected as incoming water molecules with higher deposition temperatures have more momentum and will be less prone to steering onto the ASW peaks. Figure 28 (A) shows shadowing in isolation, (B, C and D) show electro-steering and shadowing together. These results suggest that in the absence of electrosteering, shadowing, a purely geometric and temperature independent effect, would be important in ASW growth. However, once long-range interactions are included shadowing appears to have very little influence on ASW growth, and steering is dominant. Although the distribution of landing sites in Figures 24 a) and 25 a) (the ballistic simulations that display shadowing only) is denser towards the top of the filaments, there are also a significant proportion of landing sites further down on the sides of the filaments. This would clearly result in very different structures being formed in the absence of long-range electrostatic interactions on the surface. Most likely, these 'shadowing-only' ASW structures would exhibit more lateral growth and hence be shorter and less porous. When water-water interactions are included, which are dominated by electrostatic interactions at long range, we see a very different distribution of landing coordinates. This clearly illustrates how these coral-like ASW structures grow because incoming water molecules are physisorbing onto the ASW peaks creating even taller coral-like structures. Comparing Figure 27 and Figure 28, there are greater concentrations of landing coordinates around the ASW peaks at lower deposition temperatures (comparing B, C and D respectively), which suggests that electro-steering is dependent on deposition temperature, as expected. This agrees with the results shown in Figure 17 and Figure 18 where we see that ASW coral-like structures are taller for lower deposition temperatures.

5.2.3 Landing Coordinate contour plots for a hydrophobic substrate

To provide a quantitative measure of the relative effects of electro-steering in isolation, we generate contour plots of the distribution of landing coordinates using both the

ballistic (shadowing) and electro-steering (shadowing and electro-steering) simulations results. A contour plot is generated for each set of simulations by dividing the substrate area into a 30x30 Angstrom grid with 1x1 Angstrom resolution and assigning each deposition event to an element of this grid. Subtracting the ballistic data from the electro-steering data effectively allows us to investigate the effect of electro-steering in isolation. The Colour Bar situated on the right of the contour plots shows how many water molecules have landed on that particular x-y surface co-ordinate. These contour plots are shown in Figure 29 and Figure 30 below.

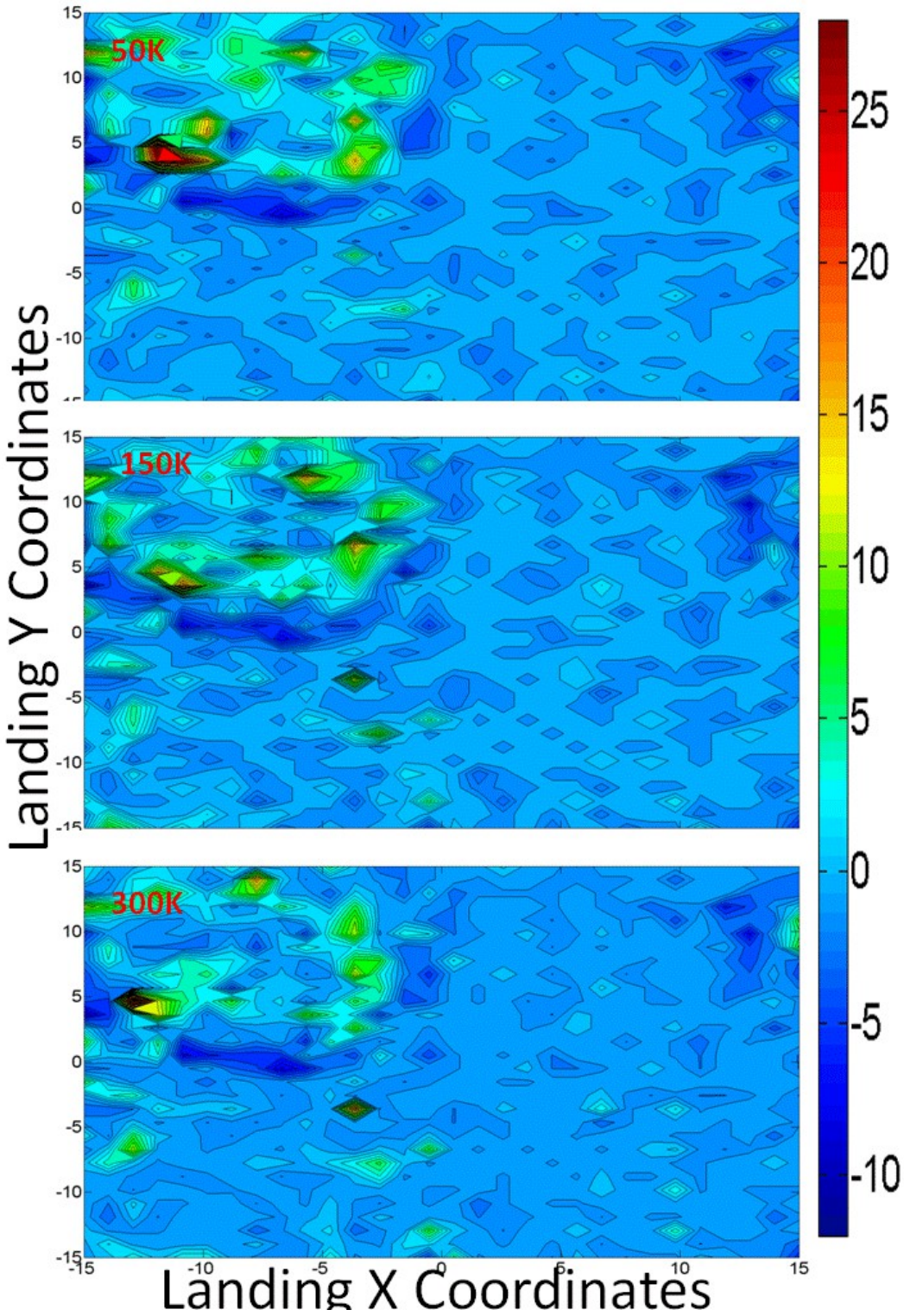

Figure 29: Landing coordinate distribution contour plot with ballistic coordinates removed of 1000 deposited water molecules onto a hydrophobic substrate with an ASW cluster consisting of 100 water molecules at deposition temperatures of; a) 50K, b) 100K, c) 300K.

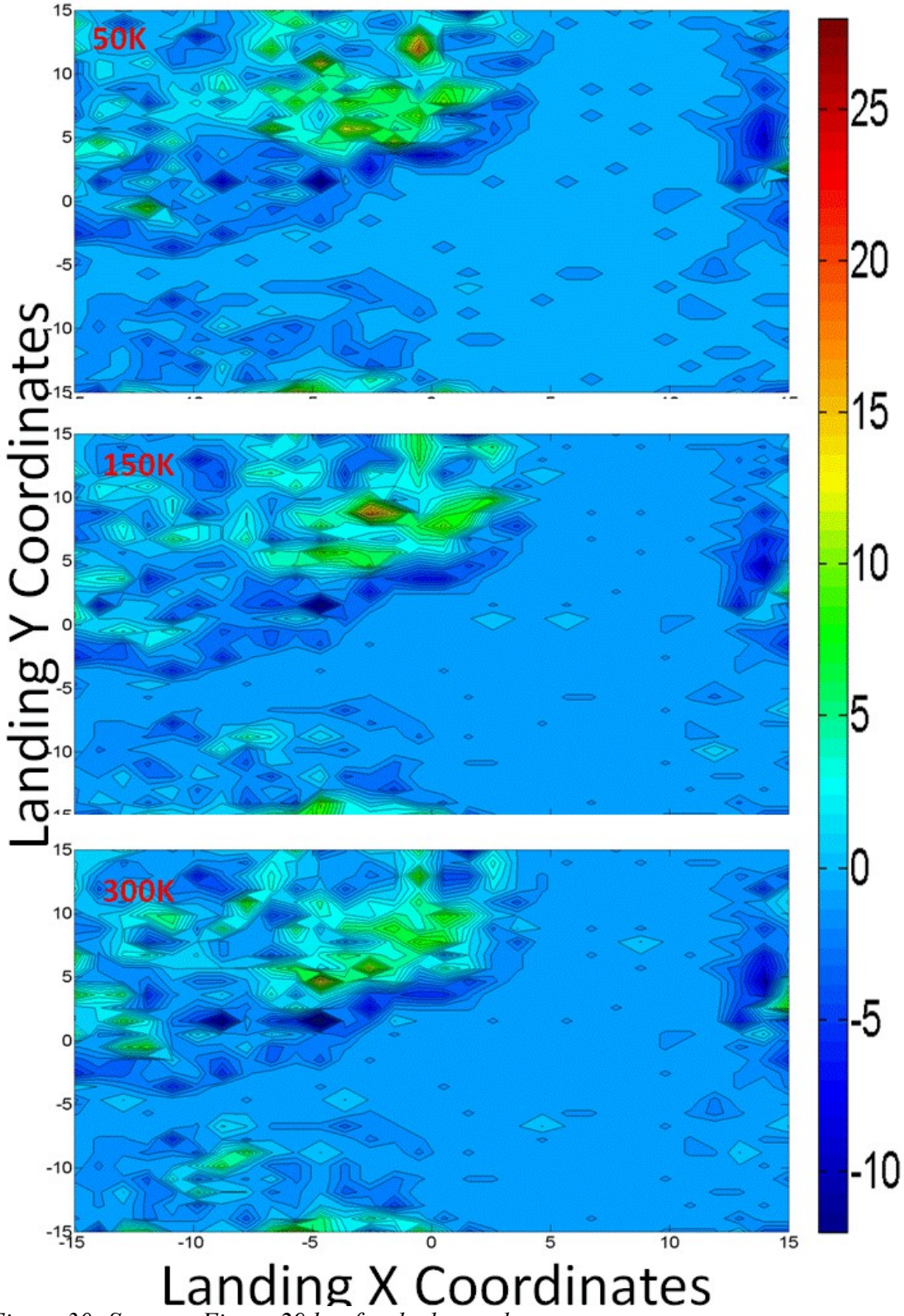

Figure 30: Same as Figure 29 but for the large cluster

Figure 29 shows that for all deposition temperatures there are concentrations of landing coordinates located at x y coordinates (-12, 4) and (-4, 4), corresponding to landing cluster concentrations seen in Figure 25 B, C and D. This can also be seen in Figure 30 around coordinates (-4, 5) and to a lesser extent (-1, 10) when compared to Figure 26 B, C and D. Upon closer inspection of these regions there are an abundance of dangling O-H bonds which appear to be electro-steering incoming water molecules to form new hydrogen bonds with the ASW structure. This suggests why ASW has nearly 4 hydrogen bonds per molecule as shown in the previous results chapter (4) in Figure 21 and Figure 22. That is, these results suggest that depositing water molecules are drawn preferentially to regions where the hydrogen bond network is not complete, and through impact annealing these dangling bonds tend to be eliminated. Figure 29 shows that for lower deposition temperatures there is a higher concentration of landing coordinates clustered near (-12, 4) on the 50K plot. Comparing this cluster at 50K to the same cluster at higher deposition temperatures 150K and 300K shows a distinct reduction in the concentration of landing coordinates. Also comparing cases 50K and 150K shows that electro-steering to coordinate (-12, 4) is less dominant at 150K, allowing electro-steering to other competing O-H dangling bond sites such as (-4, 5), (-6, 10) and (-13, 5).

This is also the case in Figure 30 for the large cluster. Comparison of the concentration of landing coordinates near the top of the ASW filament between cases 50 and 150K, shows a slightly greater degree of clustering at 50K. In both Figure 29 and Figure 30 the 300K case has a more disperse landing coordinate distribution than for the lower deposition temperatures. Again, this suggests that electro-steering for a hydrophobic substrate is deposition temperature dependent.

Another interesting feature of these contour plots is the 'negative' dark blue rings which appear to exist around the ASW clusters. Recall that these plots are generated by subtracting the ballistic results from the standard simulations, so we should expect to see negative values where the concentration of landing sites in the ballistic simulations, when projected onto the x-y plane, is greater than the concentration in the standard simulations. So these negative rings are a result of i) deposition onto the 'sides' of the

ASW filament through shadowing in the ballistic simulations, and ii) steering away from the sides of the ASW filaments in the standard simulations due to electro steering. These results further reinforce the suggestion that without electrosteering ASW cluster growth would be greater in lateral (x-y) directions, resulting in 'squatter' ASW structures with less porosity. This is because without electrosteering incoming molecules would adsorb around the blue ring as they do in the ballistic simulations and not on ASW tendril tips as they do in the electrosteeing simulations. This ASW tendril tip adsorption is essential for further ASW upwards growth. Equally, this supports the suggestion that it is electrosteering that is largely responsible for the highly porous filamentous structure of ASW in these simulations. It can also be seen from Figure 29 that the dark blue ring is more dominant at lower deposition temperatures especially at 50K (particularly in the top left hand corner of the contour plots). This is because steering is more dominant at lower deposition temperatures and therefore the effects of shadowing are more suppressed. This can also be seen in Figure 30 particularly in the bottom left hand corner of the contour plots.

5.3 Hydrophilic substrate

5.3.1 Small cluster

As with the previous substrate a 100 ASW water cluster will essentially investigate the effects of steering in isolation as a function of deposition temperature. Similarly, a 450 ASW water cluster will investigate the effects of steering and shadowing as a function of deposition temperature. The simulation strategy is identical to the previous hydrophobic steering and shadowing simulations. The figures below illustrate the x-y scatter coordinates for three different deposition temperatures and a ballistic control simulation.

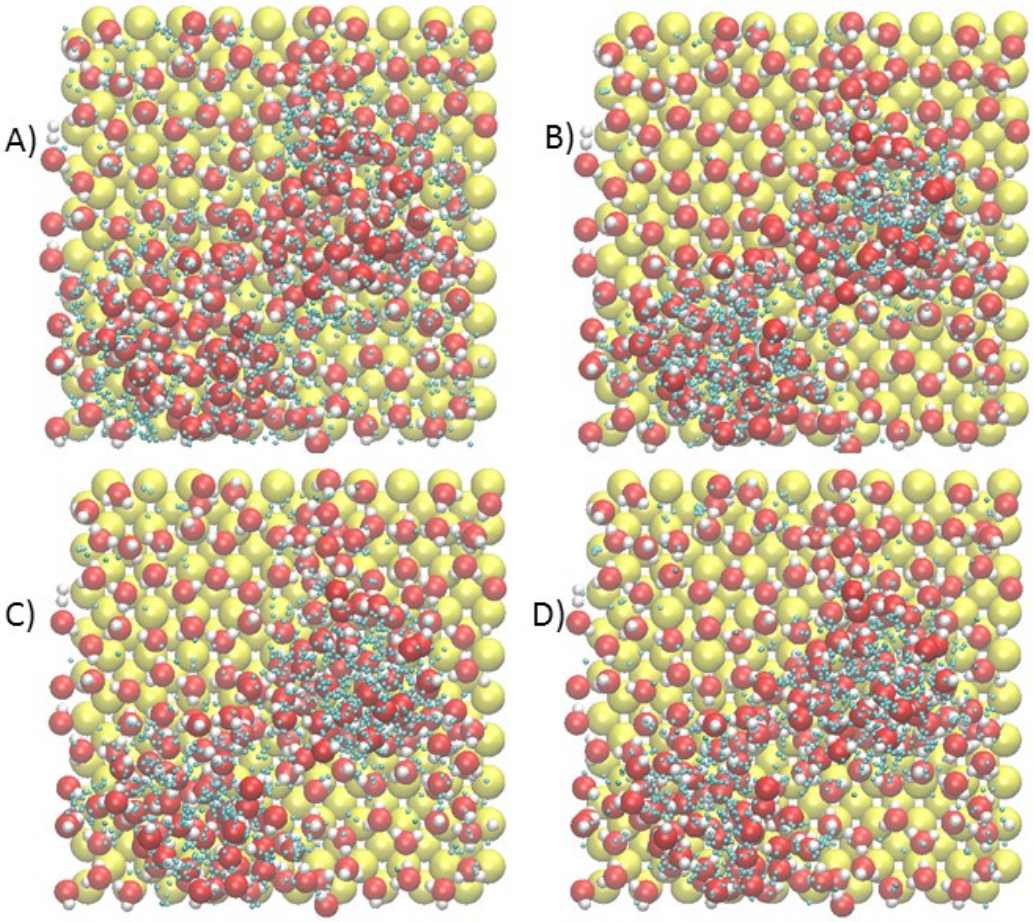

Figure 31: landing coordinates for three different deposition temperatures 50, 150 and 300K (B, C and D respectively) (A is the Landing coordinates for the ballistic control simulation) for a small ASW cluster on the hydrophilic substrate.

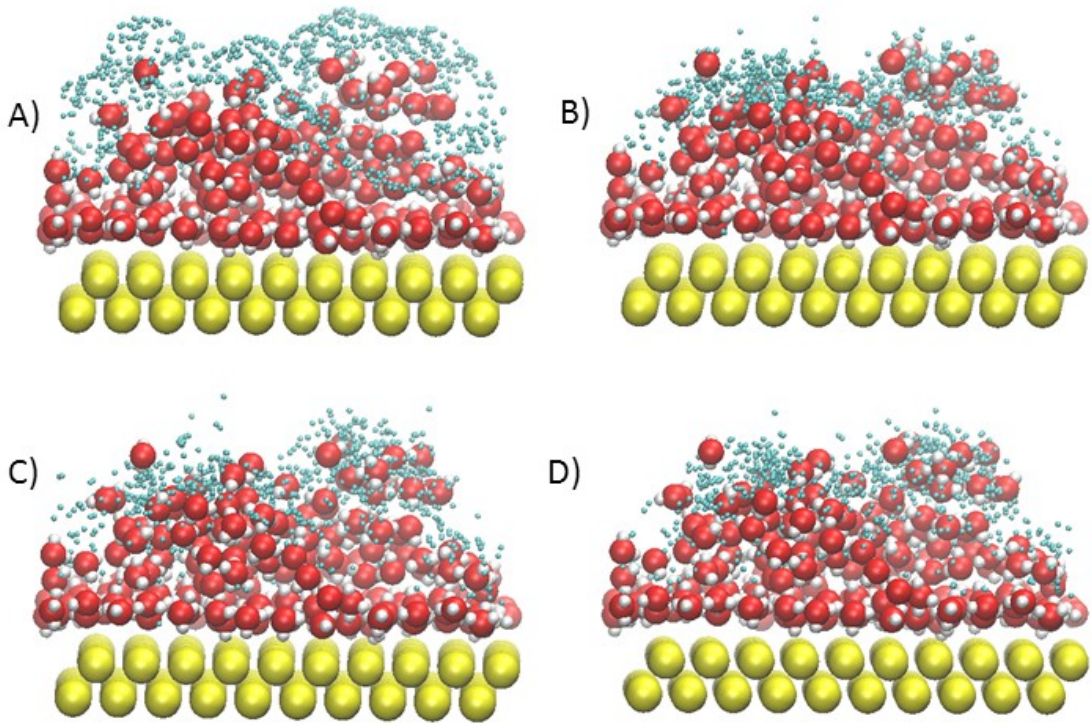

Figure 32: The figure above shows the landing coordinates for three different deposition temperatures 50, 150 and 300K (B, C and D respectively) (A is the Landing coordinates for the ballistic control simulation) for a small ASW cluster on the hydrophilic substrate.

As with the previous substrate Figure 31 and Figure 32 above show that there is a greater probability of deposition close to the ASW water cluster for all deposition temperatures compared to the ballistic control simulations. However, Figure 31A and Figure 32A show that shadowing is important even for this small cluster on a hydrophilic substrate in the absence of electro steering. However, comparing the ballistic simulations (A) with the MD simulations (B, C and D) one can see that electro steering appears to be altering the trajectory of incoming water molecules.

5.3.2 Large cluster

As for the hydrophobic substrate earlier, simulation results for deposition onto a surface with a large ASW cluster are now described. The four figures below illustrate the x-y landing coordinates for three different deposition temperatures and a ballistic control

simulation.

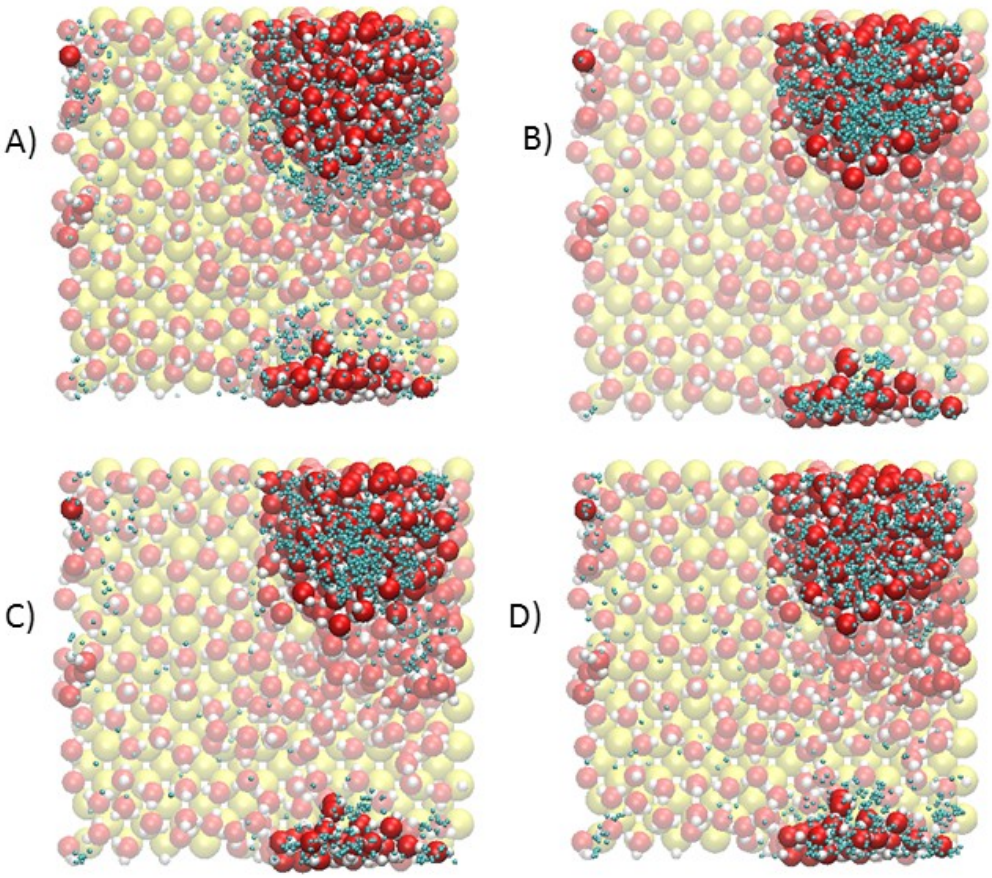

Figure 33: landing coordinates for three different deposition temperatures 50, 150 and 300K (B, C and D respectively) (A is the Landing coordinates for the ballistic control simulation) for a large ASW cluster on the hydrophilic substrate.

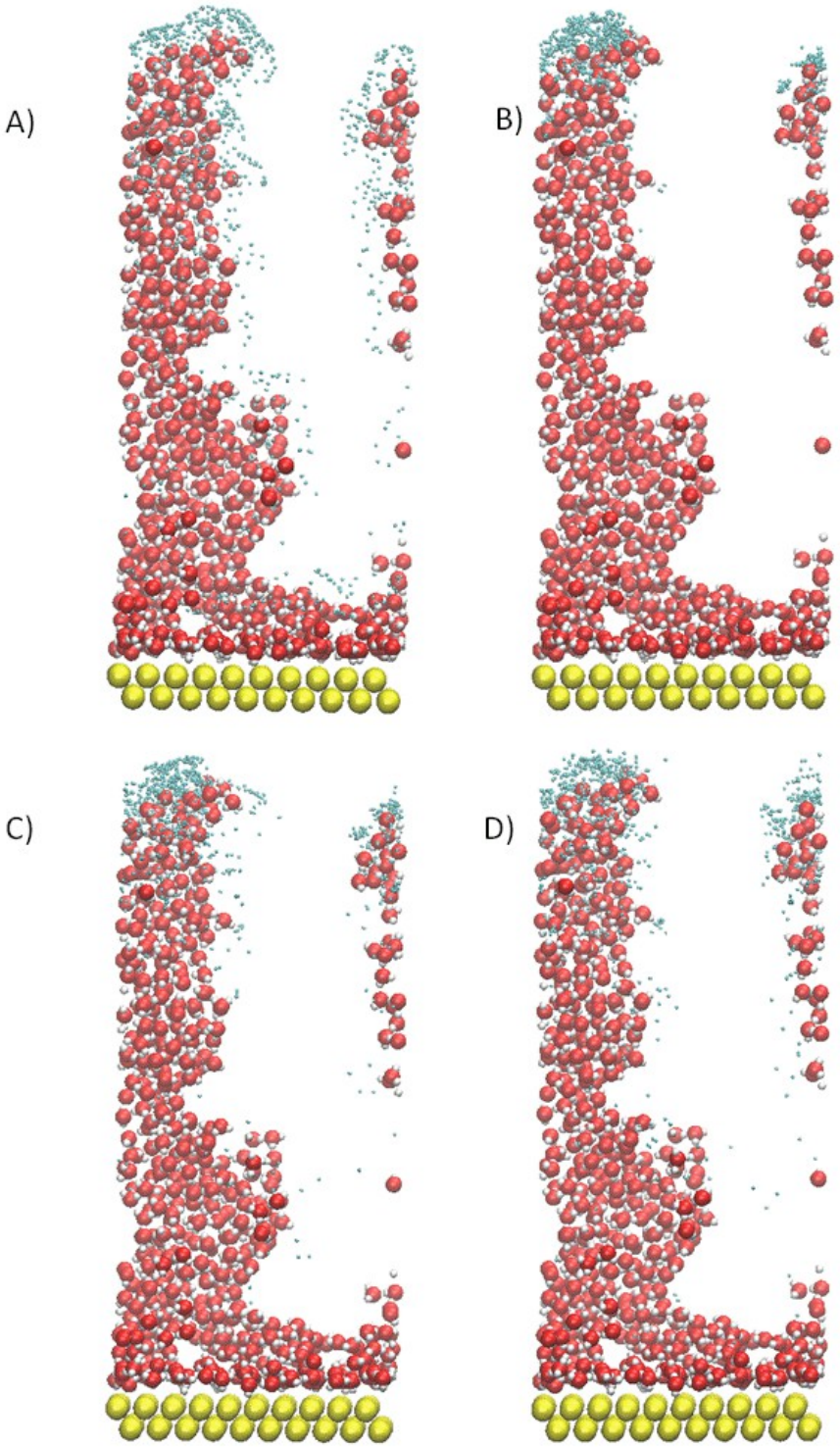

Figure 34: landing coordinates for three different deposition temperatures 50, 150 and 300K (B, C and D respectively) (A is the Landing coordinates for the ballistic control simulation) for a large ASW cluster on the hydrophilic substrate.

Figure 33 and Figure 34 show that the vast majority of incoming water molecules physisorb onto ASW peaks and not in ASW pores. Furthermore, as deposition temperature increases more incoming water molecules physisorb into ASW pores. These observations are consistent with previous large cluster (5.2.2) hydrophobic substrate simulations (see Figure 27 and Figure 28). Figure 33 (A) and Figure 34 (A) show the effects of shadowing in isolation and (B, C and D) show electro-steering and shadowing together. As with the previous large cluster (5.2.2) hydrophobic substrate simulations, although shadowing is important in the absence of long-range electrostatic interactions, steering appears to be dominant when these interactions are included. This is due to the fact that as the coral-like ASW structure grows, incoming water molecules are steering more towards the top of this structure rather than their sides or the substrate. This process further reinforces the effect of steering, producing taller ASW coral-like structures. Looking at Figure 33 and Figure 34, there are greater concentrations of landing coordinates around the ASW peaks at lower deposition temperatures (comparing B, C and D respectively), which suggest that once again electro-steering is dependent on deposition temperature as incoming water molecules with lower deposition temperatures will have lower momentum and consequently will be steered more towards ASW peaks.

5.3.3 Landing Coordinate contour plots for a hydrophilic substrate

As with the hydrophobic substrate 5.2 we generate landing coordinate contour plots for each deposition temperature as shown below in Figure 35 and Figure 36. This will highlight the electrosteering deposition temperature dependence.

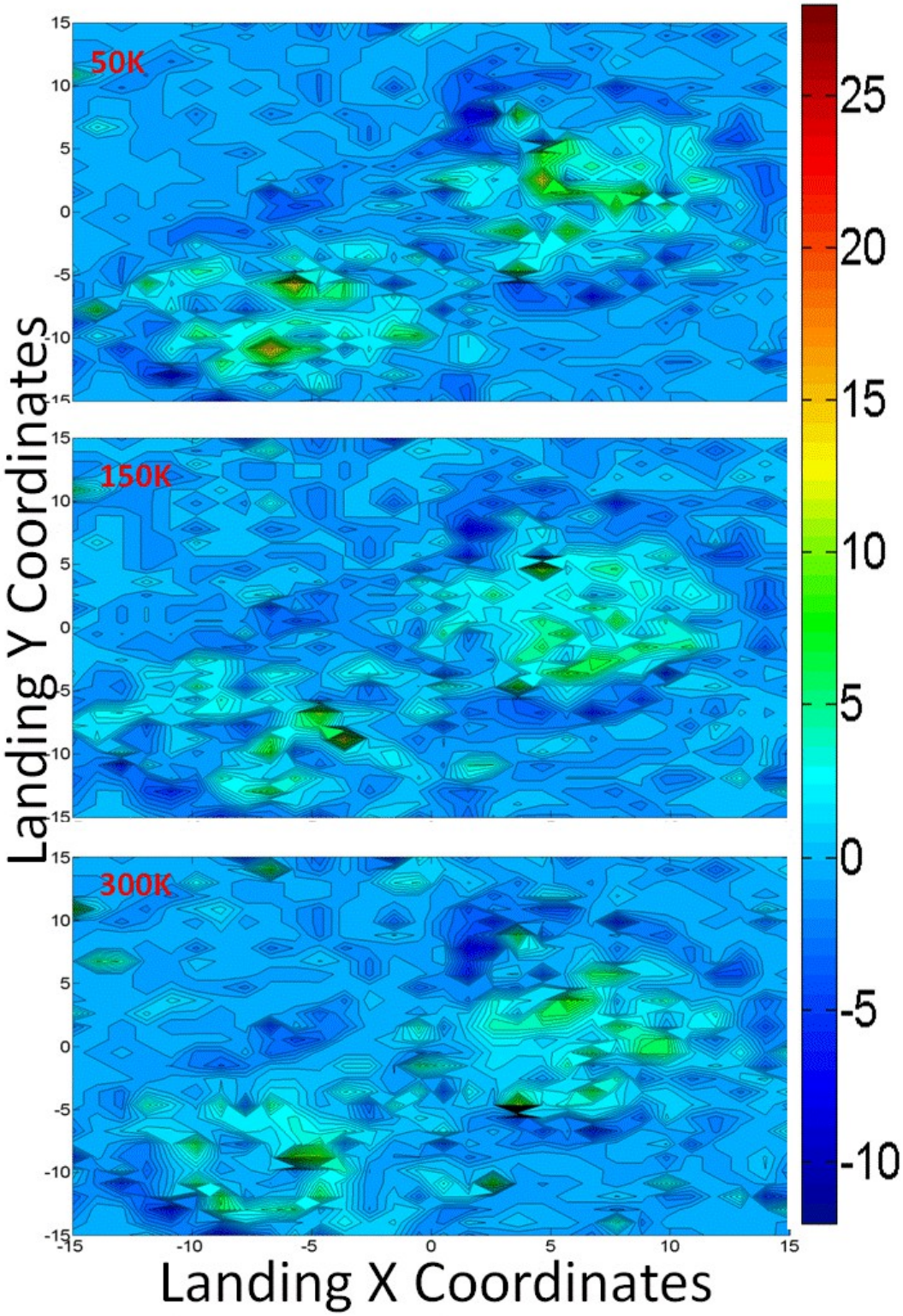

Figure 35: Landing coordinate distribution contour plot with ballistic coordinates removed of 1000 deposited water molecules onto a hydrophilic substrate with an ASW cluster consisting of 100 water molecules at deposition temperatures of; a) 50K, b) 100K, c) 300K.

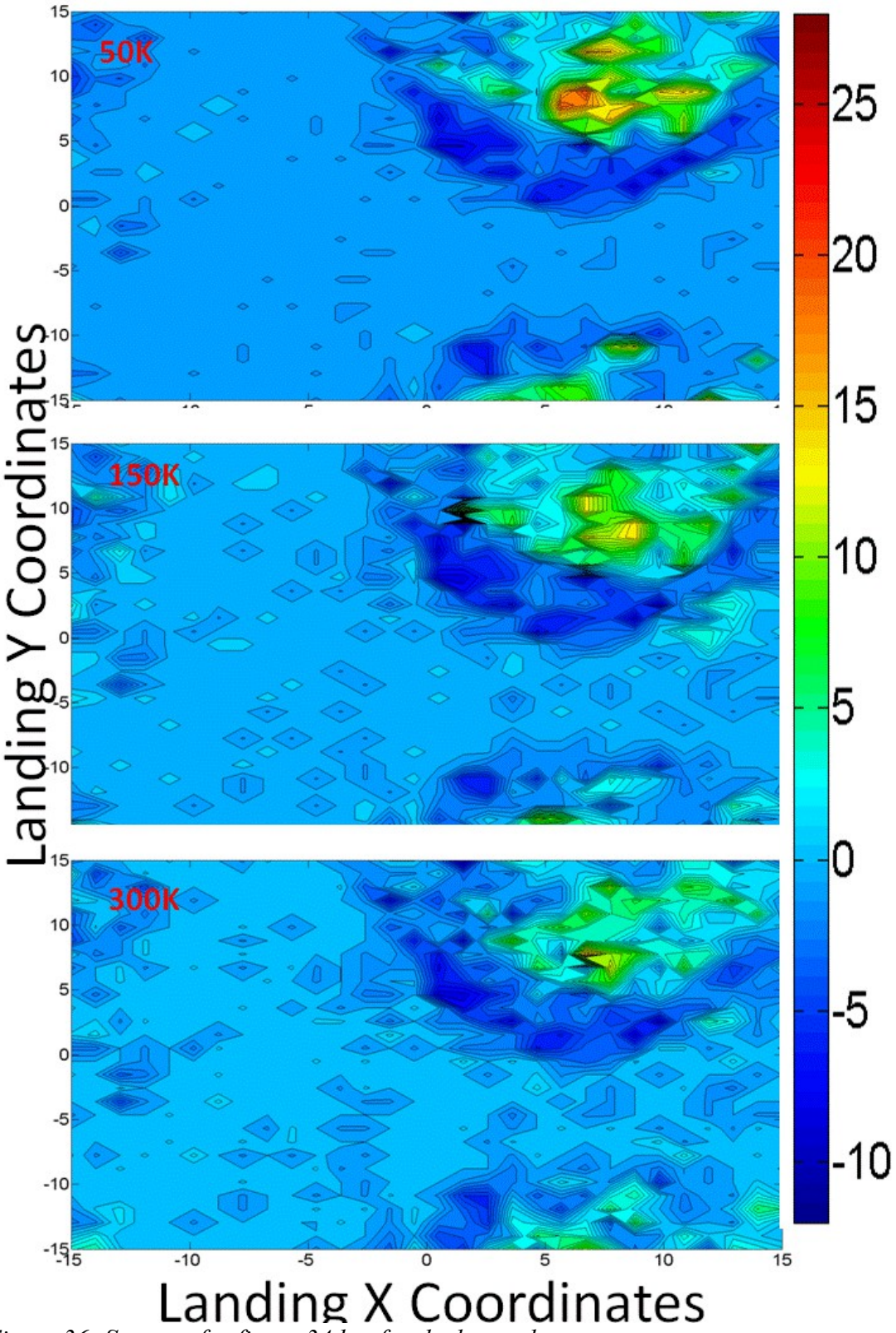

Figure 36: Same as for figure 34 but for the large cluster

Figure 35 Shows that there is a concentration of landing coordinates around (-7,-12), (5, 3) and (3.5, -5). Once again these correspond to landing cluster concentrations as seen in Figure 31 B, C and D. This is consistent with Figure 29 in section 5.2.3 for the hydrophobic substrate. Likewise, we can also see that electro-steering is deposition temperature dependent as for the previous substrate, as landing coordinates are more concentrated around the above coordinates for lower deposition temperatures. When comparing Figure 35 at 50, 150 and 300K for the landing coordinates (-7,-12) and (5, 3) respectively, it can be seen that these landing coordinates become less dominant for higher deposition temperatures. As with the previous substrate this implies that incoming water molecules with more kinetic energy will overcome steering towards the most energetically favourable site in favour of another site, and thus also explains why ASW structures grown at lower deposition temperatures are taller than those grown at higher deposition temperatures.

Figure 36 Shows that there is a concentration of landing coordinates around (5,7), (6.5,10) and (8,10) meaning that incoming water molecules are being steered towards ASW peaks. Once again we can also see that electro-steering is dependent on deposition temperature as these landing coordinates become less dominant for higher deposition temperatures. Again, Figure 35 and Figure 36 both show a negative landing coordinate ring (a dark blue ring) located around ASW peaks. This can also be see in the previous simulations in Figure 29 and Figure 30. This is because these contour plots have shadowing coordinates subtracted.

5.4 Investigating Shadowing around simple shapes

The penultimate batch of simulations looks at the effects of shadowing on simple shapes, the purpose of these simulations are to act as a control against previous simulations and to further reinforce that steering is the dominant driver for ASW growth. As with simulations performed in batches 3 and 4 (see chapter introduction 5.) these simulations are ballistic and follow the same deposition algorithm albeit with different substrates. Both substrates consist of a lennard-Jones 30x30 single layer lattice with a hemisphere and cylinder in the centre of this substrate imitating a small and large

ASW cluster. The pre and post deposition figures can be seen in Figure 37 and Figure 38below.

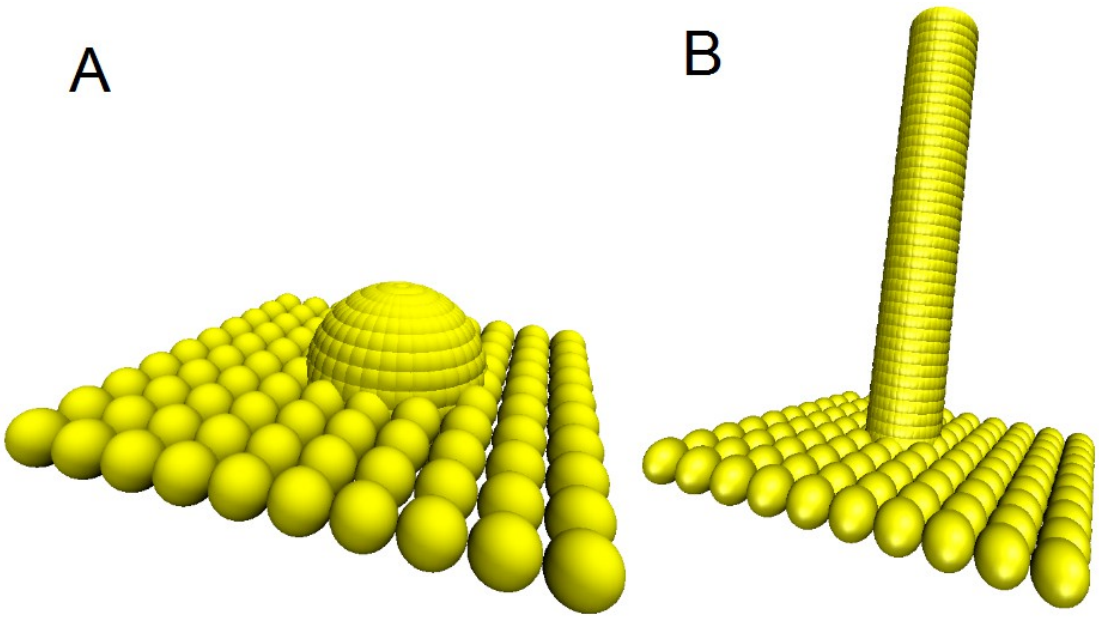

Figure 37: Illustrating the hemispherical and cylindrical shapes A and B respectively on a Lennard Jones substrate

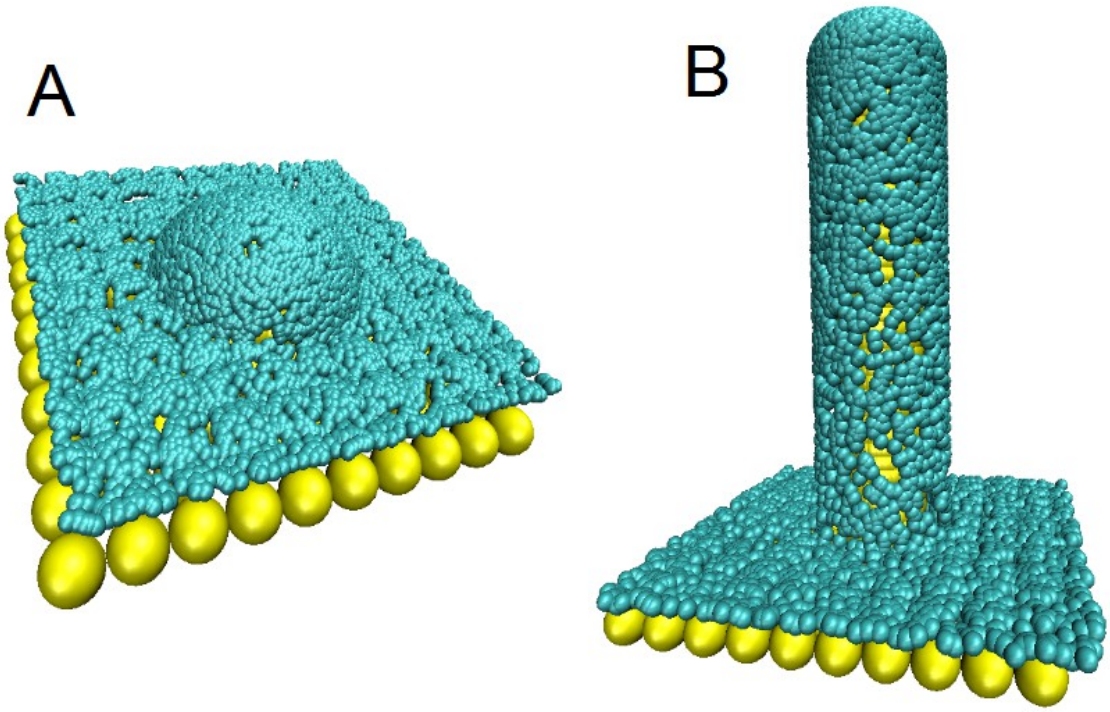

Figure 38: This figure shows the landing coordinates for a hemispherical and cylindrical substrate A and B respectively. There appears to be a uniform distribution of landing coordinates which implies that shadowing effects are not evident for small hemispherical structures.

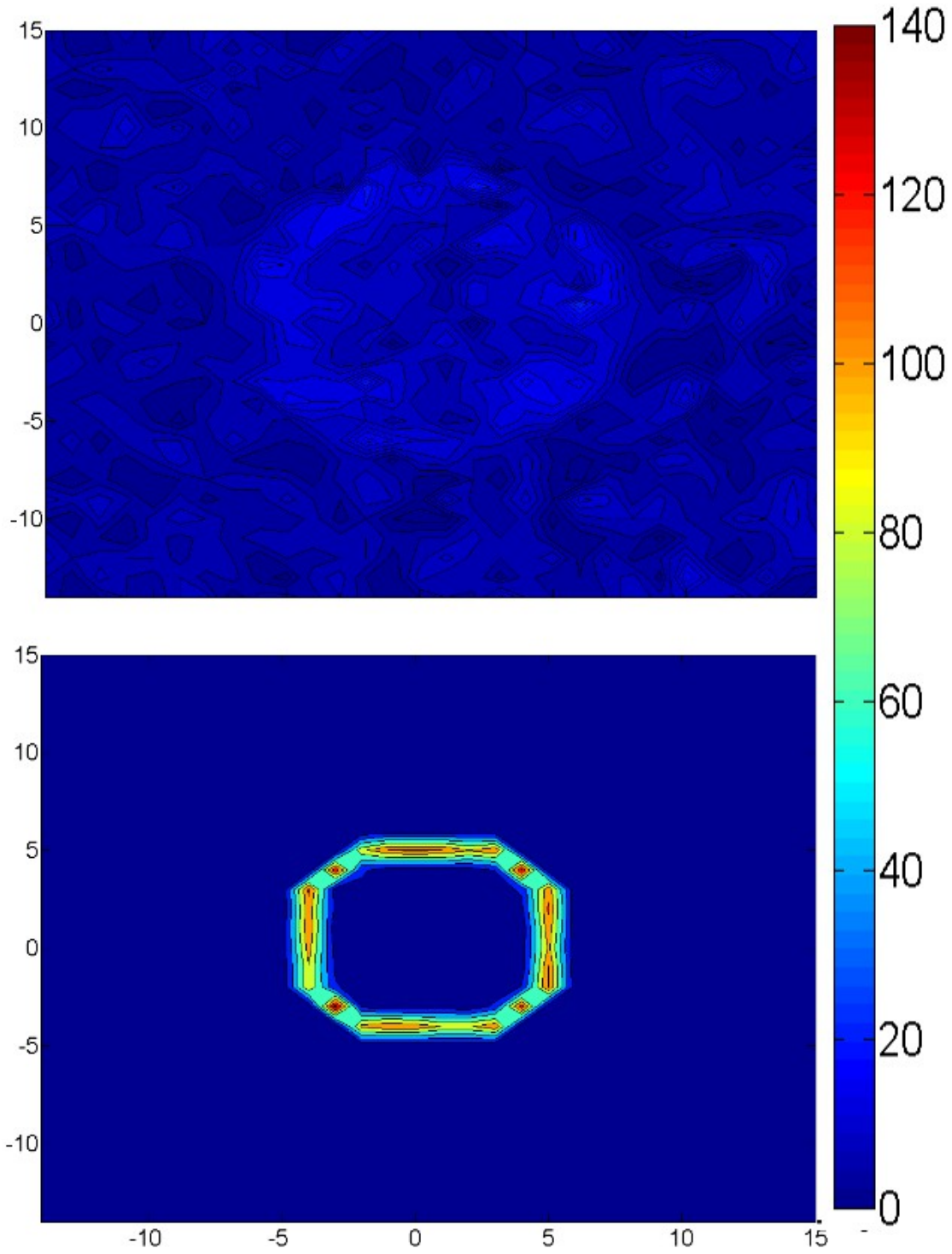

Figure 39: This figure shows the contour plot for landing sites on a hemispherical and cylindrical substrate, top and bottom respectively. It can be seen that there is a more uniform distribution of landing sites for a hemispherical than cylindrical substrate. This is because of a large number of landing sites on the side of the cylindrical surface.

Figure 38 and Figure 39 above clearly shows that shadowing is not that significant for small hemispherical clusters but is more important for cylindrical structures as more deposition landing sites are found on the cylinder surface than the base substrate. Relating this back to ASW structures we can see in Figure 25, Figure 26, Figure 31 and Figure 32 that small ASW clusters have a uniform distribution of landing sites for ballistic simulations (which is section A for all these figures), Comparing Figure 38 and section A against B, C, D of Figure 25, Figure 26, Figure 31 and Figure 32 it appears that electro-steering is having more of a dominant effect on landing sites and subsequent ASW formation that shadowing. This is also true for large clusters, if you compare Figure 38 and section A against B, C, D of Figure 27, Figure 28, Figure 33 and Figure 34, it would appear that there are a larger number of landing sites concentrated at the tips of B, C, and D of Figure 27, Figure 28, Figure 33 and Figure 34 than in section A and Figure 38 which show landing sites uniformly spread on the surface of the cylinder and ASW tendril.

5.5 Correlation between Landing sites and Dangling Hydrogen bonds

In the previous section when comparing contour plots (Figure 29, Figure 30, Figure 35 and Figure 36) against landing coordinate diagrams (Figure 25, Figure 26, Figure 31, Figure 32, Figure 27, Figure 28, Figure 33 and Figure 34) there appears to be a correlation between dangling hydrogen bonds and a higher density of landing sites around them, implying that incoming water molecules are being steered towards dangling hydrogen bonds. In order to investigate this another batch of simulations were ran to work out where the dangling hydrogen bonds were for each ASW structure using the same energetic and geometric criteria as outlined in section 4.1, for a small and large cluster for both substrates (four in total). By comparing a list of dangling hydrogen bonds to the corresponding landing sites it is possible to see if incoming water molecules are being steered towards dangling hydrogens for a given ASW structure. Figure 40, Figure 41, Figure 42 and Figure 43 below show the dangling H-Bond to landing site coordinates correlation.

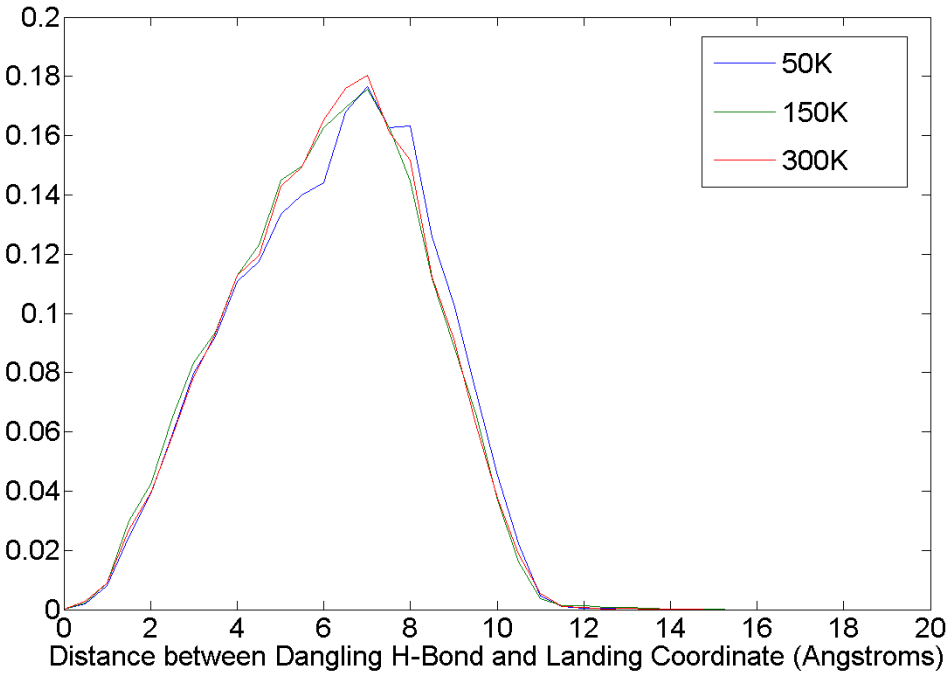

Figure 40: Shows the Dangling H-Bond to landing coordinate correlation for a hydrophobic substrate with a small ASW cluster

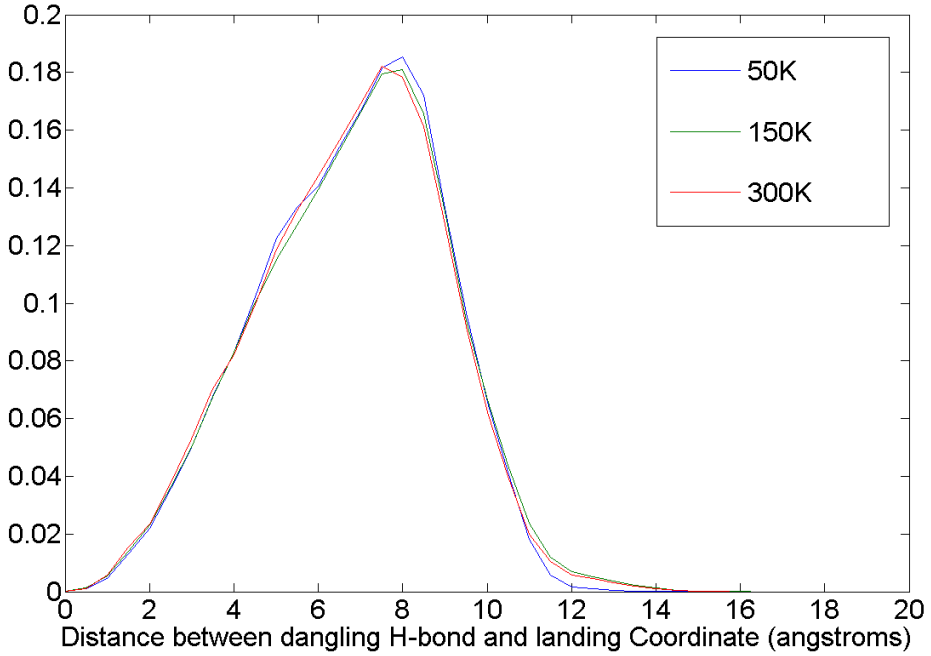

Figure 41: Shows the Dangling H-Bond to landing coordinate correlation for a hydrophilic substrate with a small ASW cluster

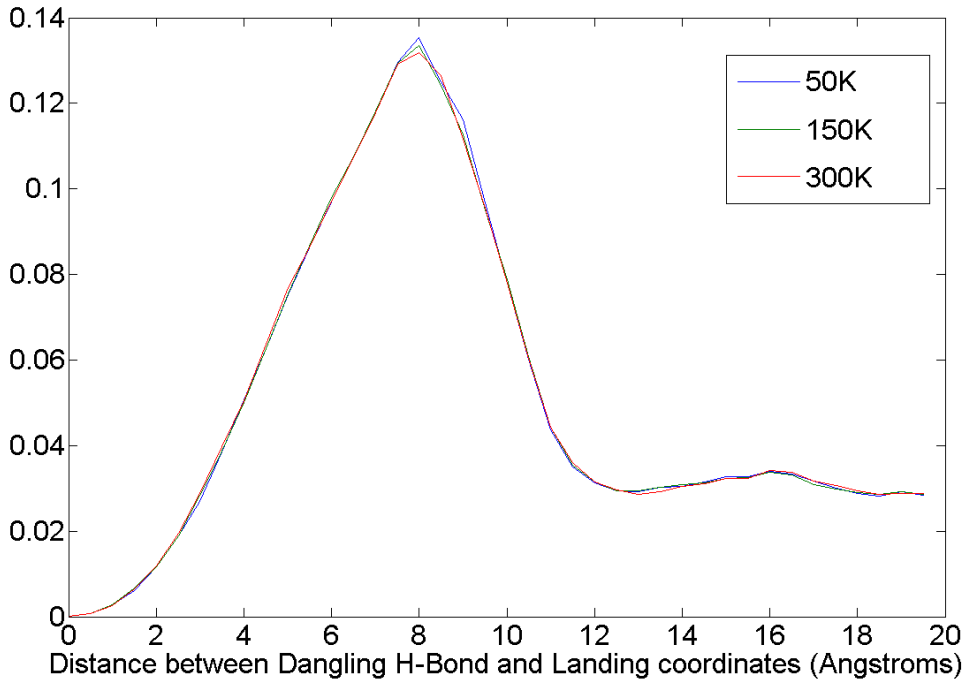

Figure 42: Shows the Dangling H-Bond to landing coordinate correlation for a hydrophobic substrate with a large ASW cluster

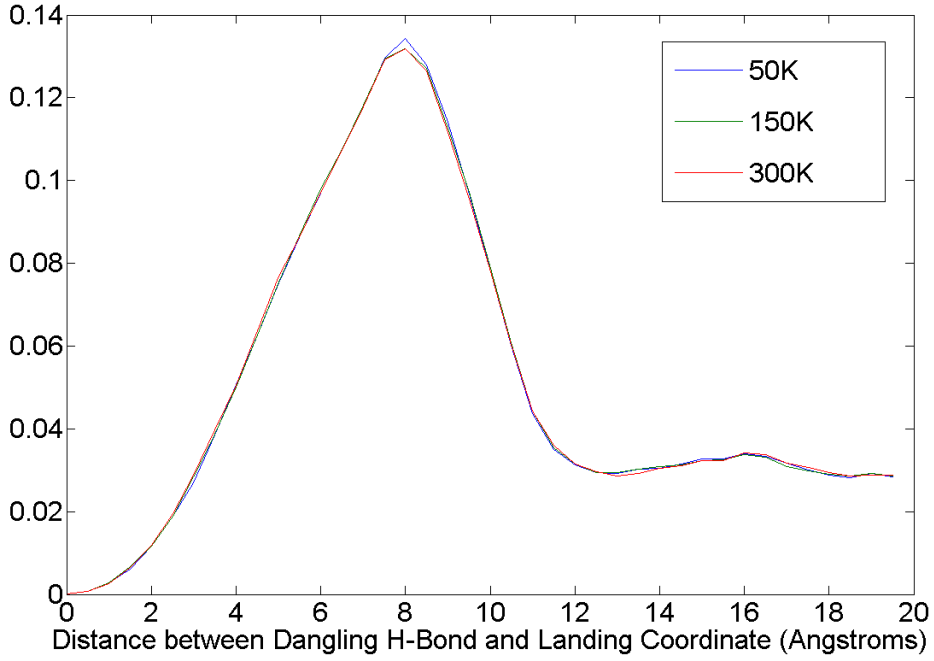

Figure 43: Shows the Dangling H-Bond to landing coordinate correlation for a hydrophilic substrate with a large ASW cluster

In all cases there is correlation peak between 6 – 8 angstroms signifying that most incoming water molecules are being steered towards dangling hydrogen bond sites, this explains why there is such a high density of landing sites for dangling H-Bonds when visually comparing contour plots (Figure 29, Figure 30, Figure 35 and Figure 36) against landing coordinate diagrams (Figure 25, Figure 26, Figure 31, Figure 32, Figure 27, Figure 28, Figure 33 and Figure 34). These results show that electrosteering is slightly more dominant for small clusters than large ones, Figure 42 and Figure 43 show that there is a greater correlation between deposition temperature and electrosteering, this inverse relationship is also consistent with sections 5.2.3 and 5.3.3.

5.6 Quantifying Electro Steering for ASW Structures

The last batch of simulations attempts to quantify steering through the use of 2D force maps, the purpose of these simulations is to quantify steering forces and by mow much incoming water molecules will be deviated towards O-H dangling hydrogen bonds.

These simulations are performed in two stages using a discovery and optimization algorithm. The discovery algorithm will traverse the simulation cell volume in all three directions generating a 1 x 1 x 1 Angstroms mesh, a point on this mesh is classed as a vacant point in space if there are no ASW water molecules within 3.5 angstroms. This produces an array of x, y, z coordinates which are in free space within the simulation cell.

The second phase of this simulation is where a water molecule is inserted into the free space coordinates and the algorithm loops through all orientations to find the strongest attractive force. The results are shown in 2D force maps below.

5.6.1 Hydrophobic Substrate

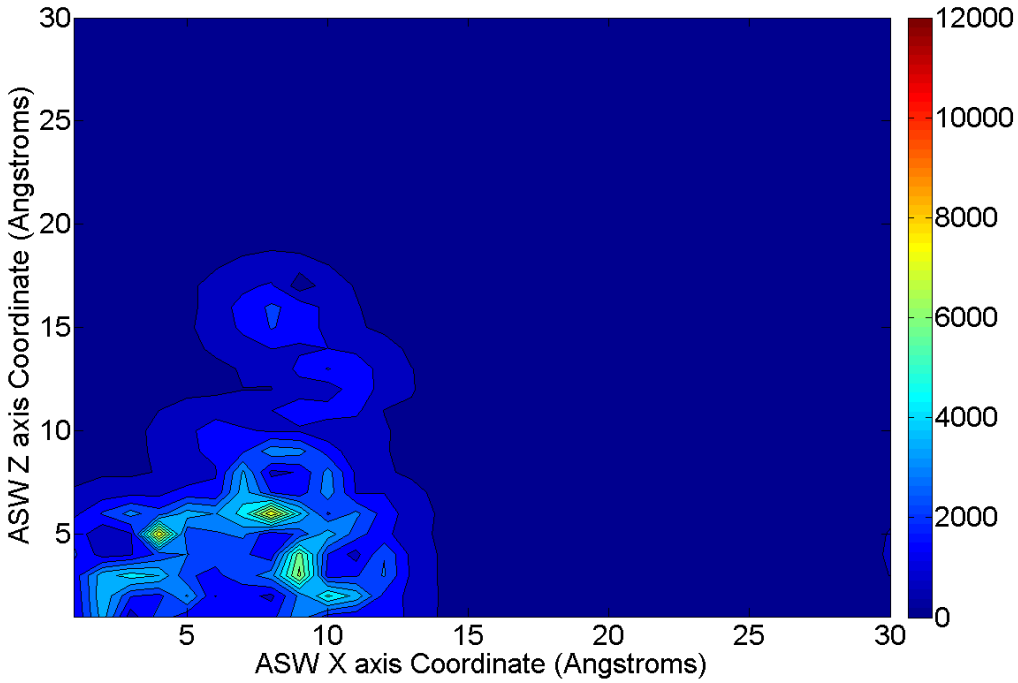

Figure 44: This Forcemap is for a small ASW cluster where 100 water molcules have been deposited onto a hydrophobic substrate. The colour bar measures molecular acceleration (in Angstroms/picosecond^2)

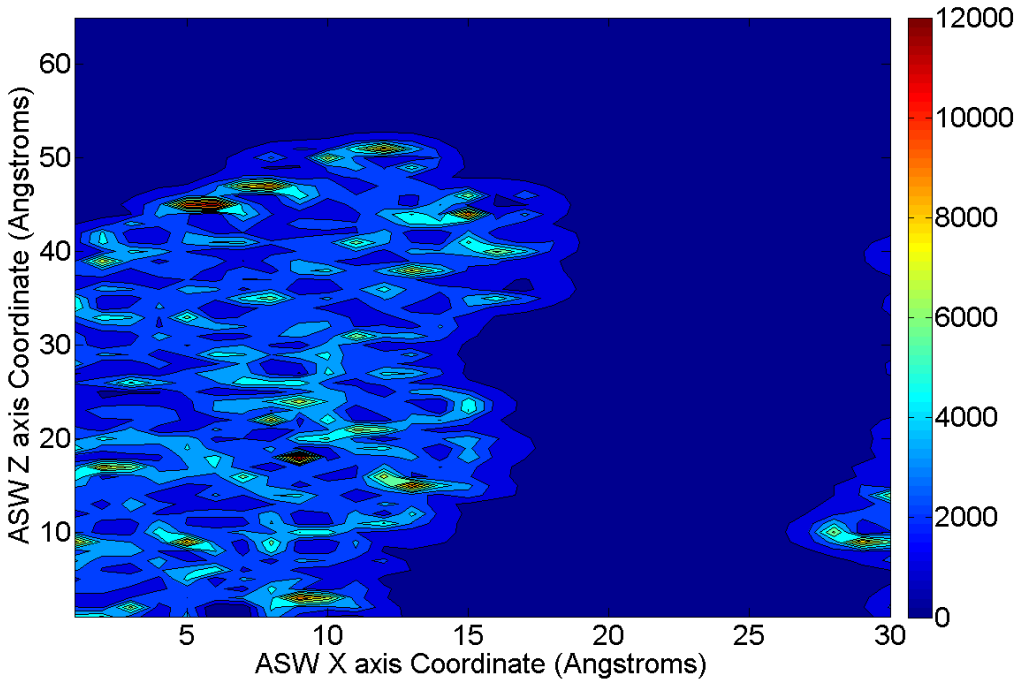

Figure 45: This is the 2D force map for a large ASW cluster where 450 water molecules have been deposited onto a hydrophobic substrate. The colour bar measures molecular acceleration (in Angstroms/picosecond^2)

Comparing Figure 44 and Figure 45 it appears that steering is more dominant for larger ASW clusters than for small ones, incoming molecules are defected by as much as 12000 Angstroms/picosecond^2. Figure 45 Shows that incoming water molecules will be subject to a strong attractive force at ASW tips corresponding to x, z coordinates (6,45), (7,47), (12.5,50) and (15,43). Max accelerations experienced for the small cluster is around 8000 Angstroms/picosecond^2 which is still considerable.

5.6.2 Hydrophilic substrate

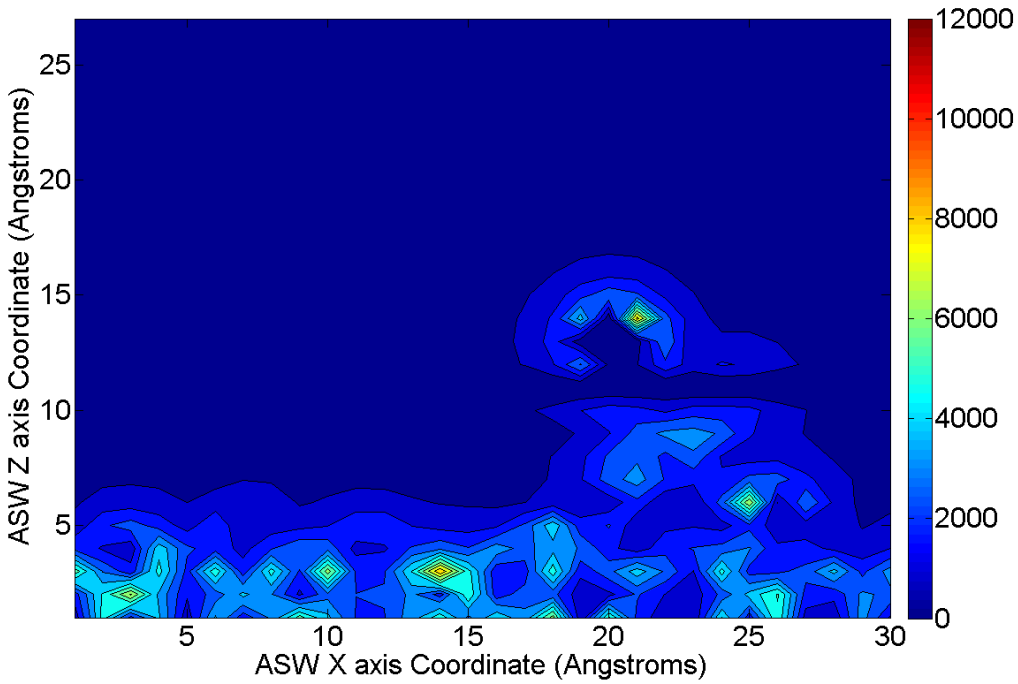

Figure 46: This Forcemap is for a small ASW cluster where 100 water molecules have been deposited onto a hydrophilic substrate. The colour bar measures molecular acceleration (in Angstroms/picosecond2)

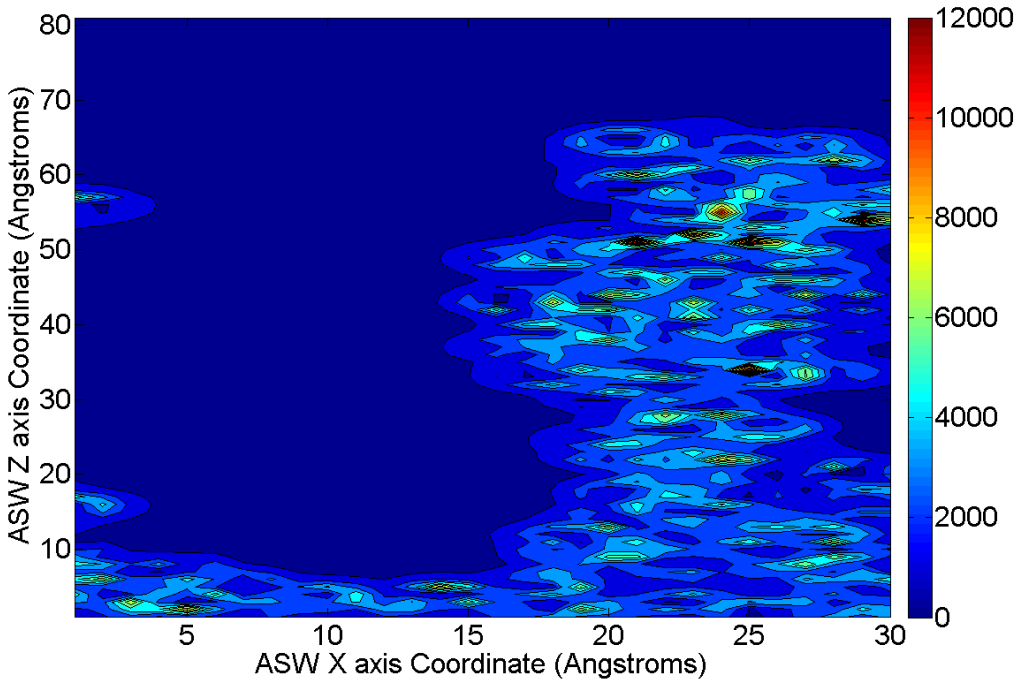

Figure 47: This Forcemap is for a large ASW cluster where 450 water molecules have been deposited onto a hydrophilic substrate. The colour bar measures molecular acceleration (in Angstroms/picosecond2)

Once again comparing Figure 46 and Figure 47 it would appear that steering is more dominant for larger ASW clusters where incoming water molecules are subject to 12000 Angstroms/picosecond^2 accelerations from their initial trajectories. Also we can also observe that incoming molecules are being steered towards ASW tips corresponding to x, z coordinates (21, 52), (22.5, 53), (25,52) and (28,55). Interesting when comparing the two small clusters (Figure 44 and Figure 46) steering forces are stronger for the hydrophilic substrate than for the hydrophobic one, this is because incoming water molecules are being steered towards the cubic ice substrate which does not happen for the hydrophobic substrate. Consequently, this further reinforces the fact that water molecules are more evenly distributed for hydrophilic than hydrophobic substrates.

In summary, steering can alter the trajectory of incoming water molecules by as much as 8000 to 12000 Angstroms/picosecond^2 with steering being more dominant for larger ASW structures where they appear to being steered towards the ASW tips. These results

further reinforce sections 5.4 and 5.5 that steering does play a significant part in ASW growth both at the nucleation and coral formation stage.

5.7 ASW growth on hydrophilic and hydrophobic substrates

These results show how ASW forms on hydrophilic and hydrophobic substrates.

- During the initial deposition stage an ASW nucleus forms on both substrates. It seems likely that such a cluster nucleus would form more quickly on the hydrophobic substrate due to competing long-range electrostatic interactions with the hydrophilic substrate. Moreover, it is conceivable that if an incoming water molecule misses the putative ASW cluster and adsorbs onto the hydrophobic substrate then long range attractive forces between this deposited water molecule and the ASW cluster are such that the deposited molecule could diffuse towards the ASW cluster and adsorb onto it. However, these effects have not been examined directly in this thesis. Nevertheless, this work has established that steering becomes increasingly influential with decreasing deposition temperature, and so an ASW nucleus will form more quickly at lower deposition temperatures. The results above show that this nucleation process is driven by steering for both substrates.

- Once ASW clusters on both substrates have matured into small coral-like structures, electro-steering further exacerbates this coral-like growth forming taller ASW columns, with incoming water molecules being steered towards dangling O-H bonds (as outlined in sections 5.2.3,5.3.3,5.5and 5.7). Incoming water molecules with less momentum (lower deposition temperatures) will experience greater deviations from their original trajectories than ones with more momentum. Consequently, at lower deposition temperatures incoming water molecules will be steered locally to the most energetically favourable hydrogen bonding site of the ASW structure. This explains why ASW coral-like structures are taller for lower deposition temperatures and why, apart from the initial nucleation stage, the substrate appears to have little effect.

- The ballistic simulations (Figure 25A, Figure 26A, Figure 31A and Figure 32A) for both substrates and both clusters demonstrate that shadowing in isolation has less impact on ASW formation. Indeed, shadowing on its own would tend to produce more lateral growth and hence shorter, less porous structures. This feature is clearly illustrated by the negative regions, or the "dark blue rings", for both sets of contour plots in Figure 29, Figure 30, Figure 35 and Figure 36 which show that even for large ASW clusters steering is much more dominant that shadowing. Essentially, nearly all depositing water molecules, at all the temperatures simulated and for both substrate types, are deflected towards the top of ASW filaments before the geometric effect of shadowing has the opportunity to have any effect.

In summary, long-range electrosteering dominates ASW structure, through both the nucleation and growth stages. Consequently, substrate type influences the nucleation stage, but has little effect on further growth. On the other hand, as electorsteering is influenced by temperature, ASW nucleation, growth and structure are influenced by deposition temperature, with lower temperatures resulting in taller, more filamentous structures. Importantly, shadowing has little influence on ASW growth, as this geometric effect rarely has the opportunity to have any effect.

6. Conclusion and Future Work

6.1 Implications of highly filamentous ASW structures

The previous chapter illustrates how electrosteering dominates ASW nucleation, growth and structure. Currently, in the astrochemical community it is thought that ASW is dominated by shadowing effects such as those reported by kimmel[70] et al. This study shows that shadowing has very little to no effect on ASW formation and structure at any stage, either during nucleation or growth, as detailed in section 5.7 above, and to the best of my knowledge no previous study has even considered electrosteering as a factor for ASW formation prior to this study. Sections 5.2.1 to 5.2.3 and 5.3.1 to 5.7 show that electrosteering becomes increasingly dominant with decreasing water deposition temperature, as incoming molecules with higher deposition temperatures will possess greater kinetic energy and therefore are able to overcome steering forces.

Figure 25, Figure 26, Figure 27 and Figure 28 show that incoming water molecules are steered towards dangling hydrogen bonds. This is important for the ASW growth stage as increasing the number of hydrogen bonds increases the structural integrity of ASW filaments and allows them to grow even taller than they would without electrosteering. Without electrosteering, the balistic simulations show that ASW growth would be greater in lateral directions producing less porous structures. It is therefore electrosteering that is responsible for the more porous ASW structures found in this study. This is the first study to demonstrate this effect. Earlier molecular dynamics studies of ASW formation could not reveal this effect for several reasons, notably their use of small cutoff radii and low deposition heights, as shown in Table 8 below.

Moreover, many previous simulation studies did not accurately simulate the deposition process, and instead sometimes reported over heating during simulations because the deposition rate was too high, compared with experimental studies and astrophysical conditions. This study has managed to overcome this issue by employing a multi-stage deposition process that attempts to accurately reproduce each deposition event. An important feature is the use of randomly oriented initial deposition trajectories, the

decision not to 'thermostat' the ASW during the deposition stage, and the use of a hyperquenching phase between each deposition, as outlined in section 3.6. This strategy is important, as it allows 'impact annealing' to be accurately simulated during each deposition event. Impact annealing increases the number of hydrogen bonds and enables localised molecular restructuring. Although these annealing effects also occur in unrealistic simulations that overheat, in those simulations this annealing process is not properly reproduced and hence the resulting structures, similar to HDA and LDA ice, are also unrealistic. The only other study to use a similar strategy is that of Wilson, but as shown in the table below, their deposition height is much lower, and they used a smaller system and did not attempt to understand the deposition process in terms of shadowing and electrosteering.

Finally, sections 5.2.3 and 5.3.3 show that surface morphology is only important during the nucleation phase, when depositing water molecules will be steered much more towards the nucleating ASW cluster than the substrate when the substrate is hydrophobic. In contrast, incoming water molecules are steered towards both the substrate and ASW cluster for a hydrophilic substrate. This is important from an astrophysical point of view as current understanding states that ISM dust gains are either silica (hydrophilic) or graphite (hydrophobic) in nature as outlined in section 1.2.2. This study has found that once nucleation has occurred, further growth and the structure of ASW does not depend on the substrate type, and the deposited ASW dominates further growth through electro-steering.

	Initial deposition height above ASW surface. (Angstroms)
This study	14
Essmann and Geiger	8.5
Buch	10
Guillot and Guissani	3
Wilson	8

Table 8: Table showing the heights at which incoming water molecules were deposited above the ASW ice film. The higher the deposition height the more electrosteering will be experienced.

As mentioned in the introduction chapter (1), ASW has been studied using both experimental and computer simulation techniques which are covered in sections 1.4 and 1.5 respectively. All previous computational studies have overestimated the ASW bulk phase density, with Guillot and Guissani[71,72]; Essmann and Geiger[69]; and Wilson et al.[68] reporting values of 1.1, 0.94 to 1.1, and 0.9 g/cm^3 respectively (as shown in Table 9 below). This is considerably higher than the 0.85 to 0.9 g/cm^3 found in this study. Furthermore, experimental studies have also overestimated ASW bulk density with P. Ehrenfreund, H. J. Fraser et al.[8] reporting an ASW bulk density of 1.1g/cm^3. This is due to experimental deposition rates far exceeding the ISM deposition rates and that of this study (by two orders of magnitude) as shown in Table 5. This also explains why experimental studies such as Jenniskens[7], Jenniskens and McCoustra[21], Fraser and McCoustra[29] report Cryostat overheating. The overheating issue introduces unrealistic annealing producing more squatter ASW structures, thus increasing the ASW bulk density. Another reason why experimental studies have higher ASW bulk densities, than this study, is that incoming water molecules are being deposited at room temperature via 'background deposition' (a process where water vapour is being deposited onto a surface rather than one molecule at a time) this raises several issues in light of the electrosteering anomaly found in this study.

- How do water molecules within this vapour interact with each other prior to being deposited on the substrate?
- How accurate is the initial deposition angle with respect to the surface normal given that incoming water molecules are steering towards and away from each other?
- Are water vapour molecules forming hydrogen bonds and consequently water clusters prior to deposition? If so by how much? Larger clusters will possess more momentum and therefore more likely to overcome the effects of electrosteering thus producing more dense ASW structures.

Interestingly, Kimmel et al. is the only experimental ASW study to use molecular

beams rather than a 'background deposition' deposition method, where individual water molecules are deposited onto a Pt(111) substrate at 22K using large deposition angles, this experimental study is more consistent with both ISM conditions and with this study. Furthermore, this study reports an ASW bulk density of 0.87 g/cm^{-3} which agrees well with this study as shown in the Table 9 below. This means that all previous simulation and experimental studies with the exception of kimmel et al.[70,86] have produced more condensed ASW structures than the ones found in this study.

This is important as previous experimental studies have reported ASW surface areas of 2700 and 4000 m^2/g[3,86] (kimmel et al. and P. Ehrenfreund, H. J. Fraser et al. respectively) even with comparatively more dense ASW structures than this study. This suggests that the surface area of ASW may be even larger than previously thought.

	No. Hydrogen Bonds per water molecule			Density		
	Bulk	Interfacial	Average	Bulk	Interfacial	Average
This study	3.85	3.7	3.78	0.85-0.9	0.25-0.3	0.85
Essmann and Geiger	3.75	3.4	3.575	0.94-1.1	0.55	0.94
Buch	3.72	2.45	3.085	-	-	-
Guillot and Guissani	-	-	-	1.1	-	1.1
Wilson	-	-	-	0.9	0.6	0.9
Kimmel	-	-	-	-	-	0.87

Table 9: This table compares the results obtain during this study with other computer simulation studies of ASW. It can be seen that this study provides the first comprehensive view of ASW structural properties. Note that previous studies have overestimated ASW density (bulk, interfacial and average) and underestimated the number of hydrogen bonds per water molecule.

6.1.1 Consequences for ASW Catalysis

Current astrochemical literature cannot account for the abundance of molecular hydrogen, and it is generally believed[3], that this occurs through surface chemistry on ASW icy mantles either by Eley-Ridal or Langmuir-Hinshelwood mechanisms. If ASW

has a much larger surface area and therefore a greater number of dangling hydrogen bonds than previously thought, this could a have profound impact on molecular hydrogen formation in the universe and would also go some way in explaining the chemical abundance of other more complex ISM molecules[17] as described in section 1.2.4 for the following reasons.

- Larger ASW surface areas will assist the Langmuir-Hinshelwood mechanism of surface chemistry as there is larger surface for reactants to physorb and react via surface diffusion.
- A greater number of dangling hydrogen bonds will assist the Eley-Ridal mechanism of surface chemistry as these dangling hydrogen atoms will provide specific surface sites to catalyse reactions for more complex ISM molecules.

This study shows that ASW is maybe a more powerful ISM catalyst than previously thought.

ASW desorption kinetics are of astrochemical importance as it describes the relationship between surface chemistry and gas phase abundance in molecular clouds. Molecular hydrogen is pivotal in star formation acting as a cooling mechanism during gravitation collapse; likewise CO also acts as a coolant for molecular clouds, shielding them from high energy photons and particles. Work by McCoustra et al, Ayotte et al.[87], Horimoto, Kato and Kawai[88] has investigated the desorption kinetics of space borne gas species such as H2, CO, CO2, N2, O2 and CH3OH and found that the molecular species similar to water, such as CH3OH, NH3 and HCOOH (in the sense that they are dominated by hydrogen bonding), desorb at higher temperatures due to hydrogen bonding interactions with water ice, whereas non hydrogen bonding species such as CO, N2, O2, NO and CH4 desorb at much lower temperatures between 30 – 90K. This desorption process of non water-like species is often referred to as 'the volcano effect' and explains the gas phase abundance[16,17] of these molecular types in current literature.

This study shows that ASW is much more porous with more accessible dangling hydrogen bonds than previously thought. This means that CO, O2, N2, NO and CH4 can penetrate deeper into ASW structures. This is important as currently literature[30]

suggest that icy mantles have much more compact structures meaning that gas species are trapped beneath layers of ice. If ASW is more porous the 'freeze out' and 'molecular volcano' effects (condensation and sublimation respectively) are much less restricted than previously thought as:

- Gas phase reactants can penetrate deeper in ASW pores increasing their abundance in an icy mantle. This should enhance Langmuir-Hinshelwood surface chemistry.
- Deeper pores with larger pore wall surface area will allow better inter-diffusion of various gas species and further enhance surface chemistry mechanisms.

6.1.2 Consequences for ASW icy mantle grain Aggregation

The process of dust grain aggregation has been investigated by Fraser and Salter[9]. As described in section 1.1, bare and icy dust grains are accelerated towards an icy target with a velocity, mass and length range of about 0.03 to 0.28m/s, 0.01 to 0.03 grams and 0.2 to 6 mm respectively. Dust grains used in this experiment were composed of 1.5 nanometers monodispersed monomer SiO2 spheres which are 85% porous, and the icy mantle was hexagonal ice. This study reports that only 10% of the icy dust grain target collisions resulted in sticking, and concludes that the experiment could be improved if the UHV chamber maintained cryogenic temperatures which more closely resembles protoplanetary conditions < 80K. The study also reports that the sticking probability of icy dust grains would increase greatly if the icy mantles were replaced with ASW rather than hexagonal crystalline structures. This study concludes that icy dust grain aggregation, and consequent planet formation, is governed by several factors including: fragmentation, mass exchange and compaction behaviour.

Although this study does not investigate sticking probabilities of icy dust grain aggregation, it is clear that ASW with its more porous and amorphous structure will be more conducive to icy dust grain aggregation than hexagonal crystalline ice for the following reasons:

- Fragmentation, mass exchange and compaction behaviour are all manifestations

of the same issue regarding ASW structure. In order for aggregation to occur icy dust grains must effectively dissipate impact energy from collisions. It is very difficult to dissipate impact energy when the icy mantle is composed of a hexagonal crystalline structure. This is in sheer contrast to ASW which is a metastable structure that can dissipate impact energy by breaking hydrogen bonds through molecular re-structuring or shattering of ASW structures. Essentially, ASW can convert collision impact energy into molecular potential energy much more easily than a crystalline or compact amorphous ice structure.

- Furthermore, in light of this study, ASW has a fluffy, coral-like structure with even larger surface area and more dangling hydrogen bonds than previously thought (> 4000 m^2/g and 3.78 hydrogen bonds per water molecule as described in section 6.1.1 above), meaning that 1 out of every 16 hydrogen bonds is dangling in this highly porous ASW structure. This is important for icy dust grain aggregation as the interfacial ASW region on colliding dust grains will have dangling hydrogen bonds which during collisions will form new hydrogen bonds between the interfacial ASW regions on both icy dust grain mantles. Moreover, as ASW strands fracture and re-structure during collisions, new dangling OH bonds will be formed. Therefore, ASW not only acts as a structure for dissipating impact energy but also acts as a 'glue' binding icy dust grains together. These h-bond forming processes are much less likely with crystalline or compact amorphous ices.
- Lastly, ASW can convert impact energy into thermal or potential energy more readily than for a crystalline structure for two reasons. Firstly, ASW pore collapse could act as a 'cushion' during the collision process allowing thermally excited ASW molecules to dissipate energy via radiation or excited modes (vibration, rotation or translational motion); and secondly, ASW is not as stable or mechanically rigid as crystalline ice and consequently will sublimate easier allowing more collision energy to be converted to chemical potential energy.

The thesis objective and outline section (1.6) in the introduction chapter outlines the

thesis objectives. Chapters 4 and 5 indicate that ASW morphology is highly porous and amorphous with deposition temperature affecting ASW structure. These chapters also show how ASW nucleation and growth occurs on different substrates, with section 5.7 indicating that substrate type is only important during the nucleation phase where nucleation occurs more quickly on a hydrophobic than hydrophilic substrate.

PVD ASW growth (nucleation development and coral-like growth) is driven by electro-steering, a process whereby incoming molecules are steered primarily towards dangling O-H bonds (see sections 5.2 and 5.3and figures Figure 25 to Figure 36). Consequently, there are not many dangling O-H bonds in our ASW structures. This is also shown in Figure 21 and Figure 22 which suggest that there are on average 3.78 hydrogen bonds per water molecule. Interestingly the number of hydrogen bonds per water molecule is 3.85 in the bulk phase region (the region closer, but not right next to the substrate), and decays to 3.7 in the interfacial region, creating a strong tetrahedral hydrogen bonding network which provides greater structural integrity of ASW corals. Figure 21 and Figure 22 show that the number of hydrogen bonds per water molecule is not affected by deposition temperature or substrate morphology.

There is evidence of molecular layer packing in the ASW region adjacent to the substrate for both substrates (as shown in Figure 19 and Figure 20) depicted by a sharp step-wise increase in density at 7 and 9 angstroms above the substrate. It was also found that substrate type affects ASW density as a function of height above the substrate. ASW densities close to the substrate were found to peak at 0.8 and 1.2 g/cm^3 for the hydrophobic and hydrophilic substrates respectively. This can be explained using results from chapter 5 which show that incoming water molecules are steered more towards an ASW cluster for a hydrophobic than hydrophilic substrate. Therefore one would expect to see a larger density closer to the substrate for a hydrophilic than hydrophobic substrate. The fact that incoming water molecules are more dispersed on the hydrophilic substrate also explains why ASW corals are taller for a hydrophobic than hydrophilic substrate. Interestingly it was also found that increasing the deposition temperature increased ASW densities closer to the substrate and also produced ASW coral-like structures which were not as tall as for lower deposition temperatures (see

Figure 17 and Figure 18); this is due to localised impact annealing which is greater for higher deposition temperatures (see the results 4section).

6.2 Astrophysical implications

As mentioned in the introduction chapter (1), space borne dust grains are either graphitic or siliceous in nature. This means that the surfaces of these dust grains will be hydrophilic or hydrophobic for silica and graphite dust grains respectively. Water molecules are deposited onto these dust grains in the protostellar phase of star formation by physical vapour deposition (PVD) producing icy dust grains, as simulated by our MD simulation for this and the previous chapter. The Electro-steering results from this chapter indicate that the initial nucleation process is different for these dust grains, where water clusters form more rapidly on graphitic dust grains than for silica ones. However, when an ASW water cluster forms on either substrate the subsequent ASW formation process is practically the same for both dust grains.

Both dust grains will produce ASW coral-like structures which are heavily dependent on Electro-steering. Furthermore, these results also show that there is a deposition temperature dependence on Electro-steering; that is, incoming water molecules which have lower deposition temperatures (momentum) will be subject to greater levels of steering and therefore will deviate more from their initial trajectory and hydrogen bond in the most energetically favourable position within/on the ASW structure. This also explains why in the last chapter ASW coral-like structures were taller for lower rather than higher deposition temperatures, as incoming molecules with lower deposition temperatures increase the structural integrity of this coral-like ASW structure by hydrogen bonding to the most energetically favourable bonding site.

6.2.1 Implications for Planet, Asteroid and Comet formation

These results suggest that icy dust grains which are grown in colder areas of the protostellar disk will have a more amorphous and porous coral-like structure than those grown in warmer areas. This implies that the initial icy dust grain aggregation which

results in planet and asteroid formation will occur in the outer layers of the protostellar disk as icy mantles are more porous and capable of dissipating impact energy incurred during the aggregation process. This explains why planets, asteroids and comets form further out in the equatorial mid-plane as described in section 1.2.7, formation cannot occur too close to a forming star as radiative thermal energy sublimates icy mantles preventing the aggregation process. In addition to this, using this analogy comets should form on the outer layers of the protostellar disk which reinforces popular theory[3].

6.3 Possible Future Work

This thesis has revealed a suitable strategy for performing PVD simulations of ASW nucleation and growth, and for examining the resulting structures. However, there are still some areas for improvement.

6.3.1 Improved models

First, the conclusions of this work rest largely on the discovery that long-range interactions between water molecules are important for ASW nucleation and growth, and the resulting structures and properties. The implication of this is that in future, simulation strategies should be more careful to properly capture these effects. It is particularly important to note that it is not enough to have an accurate representation of short-range water-water interactions that lead to hydrogen bonding. These kinds of interaction are modelled rather well by many popular water models in the literature, at least at ambient conditions. So it is suggested here that future work should look at the following issues;

- The short range representation of hydrogen-bonding in water molecules at very low temperature. We have neglected quantum effects in this work for convenience, but as shown in section 3.4 quantum dispersion might be significant for the hydrogen atoms in water at such low temperatures as well as quantum rotational effects due to a water molecules low moment of inertia.
- The long range interaction of water molecules, which is shown in this thesis to

be so important, is treated here primarily through partial charge sites. The sensitivity of these long-range interactions to this kind of model, and its accuracy in the vapour phase, should be investigated. Moreover, the effect of using an Ewald summation scheme, or similar method, to model long-range electrostatic interactions, rather than the cutoff at 1.4nm used here, should be examined.

- As long-range interactions are seen to be important, the effect of finite-size effects should be investigated. This would involve much larger simulations. Different deposition heights could also be examined. These issues are discussed in more detail next.

6.3.2 Long length Scales

This study has focused on ASW PVD simulations on a small scale 30 by 30 Angstrom substrates. Future work should grow ASW structures using broadly the same methods as outlined in chapter 3 but for much larger substrates, perhaps approximately 300 by 300 angstroms in area. These large scale simulations would consist of 500,000 depositing water molecules at a range of temperatures. This would allow investigation of ASW morphology and growth kinetics at near-ISM dust grain scales, and would provide a more detailed analysis of icy mantle morphology in the ISM. However, such simulations would require large memory and disk space; approximately 120 Gigabytes of RAM and Terabytes of disk space respectively. These simulations should be performed on the same node to benefit from shared memory parallelisation such as OpenMP (Open Manual Parallelisation). The alternative route would be to use parallel computing through the use of a MPI (message passing interface) which is not as computationally efficient as shared memory computing due to communication overheads.

DL_POLY 2 has OpenMP and MPI interfaces integrated already so it is anticipated that these options could be activated without too much alteration of the existing code.

6.3.3 Long Time Scales

In addition to investigating long length scales it would be interesting to investigate long time scales. Icy mantles exist on interstellar dust grains for thousands of years prior to the onset of star formation, yet the simulations here are of the order of 10 ns. So an increase of timescale by around 18 orders of magnitude or more would be needed to properly model ASW growth and annealing mechanisms in the ISM. Understanding how ASW morphology changes over these long timescales could have important implications for both dust grain aggregation in the ISM and subsequent formation of planetesimals, and for surface promoted chemistry. If the ASW icy mantle morphology changes significantly over this extended timescale this will affect the catalytic properties of these icy mantles, potentially reducing the possibility of certain chemical reactions.

In molecular dynamics it is possible to increase the time scale by using Hyperdynamics or TAD (Temperature Accelerated Dynamics). Of the two, hyperdynamics is easier to implement, in terms of coding, than TAD. Indeed, DL_POLY 3 already has Hyperdynamics integrated functionality. Both of these methods are described in detail below.

Temperature Accelerated Dynamics (TAD)

TAD is based on a harmonic approximation to transition state theory[89], and attempts to accelerate molecular dynamic time scales by increasing the system temperature. This is usually referred to as T_{high}[89,90,91], in order to speed up transitions that would naturally occur in a metastable structure given sufficient time scales. Therefore, increasing T_{high} so that it is sufficiently large that the desired system temperature T_{low} will produce greater TAD speed ups. However, if a value of T_{high} is too large molecules will possess unrealistic kinetic energies resulting in high energy phase transitions which would not happen naturally at T_{low}; conversely if a T_{high} value is too low the system will not posses sufficient kinetic energy required for transitions. Thus there is a optimum value for T_{high} for a MD system which is dependent on the system molecular configuration.

This method is consistent with Arrhenius' Law which states that the rate which a

transition will occur, k_i, is proportional to the activation energy barrier E_i and temperature T as shown below in equation (6.1) below.

$$k_i = A_i \exp\left[E_i / k_b T \right] \tag{6.1}$$

A_i and k_b are the constant of proportionality and Boltzmann's constant respectively. TAD simulations are performed using a basin constrained MD simulation at T_{high} until a transition has been detected, where a transition is defined as a particle leaving its potential basin and overcoming a potential energy barrier (E_i). The time taken for this transition to occur at high temperature is known as $t_{i,high}$. This high temperature transition time can then be translated back to the desired system temperature time ($t_{i,low}$) using Arrhenius' law as shown below.

$$t_{i,low} = t_{i,high} \exp\left(E_i / (\beta_{low} - \beta_{high}) \right) \tag{6.2}$$

where

$$\beta = 1 / k_b T \tag{6.3}$$

In order for the simulation to proceed to the new basin state, all possible realistic transitions must be considered. In practice this is achieved by performing multiple high temperature runs and recording which transitions have occurred before returning the system back to its initial configuration and iterating. The number of iterations is chosen arbitrarily in line with how confident one is that no other realistic transitions can occur. At some stage the high temperature MD simulation is stopped and the lowest waiting transition time ($t_{low,short}$) is accepted[90] and another basin constrained MD simulation is performed with this new basin state. Initially high temperature basin constrained MD simulations are run for as long is needed for a transition to occur, but progressively there is no point running these high temperature simulation beyond $t_{low,short}$ of a previously recorded transition, so the stop time for these simulation, $t_{high,stop}$ is determined by the expression below,

$$t_{high,stop} = \left(\frac{1}{v_{min}}\right)\left(v_{min} t_{low,short}\right)^{T_{low}/T_{high}} \tag{6.4}$$

where

$$v_{min} = A_{min} / \ln\left(1/\delta\right) \tag{6.5}$$

where δ is the confidence factor which lies between 0 and 1, with 0 being most confident[90,91]. In each case the TAD simulation is accelerated by $t_{low,short}$ for each iteration.

Hyperdynamics

Hyperdynamics is also based on transition state theory (TST). The difference with this approach is that potential energy wells are filled with a non negative bias potential ($\Delta V_b(r)$) to effectively lower activation energy barriers[92]. This increases the frequency of state transitions whilst maintaining relative state transition probabilities. This is shown graphically in Figure 48 below

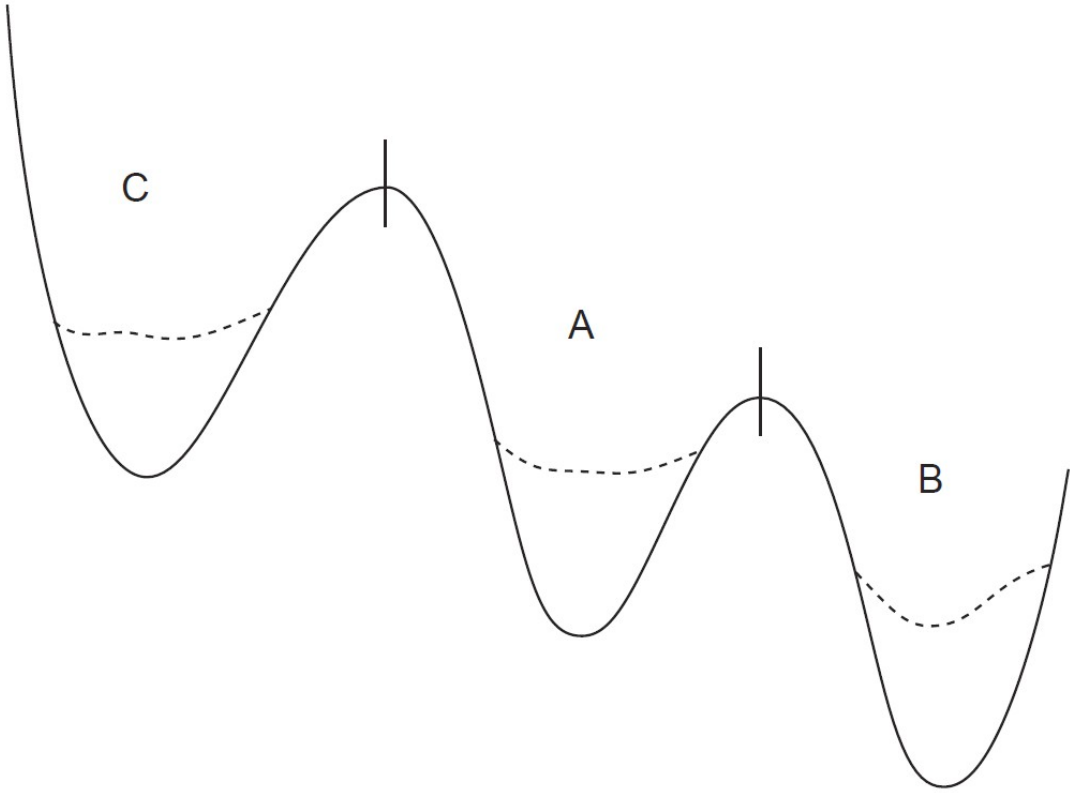

Figure 48: Schematic illustration of the hyperdynamics method. A bias potential ΔVb(r) is added to the original potential (V(r), solid line). Provided that V(r) meets certain conditions, primarily that it be zero at the dividing surfaces between states, a trajectory on the biased potential surface (ΔVb(r)+V(r); dashed line) escapes more rapidly from each state without corrupting the relative escape probabilities. The accelerated time is estimated as the simulation proceeds[hyper4].

Therefore, the MD simulation which has a biased potential will evolve quicker than the unbiased potential simulation, and the relationship between these two simulations is measured using TST. The escape rate from transition A to B is given by the following expression

$$k_A = \left\langle |v_A| \delta_A(r) \right\rangle_A \tag{6.6}$$

where δ_A is the Dirac delta function positioned at the boundary of state A and v_A is the velocity normal at the state A boundary, the angle brackets denotes the canonical ensemble average. There are three conditions which are imposed on any bias potential

- The gradient of the bias potential must be > 0 whilst in state A

- The gradient of the bias potential must be = 0 whilst on the state A boundary
- The gradient of the bias potential must be < 0 outside state A

This is shown graphically in Figure 49 below

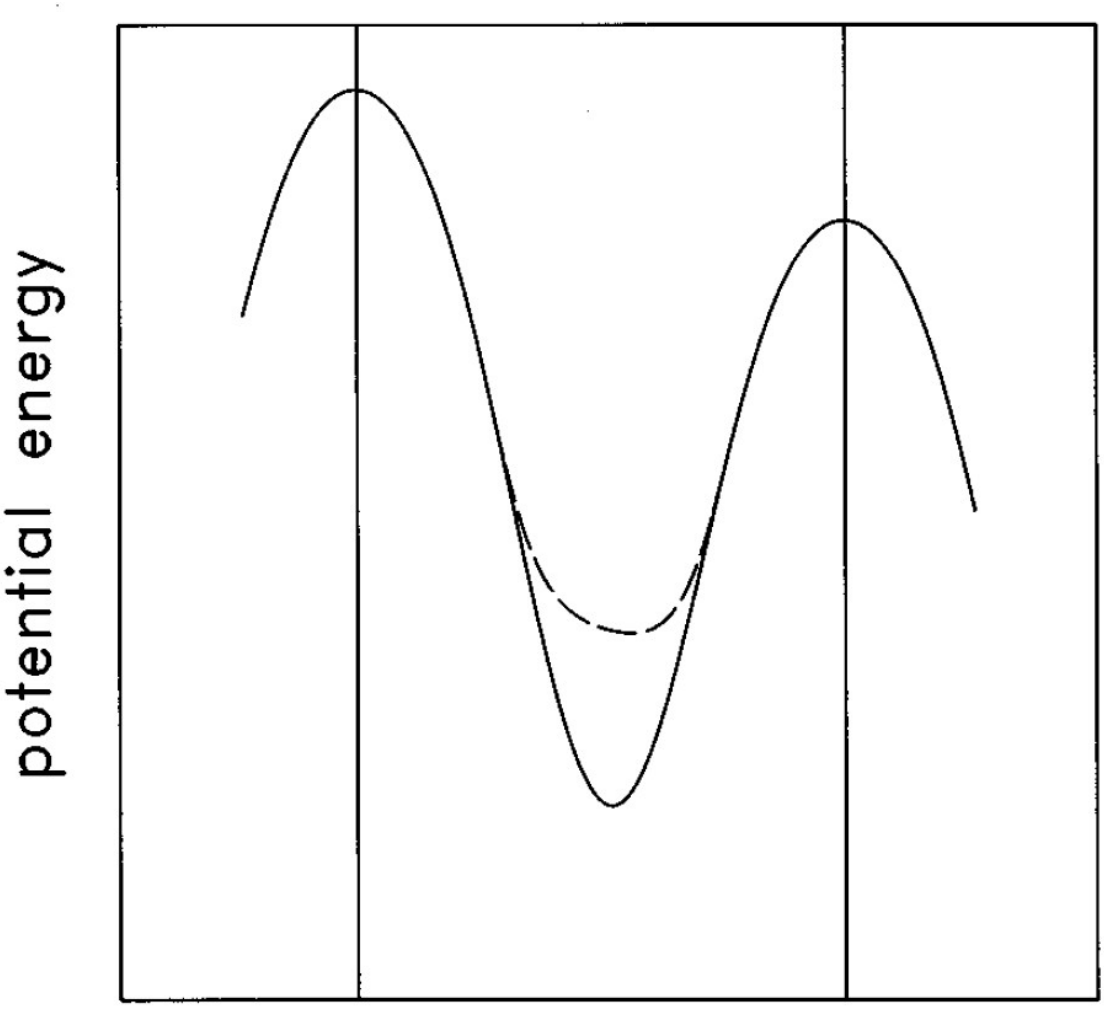

Figure 49: Schematic illustration of a one-dimensional potential V(r) (solid line) defining state A, and the biased potential $\Delta V_b(r)$ (dashed line), which defines state A_b . The potentials are equivalent at the TST boundaries (indicated by vertical lines), so the relative probability of escape to the left vs right is the same for both states, although the escape rates are enhanced for state A_b [93].

Re-factoring equation (6.6) above for the bias potential and taking importance sampling into consideration we get the following expression

$$k_A = \frac{\left\langle |v_A| \delta_A(r) e^{\beta \Delta V_b(r)} \right\rangle_{A_b}}{\left\langle e^{\beta \Delta V_b(r)} \right\rangle_{A_b}} \tag{6.7}$$

where β is defined in equation (6.3) above. The bias potential should vanish at state boundaries so the above equation can be written as

$$k_A = \frac{\left\langle |v_A| \delta_A(r) \right\rangle_{A_b}}{\left\langle e^{\beta \Delta V_b(r)} \right\rangle_{A_b}} \tag{6.8}$$

As shown in Figure 49 the escape rates are the same for both the biased and unbiased potentials and in order to equate the two systems the biased potential simulation is advanced by a larger time step as outlined below.

$$t_{hyper} = \sum_{i}^{n} \Delta T_{MD} \exp^{\beta \Delta V(r(t_i))} \tag{6.9}$$

where t_{hyper}, i, ΔT_{MD} and n are the accelerated time step, number of time steps, simulation time step and the total number of time steps respectively. The degree of time acceleration is given by the boost factor as shown below

$$boost\ factor = \frac{t_{hyper}}{t_{MD}} \tag{6.10}$$

Hyperdynamics is easier to implement than TAD as it only requires a bias and un-biased potential for atomic pairs in order to compute the boost factor and hence time acceleration. However, there is a computational cost as a hyperdynamics simulation calculates two potential energies and forces for each atomic pair in the system which significantly increases the computation workload for an MD simulation. Another disadvantage of hyperdynamic simulations is that it is difficult to 'engineer' bias potentials that offer substantial boost factors[94,95]. Conversely, TAD simulations require significant MD code changes and are notoriously difficult to implement[92].

6.3.4 ASW – gas interactions

One of the key areas of interest for the astrochemical community is how ASW interacts

with space borne ISM gas species. Many types of interactions could be investigated, from 'physical' interactions with a range of depositing atom and molecule species, to 'chemical' interactions, i.e. as a catalytic surface.

The former could be investigated by adopting essentially the same kind of PVD simulations as developed in this thesis, albeit with different gas phase species such as atomic and molecular hydrogen, carbon monoxide, carbon dioxide and methanol (as shown in Table 3). It would be interesting to investigate how gas phase species effect ASW morphology as they penetrate deep into ASW pores. In particular, what impact do gas phase species have on the number of dangling hydrogen bonds, which is important for ASW catalysis.

The latter kind of chemical interactions will allow for a more detailed analysis of how ASW acts as a catalyst. This is important from an astronomical point of view as dust grain icy mantles are thought to be the main driver for molecular hydrogen generation in the ISM. This is important for two reasons

- Molecular hydrogen and carbon monoxide 'cool' dense molecular clouds in the ISM by absorbing cosmic and high energy photons and dissipating that excess energy through exciting density of states (rotational and vibration modes of motion). This maintains the low gas and dust grain temperature required for surface chemistry to occur, which further exacerbates the cooling process eventually leading to gravitation collapse and protostellar cores as outlined in sections 1.2.6 and 1.2.7.
- Molecular hydrogen may act as a 'foundation' for more complex surface chemistry leading to more complex compounds such as methanol and others as outlined in Table 3.

Although the ASW structures which have been grown in this study could be used for this analysis, it is difficult to model chemical reactions using molecular dynamics simulations[96,97,98]. Previous studies[96] have used ab-initio (quantum) simulations combined with MD to model chemical reactions. The main difficulty here would be accurately representing reaction rates for various molecular configurations at such low

temperatures. In addition to this, atomic hydrogen at such low temperature will also be subject to quantum effects which would also have to be accurately modelled.

6.3.5 Dust Grain Aggregation

The other issue relating to ASW properties is its interaction with dust grains in the ISM. Previous experimental studies have tied to simulate icy dust grain collision kinetics using a range of different of microgravity methods from drop tower experiments[99,100], parabolic flight experiments[9,101], space shuttle missions[102,103], and space-borne experiments on the international space station[104]. However, all of these experiments have tried to simulate dust grain aggregation using either bare dust grain surfaces or non-porous crystalline icy mantles. It would also be interesting to study icy dust grain aggregation using the ASW structures produced by this study, as these icy mantles are more porous with more dangling hydrogen bonds and therefore should be more capable of dissipating collision energies (as outlined in section 6.1.2) which is crucial for planet, comet and asteroid formation. In particular, investigating how the ASW icy mantle deforms during collisions between dust grains, and what impact that has on dangling hydrogen bonds and the wider ASW tetrahedral hydrogen bonding network and the overall sticking probability will greatly improve our understanding of icy dust grain aggregation kinetics in the ISM and subsequently the origins of planet, asteroid and comet formation in the universe.

7. Bibliography

[1] Eric Herbst, "Chemistry of Star-Forming Regions," J. Phys. Chem. A **109** (18), 4017–4029 (2005).

[2] P. Caselli, "Chemical processes in star forming regions," Cores to Clusters: Star Formation with Next Generation Telescopes **324**, 47-65 (2005).

[3] P. Ehrenfreund, H. J. Fraser, J. Blum, J. H. E. Cartwright, J. M. Garcia-Ruiz, E. Hadamcik, A. C. Levasseur-Regourd, S. Price, F. Prodi, and A. Sarkissian, "Physics and chemistry of icy particles in the universe: answers from microgravity," Planetary and Space Science **51** (7-8), 473-494 (2003).

[4] Aigen Li, "On the Absorption and Emission Properties of Interstellar Grains," AIP Conference Proceedings **761** (1), 123-133 (2005).

[5] S. G. Coulson, "The influence of magnetic properties on the absorption of porous spheres," Monthly Notices of the Royal Astronomical Society **389** (4), 1885-1890 (2008).

[6] E. F. van Dishoeck and G. A. Blake, "Chemical evolution of star-forming regions," Annual Review of Astronomy and Astrophysics **36**, 317-368 (1998).

[7] P. Jenniskens, D. F. Blake, M. A. Wilson, and A. Pohorille, "High-Density amorphous ice, the frost on interstellar grains", Astrophysical Journal **455** (1), 389-401 (1995).

[8] Pascale Ehrenfreund and Helen Fraser, "Ice chemistry in space," NATO Science Series II: Mathematics, Physics and Chemistry **120** (1), 40 (2000).

[9] D. M. Salter, D. Heisselmann, G. Chaparro, G. van der Wolk, P. Reissaus, A. G. Borst, R. W. Dawson, E. de Kuyper, G. Drinkwater, K. Gebauer, M. Hutcheon, H. Linnartz, F. J. Molster, B. Stoll, P. C. van der Tuijn, H. J. Fraser, and J. Blum, "A zero-gravity instrument to study low velocity collisions of fragile particles at low temperatures," Review of Scientific Instruments **80** (7) (2009).

[10] U. J. Meierhenrich, G. M. M. Caro, W. A. Schutte, B. Barbier, A. A. Segovia, A. Back, H. Rosenbauer, and W. H. P. Thiemann, "Amino acids from ultraviolet

irradiation of interstellar ice analogues," Geochimica Et Cosmochimica Acta **66** (15A), A505-A505 (2002).

[11] M. P. Bernstein, J. P. Dworkin, S. A. Sandford, G. W. Cooper, and L. J. Allamandola, "Racemic amino acids from the ultraviolet photolysis of interstellar ice analogues," Nature **416** (6879), 401-403 (2002).

[12] P. Ehrenfreund, M. P. Bernstein, J. P. Dworkin, S. A. Sandford, and L. J. Allamandola, "The photostability of amino acids in space," Astrophysical Journal **550** (1), L95-L99 (2001).

[13] S. B. Charnley, P. Ehrenfreund, and Y. J. Kuan, "Spectroscopic diagnostics of organic chemistry in the protostellar environment," Spectrochimica Acta Part a-Molecular and Biomolecular Spectroscopy **57** (4), 685-704 (2001).

[14] J. C. Lee and B. Ravel, "Determining the grain composition of the interstellar medium with high-resolution X-ray spectroscopy," Astrophysical Journal **622** (2), 970-976 (2005).

[15] A. G. Li and J. M. Greenberg, "Mid-infrared spectropolarimetric constraints on the core-mantle interstellar dust model," Astrophysical Journal **577** (2), 789-794 (2002).

[16] D. C. B. Whittet, W. A. Schutte, Aggm Tielens, A. C. A. Boogert, T. deGraauw, P. Ehrenfreund, P. A. Gerakines, F. P. Helmich, T. Prusti, and E. F. vanDishoeck, "An ISO SWS view of interstellar ices: First results," Astronomy and Astrophysics **315** (2), L357-L360 (1996).

[17] Isa Oliveira, Klaus M. Pontoppidan, Bruno Merin, Ewine F. van Dishoeck, Fred Lahuis, Vincent C. Geers, Jes K. Jorgensen, Johan Olofsson, Jean-Charles Augereau, and Joanna M. Brown, "A SPITZER SURVEY OF PROTOPLANETARY DISK DUST IN THE YOUNG SERPENS CLOUD: HOW DO DUST CHARACTERISTICS EVOLVE WITH TIME?," Astrophysical Journal **714** (1), 778-798 (2010).

[18] Accolla, M., E. Congiu, F. Dulieu, G. Manico, H. Chaabouni, E. Matar, H. Mokrane, J. L. Lemaire & V. Pirronello “Changes in the morphology of interstellar ice analogues after hydrogen atom exposure,” Physical Chemistry Chemical Physics, **13,** 8037-8045 (2011).

[19] Keane, J. V., A. C. A. Boogert, A. Tielens, P. Ehrenfreund & W. A. Schutte "Bands of solid CO2 in the 2-3 mu m spectrum of S 140 : IRS1," Astronomy & Astrophysics, **375,** L43-L46 (2001).

[20] Pontoppidan, K. M., H. J. Fraser, E. Dartois, W. F. Thi, E. F. van Dishoeck, A. C. A. Boogert, L. d'Hendecourt, A. Tielens & S. E. Bisschop "A 3-5 mu m VLT spectroscopic survey of embedded young low mass stars I - Structure of the CO ice," Astronomy & Astrophysics, 408**,** 981 (2003)

[21] P. Jenniskens, S. F. Banham, D. F. Blake, and M. R. S. McCoustra, "Liquid water in the domain of cubic crystalline ice I-c," Journal of Chemical Physics **107** (4), 1232-1241 (1997).

[22] D. F. Blake, L. J. Allamandola, S. Sandford, and F. Freund, "CLATHRATE TYPE-II HYDRATE FORMATION INVACUO UNDER ASTROPHYSICAL CONDITIONS," Meteoritics **26** (4), 319-320 (1991).

[23] A. G. G. M Tielens, *The physics and chemistry of the interstellar medium*. (Cambridge Universtity Press, Kapteyn Astronomical Institute, 2005), 1 ed.

[24] J.E Dyson and D.A Williams, *The physics of the interstellar medium*. (Taylor & Francis, 1997), 2nd Edition ed.

[25] David Williams, "Gas and dust in the interstellar medium," Journal of Physics: Conference Series **6** (1), 17 (2005).

[26] http://homepages.wmich.edu/~korista/stargal-images/barnard68_vis-nir.jpg

[27] J. M. Greenberg, "The secrets of stardust," Scientific American **283** (6), 70-75 (2000).

[28] B. R. Rowe, A. Canosa, and I. R. Sims, "RATE COEFFICIENTS FOR INTERSTELLAR GAS-PHASE CHEMISTRY," Journal of the Chemical Society-Faraday Transactions **89** (13), 2193-2198 (1993).

[29] H. J. Fraser, M. P. Collings, and M. R. S. McCoustra, "Laboratory surface astrophysics experiment," Review of Scientific Instruments **73** (5), 2161-2170 (2002).

[30] M. P. Collings, M. A. Anderson, R. Chen, J. W. Dever, S. Viti, D. A. Williams,

and M. R. S. McCoustra, "A laboratory survey of the thermal desorption of astrophysically relevant molecules," Monthly Notices of the Royal Astronomical Society **354** (4), 1133-1140 (2004).

[31] E. L. Gibb, D. C. B. Whittet, A. C. A. Boogert, and Aggm Tielens, "Interstellar ice: The Infrared Space Observatory legacy," Astrophysical Journal Supplement Series **151** (1), 35-73 (2004).

[32] A. C. A. Boogert, K. M. Pontoppidan, C. Knez, F. Lahuis, J. Kessler-Silacci, E. F. van Dishoeck, G. A. Blake, J. C. Augereau, S. E. Bisschop, S. Bottinelli, T. Y. Brooke, J. Brown, A. Crapsi, N. J. Evans, II, H. J. Fraser, V. Geers, T. L. Huard, J. K. Jorgensen, K. I. Oberg, L. E. Allen, P. M. Harvey, D. W. Koerner, L. G. Mundy, D. L. Padgett, A. I. Sargent, and K. R. Stapelfeldt, "The c2d Spitzer spectroscopic survey of ices around low-mass young stellar objects. I. H(2)O and the 5-8 mu m bands," Astrophysical Journal **678** (2), 985-1004 (2008).

[33] Robin Garrod, In Hee Park, Paola Caselli, and Eric Herbst, "Are gas-phase models of interstellar chemistry tenable? The case of methanol," Faraday Discussions **133**, 51-62 (2006).

[34] F. Dulieu, L. Amiaud, E. Congiu, J. H. Fillion, E. Matar, A. Momeni, V. Pirronello, and J. L. Lemaire, "Experimental evidence for water formation on interstellar dust grains by hydrogen and oxygen atoms," Astronomy & Astrophysics **512** (2010).

[35] Shu, F. H. “SELF-SIMILAR COLLAPSE OF ISOTHERMAL SPHERES AND STAR FORMATION”. *Astrophysical Journal,* 214**,** 488-497. Astrophysical Journal **214**, 488-497 (1977).

[36] M. R. Hogerheijde, "Chemical evolution of protostars," Astrophysics and Space Science **295** (1-2), 179-187 (2005).

[37] Ewine F. van Dishoeck, presented at the Conference on Astrophysics in the Next Decade, Tucson, AZ, 2009 (unpublished).

[38] Wendy A. Brown, Serena Viti, Angela J. Wolff, and Amandeep S. Bolina, "Laboratory investigations of the role of the grain surface in astrochemical models," Faraday Discussions **133**, 113-124 (2006).

[39] O. Yamamuro, Y. Madokoro, H. Yamasaki, T. Matsuo, I. Tsukushi, and K.

Takeda, "Low-energy excitations of vapor-deposited amorphous ice and its annealing and methanol-doping effects studied by inelastic neutron scattering," Journal of Chemical Physics **115** (21), 9808-9814 (2001).

[40] J. M. K. Donev, Q. Yu, B. R. Long, R. K. Bollinger, and S. C. Fain, "Noncontact atomic force microscopy studies of ultra thin films of amorphous solid water deposited on Au (111)," J. Chem. Phys. **123** (1), 6 (2005).

[41] DT Bowron, JL Finney, A Hallbrucker, I Kohl, T Loerting, E Mayer, and AK Soper, "The local and intermediate range structures of the five amorphous ices at 80K and ambient pressure: A Faber-Ziman and Bhatia-Thornton analysis," The Journal of Chemical Physics **125** (1), 1-14 (2006).

[42] A. S. Bolina, A. J. Wolff, and W. A. Brown, "Reflection absorption infrared spectroscopy and temperature-programmed desorption studies of the adsorption and desorption of amorphous and crystalline water on a graphite surface," Journal of Physical Chemistry B **109** (35), 16836-16845 (2005).

[43] L. Hornekaer, A. Baurichter, V. V. Petrunin, A. C. Luntz, B. D. Kay, and A. Al-Halabi, "Influence of surface morphology on D-2 desorption kinetics from amorphous solid water," Journal of Chemical Physics **122** (12) (2005).

[44] Z. Dohnálek, Greg A. Kimmel, Patrick Ayotte, R. Scott Smith, and Bruce D. Kay, "The deposition angle-dependancy density of amorphous solid water films," J. Chem. Phys. **128** (1), 9 (2003).

[45] Jean-Hugues Fillion, Lionel Amiaud, François Dulieu, Anouchah Momeni, Saoud Baouche, and Jean-Louis Lemaire, "Experimental studies of H2 and D2 interaction with water ice films," Astrochemistry: Recent Successes and Current Challenges
Poster Book IAU Symposium **231** (1) (2005).

[46] H. Wang, R. C. Bell, M. J. Iedema, A. A. Tsekouras, and J. P. Cowin, "Sticky ice grains aid planet formation: Unusual properties of cryogenic water ice," Astrophysical Journal **620** (2), 1027-1032 (2005).

[47] H. M. Cuppen and Eric Herbst, "Simulation of the formation and morphology of ice mantles on interstellar grains," Astrophysical Journal **668** (1), 294-309 (2007).

[48] Frenkel Daan and Smit Berend. “Understanding Molecular Simulation from Algorithms to applications,” vol. 1. Academic Press Inc. (2001)

[49] Peter A. “Atkin's Physical Chemistry.” Oxford University Press, Oxford. (2009).

[50] Wang L & Sadus RJ. “Effect of three-body interactions on the vapor-liquid phase equilibria of binary fluid mixtures,” Journal of Chemical Physics **125**. (2006a).

[51] Wang L & Sadus RJ. “Three-body interactions and solid-liquid phase equilibria: Application of a molecular dynamics algorithm,” Physical Review E **74**. (2006b).

[52] Li JH, Zhou ZW & Sadus RJ. “Role of nonadditive forces on the structure and properties of liquid water,” Journal of Chemical Physics **127,** 7. (2007).

[53] Marcelli G & Sadus RJ. “Molecular simulation of the phase behavior of noble gases using accurate two-body and three-body intermolecular potentials,” Journal of Chemical Physics **111,** 1533-1540. (1999).

[54] Nasrabad AE & Deiters UK. “Prediction of thermodynamic properties of krypton by Monte Carlo simulation using ab initio interaction potentials,” Journal of Chemical Physics **119,** 947-952. (2003).

[55] Bukowski R & Szalewicz K. “Complete ab initio three-body nonadditive potential in Monte Carlo simulations of vapor-liquid equilibria and pure phases of argon,” Journal of Chemical Physics **114,** 9518-9531. (2001).

[56] Rapaport D.C. “The Art of Molecular Dynamics Simulation,” Cambridge University Press, Cambridge. (2004).

[57] Allen M.P and Tildesley D.J. “Computer Simulation of Liquids,” Clarendon Press, New York. (1989).

[58] W Chester. (1980). *Mechanics*. HarperCollins Publishers Ltd, London. ISBN 0-04-510058-6

[59] Evans DJ & Murad S. “SINGULARITY FREE ALGORITHM FOR MOLECULAR-DYNAMICS SIMULATION OF RIGID POLYATOMICS,” Molecular Physics **34,** 327-331. (1977).

[60] Ewald P.P. “Die Berechnung optischer und elektrostatischer Gitterpotentiale,”

Annalen der Physik **369,** 253-287. (1921)

[61] Jorge M & Seaton NA. (2002). Long-range interactions in Monte Carlo simulation of confined water. *Molecular Physics* **100,** 2017-2023.

[62] Giovambattista N, Angell CA, Sciortino F & Stanley HE. "Glass-transition temperature of water: A simulation study," Physical Review Letters **93**. (2004).

[63] Guillot B & Guissani Y. "Polyamorphism in low temperature water: A simulation study," Journal of Chemical Physics **119,** 11740-11752. (2003).

[64] Giovambattista N, Loerting T, Lukanov BR & Starr FW. "Interplay of the Glass Transition and the Liquid-Liquid Phase Transition in Water," Scientific Reports **2**. (2012).

[65] English NJ, Tse JS & Gallagher R. "Thermal conductivity in amorphous ices from molecular dynamics," Physical Review *B* **82,** 4. (2010).

[66] Hoshino K, Yoshikawa T & Munejiri S. "Pressure-induced structural change from low-density to high-density amorphous ice by molecular-dynamics simulations," Computer Physics Communications **182,** 49-51. (2011).

[67] Buch V & Zhang Q. "STICKING PROBABILITY OF H AND D ATOMS ON AMORPHOUS ICE - A COMPUTATIONAL STUDY," Astrophysical Journal **379,** 647-652. (1991).

[68] Wilson MA, Pohorille A, Jenniskens P & Blake DF. "PROBING THE STRUCTURE OF COMETARY ICE," Origins of Life and Evolution of the Biosphere **25,** 3-19. (1995).

[69] Essmann U & Geiger A. "MOLECULAR-DYNAMICS SIMULATION OF VAPOR-DEPOSITED AMORPHOUS ICE," Journal of Chemical Physics **103,** 4678-4692. (1995).

[70] Kimmel GA, Dohnalek Z, Stevenson KP, Smith RS & Kay BD. "Control of amorphous solid water morphology using molecular beams. II. Ballistic deposition simulations," Journal of Chemical Physics **114,** 5295-5303. (2001).

[71] Guillot B & Guissani Y. "Polyamorphism in low temperature water: A simulation study," Journal of Chemical Physics **119,** 11740-11752. (2003).

[72] Guillot B & Guissani Y. "Investigation of vapor-deposited amorphous ice and

irradiated ice by molecular dynamics simulation," Journal of Chemical Physics **120,** 4366-4382. (2004).

[73] http://www.csar.cfs.ac.uk/user_information/software/chemistry/dl_poly.shtml

[74] http://www.epsrc.ac.uk/Pages/default.aspx

[75] http://www.ccp5.ac.uk/

[76] http://www.icmab.es/molsim/

[77] Gonzalez MA & Abascal JLF. "A flexible model for water based on TIP4P/2005," Journal of Chemical Physics **135**. (2011).

[78] Mahoney MW & Jorgensen WL. "A five-site model for liquid water and the reproduction of the density anomaly by rigid, nonpolarizable potential functions. Journal of Chemical Physics **112,** 8910-8922. (2000).

[79] Cho CH, Singh S & Robinson GW. "Understanding all of water's anomalies with a nonlocal potential," Journal of Chemical Physics **107,** 7979-7988. (1997).

[80] Roy R, Tiller WA, Bell I & Hoover MR. "The structure of liquid water; Novel insights from materials research; Potential relevance to homeopathy," Materials Research Innovations **9,** 98-103. (2005).

[81] Rick SW. "Simulations of ice and liquid water over a range of temperatures using the fluctuating charge model," Journal of Chemical Physics **114,** 2276-2283. (2001).

[82] Paricaud P, Predota M, Chialvo AA & Cummings PT. "From dimer to condensed phases at extreme conditions: Accurate predictions of the properties of water by a Gaussian charge polarizable model," Journal of Chemical Physics **122**. (2005).

[83] Horn HW, Swope WC, Pitera JW, Madura JD, Dick TJ, Hura GL & Head-Gordon T. "Development of an improved four-site water model for biomolecular simulations: TIP4P-Ew," Journal of Chemical Physics **120,** 9665-9678. (2004).

[84] Swiatla-Wojcik D. "Evaluation of the criteria of hydrogen bonding in highly associated liquids," Chemical Physics **342,** 260-266. (2007).

[85] Liu JF, Liu C, Li Q & Asme. "DYNAMICAL BEHAVIOR AND FLOW MECHANISM OF FLUID IN NANOCHANEL BY MOLECULAR

DYNAMICS SIMULATION," Icnmm 2009, Pts a-B**,** 863-866. (2009).

[86] G. A. Kimmel, K. P. Stevenson, Z. Dohnalek "Control of amorphous solid water morphology using molecular beams. I. Experimental results" Chemical Physics **114,** 5284-5294. (2001).

[87] P. Ayotte R. S. Smith, K. P. Stevenson, Z. Dohnalek, G. A. Kimmel "" J. Geophys. Res. **106** 33387 2001

[88 N. Horimoto, H. S. Kato, M. Kawai "" Journal of Chemical Physics **116** 4375 (2002)

[89] Y. Shim, J. G. Amar "Adaptive temperature-accelerated dynamics" Journal of Chemical Physics **134** 054127 (2011)

[90] M. R. Sorensen, V. F. Voter "Temperature-accelerated dynamics for simulation of infrequent events" Journal of Chemical Physics **112** 9599 (2000)

[91] F. Montalenti A. F. Voter "Exploiting past visits or minimum-barrier knowledge to gain further boost in the tempature-accelerated dynamics method" Journal of Chemical Physics **116** 4819 (2002)

[92] P. Danny, B. P. Uberuaga, Y. Shim, J. G. Amar, A. F. Voter "Accelerated Molecular Dynamics Methods: Introduction and Recent Developments" Annual Reports in Computational Chemistry 5 79 (2009)

[93] A. F. Voter "A method for accelerating the molecular dynamics simulation of infrequent events" Journal of Chemical Physics 106 4665 (1997)

[94] L. Y. Chen, N. J. M. Horing "An exact formulation of hyperdynamics simulations" 126 224103 (2007)

[95] M. M. Steiner, P. A. Genilloud, J. W. Wilkins "Simple bias potential for boosting molecular dynamics with the hyperdynamics scheme" Physical Review B 57 10236 (1997)

[96] M. R. Weismiller, M. F. Russo, A. C. T. van Duin, R. A. Yetter "Using molecular dynamics simulations with a ReaxFF reactive force field to develope a kinetic mechanism for ammonia borane oxidation" Proceedings from the Combustion Institute 34 3489-3497 (2013)

[97] S. Tolosa, A. Hidalgo, J. A Sanson, "Thermodynamic Study of Hydrolysis Reactions in Aqueous Solution from Ab Initio Potential and Molecular

Dynamics Simulations" Journal of Chemistry 265958 DOI: 10.1155/2013/265958 (2013)

[98] X. J. Wang, Zhi-Yi Li, Z. Liu "Molecular Dynamics Simulations on Hydrolysis of Zinc Acetate in Supercritical Water" ACTA PHYSICO-CHIMICA SINICA **29** 23-29

[99] J. Blum, G. Wurm, T. Poppe, S. Kempf, and T. Kozasa, Adv. Space Res. **29**, 497 (2002).

[100] D. Langkowski, J. Teiser, and J. Blum, Astrophys. J. 675, 764 (2008).

[101] J. E. Colwell, S. Sture, M. Cintala, D. Durda, A. Hendrix, T. Goudie, D. Curtis, D. J. Ashcom, M. Kanter, T. Keohane, A. Lemos, M. Lupton, and M. Route, Icarus 195, 908 (2008).

[102] J. Colwell and M. Taylor, Icarus 138, 241 (1999).

[103] J. E. Colwell, Icarus 164, 188 (2003).

[104] S. G. Love and D. R. Pettit, in Lunar and Planetary Institute Conference Abstracts, edited by S.